Thermoelectric Properties of Few-Electron Quantum Dots

Dissertation zur Erlangung des
naturwissenschaftlichen Doktorgrades
der Bayerischen Julius-Maximilians-Universität
Würzburg

vorgelegt von

Ralf Scheibner

geboren in Ebern

Würzburg 2007

Eingereicht am: 30.08.2007
bei der Fakultät für Physik und Astronomie
der Julius-Maximillians-Universität Würzburg

1. Gutachter: Prof. Dr. Hartmut Buhmann

2. Gutachter: Prof. Dr. Vladimir Dyakonov

3. Gutachter: Prof. Dr. Kornelius Nielsch

Tag des Promotionskolloquiums: 16.01.2008

1. Prüfer: Prof. Dr. Hartmut Buhmann

2. Prüfer: Prof. Dr. Vladimir Dyakonov

3. Prüfer: Prof. Dr. Kornelius Nielsch

4. Prüfer: Prof. Dr. Björn Trauzettel

Meiner Familie

Parts of this thesis have been published in:

- R. Scheibner, H. Buhmann, D. Reuter, M.N. Kiselev, and L.W. Molenkamp
  'Thermopower of a Kondo spin-correlated quantum dot',
  Phys. Rev. Lett. **95**, 176602 (2005)
  recited in 'Virtual Journal of Nanoscale Science & Technology', 31. Oct. 2005.

- R. Scheibner, E.G. Novik, T. Borzenko, M. König, D. Reuter, A.D. Wieck, H. Buhmann, and L.W. Molenkamp
  'Sequential and cotunneling behavior in the temperature-dependent thermopower of few-electron quantum dots',
  Phys. Rev. B **75**, 041301 (2007).

Submitted for publication:

- R. Scheibner, M. König, D. Reuter, A.D. Wieck, H. Buhmann, and L.W. Molenkamp, *'Quantum dot as a thermal rectifier'*,
  arXiv:cond-mat/0703514v1 (2007); submitted to Phys. Rev. Lett.

  Further Chapters of this thesis are considered for publication.

Contents

Introduction

The information technology based society has an increasing demand for efficient computing power. A gain in efficiency can be achieved by reduced production costs for single logic devices, by an increased number of computational operations per given time interval, or by reduced energy consumption in relation to the number of logic operations. These goals are achievable by means of size reduction of conventional logic components, which are based on the laws of classical information theory, and by the application of quantum information theory. The latter allows a high degree of parallel information processing to be attained. The fundamental limit of the size of new information processing and storing devices is given by the properties of single particles, or to be more precise, the spacial extension of single quantum states. The particle states are characterized by a given set of quantum numbers and these states yield the information that has to be stored or processed. Modern semiconductor fabrication technologies make it possible for these geometric limits to be approached, and consequently offer the prospect of scalable semiconductor quantum processing devices; hence, the intense interest in the study of quantum dot (QD) structures that contain only a few electrons [LD98]. For the development of these devices, a detailed knowledge of the underlying electron transport processes is of crucial importance. So far, most of the transport experiments have focused on the electrical conductance [KMM⁺97]. Besides the proofs that semiconductor QD structures can be used for (coherent) single particle and quantum state manipulation [EHWvB⁺04, KBT⁺06], measurements have shown that the dynamic and magnetic quantum mechanical properties of the QD electrons govern the electrical transport at low temperatures [GGSAM⁺98, COK98, vdWDFF⁺00], and that (QD) systems containing confined electrons are a useful tool for studying fundamental transport phenomena, e.g. the quantum Hall effect [KDP80, vKGW05]. These, as well as many other experiments on the electrical conductance, have made few electron QDs a magnificent model system for testing the charge transport properties on the scale of a single lattice site, or single impurity, respectively.

Although thermoelectrical transport measurements are known to be more sensitive to the details of the electronic structure than conventional transport measurements [Zim63], little experimental attention has so far been paid to this kind of measurements on QDs. Thus it is desirable that such measurements be done, since the measurement of the thermoelectric power (thermopower) allows a direct analysis of the charge transport dynamics

to be carried out. Moreover, it is an important measurement due to the close connection between the thermopower and the heat transport, i.e. entropy transport. Experiments show that diverse behaviors are found for the thermopower of simple metals, where even the sign of this quantity shows no regularity. Although there has been extensive work on this topic, the low temperature theory even in metals has still not been well understood [Mah81]. Thus, it is highly desirable to establish a complete microscopic picture of thermoelectric transport in mesoscopic and quantum systems.

Recently, the field of thermoelectricity has gained large renewed attention. Much interest has been focused on understanding thermoelectric transport in nano-scale devices due to the possible applications of QDs for efficient thermoelectric power generation or cooling [SNB07b, GGB$^+$06, DiS99, KNY$^+$98]. In this connection, thermoelectric devices have the advantages of being reliable, cheap and scalable down to mesoscopic sizes, which makes them interesting for on-chip cooling applications. The advances in growth and fabrication of complex compounds, mesoscopic devices and nanostructures open up various opportunities for studying new materials and device designs. Generally speaking, the concepts are based on improving the macroscopic material properties by controlling the energy transport on a (very) small scale. The ideas to enhance the efficiency of thermoelectric devices range from modifications of the crystal lattice (phonon system), such as in super-lattice structures, over changes in the energy spectrum of the charge carriers by quantum mechanical confinement in low dimensional systems, to the use of magnetic (spin) properties in spin entropy transport. The modification of the electronic energy spectrum in low dimensional systems has a significant impact on the performance of thermoelectric and solid-state thermionic devices. It has been shown that devices with a sharply rising transmission probability significantly outperform those that do not show this behavior [OLZH05].

Within this context, single electron QDs represent the smallest thermoelectric devices besides molecular junctions [RJSM07]. They naturally have sharply rising transmission properties and provide a high degree of variability. Additionally, they allow a fundamental control of the energy and entropy flow, which makes them interesting for heat information processing [TPC02, Pey06], complementary to the well known charge based information processing. Thus, the investigation of the thermoelectric properties of few-electron QDs can contribute to the understanding of the fundamental questions of information, charge and heat transport processes in quantum systems, which represent an important basis of the future information technology based society.

The used QD design is based on lithographically patterned high electron mobility transistor nanostructures. The QDs are defined electrostatically in a 2-dimensional electron gas (2DEG). Their nominal lateral diameter is 250 nm, and the QDs contain up to a few tens of electrons. In order to observe charge quantization (Coulomb blockade) and size quantization effects (discrete energy spectrum of the QD) in the electrical and thermoelectrical transport, electromagnetic interferences and thermal noise have to be minimized. This is achieved by cooling the samples to temperatures below 1 K in an

electromagnetically shielded environment. The size and the energy spectrum of the QDs can be controlled by means of voltages applied to nearby metallic surface electrodes, and by the application of magnetic fields up to 16 T. The ambient temperature of the QD serves as an additional parameter for modifying the contributions of the various charge transport mechanisms to the overall electrical and thermoelectrical transport.

The aim of this thesis is to clarify the role of the QD energy spectrum and the QD spin properties on the thermoelectric response. This would contribute to the understanding of charge and entropy transport processes in future solid state quantum information processing and in highly efficient nano-scale thermoelectric devices. In this regard, the thesis investigates the electronic orbital and spin transport dynamics through few-electron QDs by means of electrical and thermoelectrical measurements. It should be pointed out that there are contributions to the thermoelectric transport which result from the interaction of the crystal lattice and the electrons. This so called phonon drag contribution to the thermoelectric transport is not investigated here. The experimental work has produced experimental results and confirms theoretical calculations, which were obtained earlier for the diffusion thermopower of larger QDs [SMA+93, MBGM98, DSB+97, TM02]. The new experimental findings for the thermoelectric response of few-electron QDs have been compared with theoretical model calculations. This enables a direct analysis of the composition of first and second order transport processes to be done. Deviations between measurements and simulations are discussed with respect to their various possible origins. The detailed direct comparison of nonlinear differential conduction measurements and thermopower measurements on the same sample are used to identify the thermoelectric signatures due to single QD states, and asymmetries as well as imperfections in the sample design. It is shown that under certain circumstances the QD configuration can even lead to rectifying effects in the thermal transport. The influence of the spin properties of the QD on the thermopower is studied in the spin-correlated transport regime. Here, the magnetic interaction between localized QD electrons and the free electrons in the leads creates correlated many-particle states which are known from bulk materials to exhibit a very irregular thermoelectric behavior. Having investigated extensively the QD as a tunable model system, this work can serve as a starting point for future investigations in the field of many-particle thermoelectric effects and spin entropy transport.

The details of this thesis are organized in the following chapters:

The first chapter reviews the basic concepts of electric transport through lateral few-electron QDs. A brief introduction is given on the theoretical description of QDs, and on the first and second order transport in the Coulomb blockade regime. The nonlinear electric transport is discussed with respect to the charge transfer via the discrete energy states of the QD. The chapter gives an introduction to the interpretation of Coulomb blockade diamonds which are obtained by nonlinear differential conductance measurements. The commonly known signatures of charge transport via the ground states and the excited states are summarized with respect to first and second order charge transport.

The second chapter starts by introducing the basic concepts of thermoelectricity. The thermodynamics of irreversible processes is reviewed with respect to the charge transfer and its accompanying heat flow. The macroscopic transport equations are introduced for the thermoelectric transport in microstructures and a short remark is given on the applicability of the semiclassical Mott's relation between the conductance and thermopower in the thermoelectrical transport. The chapter ends with an introductory review of the known results for thermopower oscillations in the Coulomb blockade regime.

The third chapter addresses the design of the few-electron QDs, the material system, as well as the split gate sample layout. Furthermore, the experimental techniques for the electrical and thermoelectrical characterization are explained. The chapter also discusses in detail the used current-heating technique, especially due to its importance for the quantitative analysis of the experimental data. In this regard, various electron gas temperature calibration techniques are compared.

The fourth chapter deals with measurements of the thermopower of few-electron QDs in the temperature range between 1.5 K and 40 mK. Comparison is made with results of past measurements of the thermopower of QDs in the Coulomb blockade transport regime which yielded qualitatively different results for many electron QDs. It is verified that these differences result from the different strengths of the transport processes. The temperature-dependent line shape of the thermopower oscillations in the Coulomb blockade regime is analyzed and explained with respect to the thermoelectric contributions of sequential and cotunneling transport. The observed deviations from model calculations, which account for sequential and inelastic cotunneling, are discussed with respect to the finite level spacing in the QD, the low temperature electron distribution in the heated reservoir, and the temperature stability during the measurement.

The high sensitivity of thermopower measurements very often reveals deviations from an expected ideal model system. In order to clarify the origin of these differences between theoretical model calculations and experimentally obtained data, the fifth chapter focuses on the contributions to the thermoelectric response which arise from asymmetries in the QD-lead system. Effects caused by the finite height of the connecting tunneling barriers are discussed as well as the signature of the intrinsic symmetry properties of given QD states. The thermoelectric signal is directly compared with the excitation spectrum of

the QD which is obtained independently from nonlinear differential conductance measurements. In order to show that part of the line shape of the thermoelectric signal reflects the symmetry of the coupling of given QD states to the leads, numerical model calculations are presented which are based on a resonant tunneling model. The possibility of using the internal properties of a QD for thermal rectification is discussed. The chapter ends with a section on the influence of the symmetry properties of given QD states on the thermoelectric transport via excited states in first order and second order transport.

Finally, the sixth chapter deals with the influence of the magnetic properties of the QDs and their interactions with the surrounding lead system. In the limiting case of a strong coupling of the QD to the leads, these interactions result in so called spin- or Kondo-correlations under certain circumstances. Thus, a complete picture of the electronic contributions to the thermoelectric transport requires the spin-correlation contribution to the thermopower of a few-electron QD to be studied. A clear deviation from the semiclassical Mott relation between thermopower and conductivity indicates a significant asymmetry in the spectral density of states of the spin-correlated state with respect to the Fermi energies of the reservoirs. The observed behavior is explained within the framework of an Anderson-impurity model and possible contributions to the thermoelectric transport due to spin entropy transport.

Chapter 1

Fundamentals of Coulomb-blockade in quantum dots

In this chapter, basic concepts are presented for the theoretical description of a quantum dot (QD) and for the electric transport through QDs at low temperatures. In the first section, the Hamilton operator is introduced and approximations are discussed, which are in the framework of the so called *constant interaction model* (CI-model). The second part summarizes the theoretical description of the transport through single QDs in the Coulomb blockade (CB) regime. The third section reviews the interpretation of Coulomb blockade diamonds obtained by nonlinear conductance measurements.

1.1   Theoretical description of a quantum dot

1.1.1   Hamiltonian for transport through a quantum dot

Starting with an electrostatic description of a QD, a general expression for the Hamilton operator $\hat{H}$ can be given by [HWM96, KWS$^+$01, Kel01]

$$
\begin{aligned}
\hat{H}(N) \;=\; & \frac{1}{2m^*} \sum_{n=1}^{N} [\hat{\boldsymbol{p}}_n + e\boldsymbol{A}(\hat{r}_n)] \\
& + \sum_{n=1}^{N} \Phi_{ext}(\hat{r}_n) \\
& + \frac{e^2}{2} \sum_{n=1}^{N} \sum_{n'=1, n' \neq n}^{N} G(\hat{r}_n, \hat{r}_{n'}) \\
& + g\mu_B \boldsymbol{B}\hat{\boldsymbol{S}}.
\end{aligned}
\tag{1.1}
$$

The first term of the Hamilton operator reflects the kinetic energy of N (independent) electrons in a magnetic field $\boldsymbol{B} = \nabla \times \boldsymbol{A}$, where $\boldsymbol{A}$ is the vector potential, $\hat{p}_n$ is the canonical momentum operator for the n-th electron, $\hat{r}_n$ is the corresponding position operator and e the elementary charge.

The second term describes the additional electrostatic energy due to the confining potential $\Phi_{ext}(\hat{r}_n)$. In general, $\Phi_{ext}(\hat{r}_n)$ depends on the shape and position of metallic gate electrodes, the average charge density of ionized donors or impurities and the potentials applied to the individual gate electrodes. Furthermore, a local variation of the material composition can be included, as well as the interaction of the QD electrons with its mirror charges on the gate electrodes.

In the third term, the Green-function $G(\hat{r}_n, \hat{r}_{n'})$ reflects the interaction between the QD electrons.

The last term represents the Zeeman energy of the QD in a magnetic field, where g is the Landé-factor, μ_B the Bohr magneton and $\hat{\boldsymbol{S}}$ the total spin operator.

In order to calculate the N-electron states $|N, k\rangle$ and the corresponding eigen-energies, the N-particle Schrödinger equation has to be solved:

$$
\hat{H}|N, k\rangle = E(N, k)|N, k\rangle.
\tag{1.2}
$$

The N-electron state is characterized by the number of electrons N on the QD and a set of quantum numbers $k \geq 0$. In the following, $|N, 0\rangle$ denotes the ground state of the N-electron QD and $|N, k\rangle$ with $k > 0$ denote excited states of the corresponding system. Equation (1.2), can be solved exactly by numerical methods only for a small number of electrons ($N \lesssim 10$). Thus, approximations, e.g. the Hartree-approximation and the Thomas-Fermi-approximation, are introduced, which reduce the complexity of
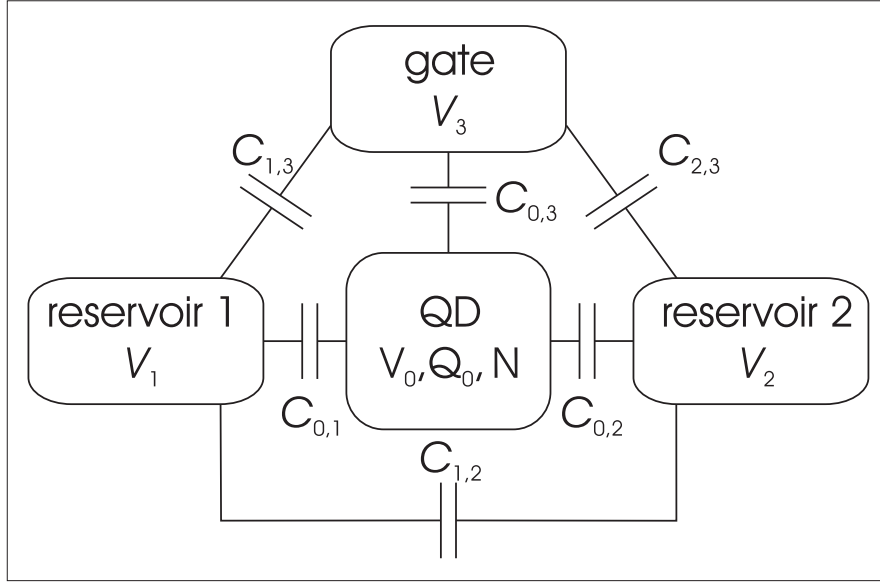
Fig. 1.1: Schematic diagram of the capacitive coupling between QD and nearby electrodes. $C_{i,j}$ with $i, j \neq 0$ describe the capacitive coupling among electrodes. Considering the symmetry properties of the system, the relation $C_{i,j} = C_{j,i}$ applies.

the problem. In these approximations, the N-particle problem is usually reduced to a single particle problem, where the interaction between the electrons is taken into account by an effective interaction potential. The results of these approximations will be used to explain the experimental observations in the quantum Hall regime [Chap. 6], where the confining potential considerably depends on the number of electrons in the QD.

1.1.2 Constant interaction model

For the discussion of the experiments shown in this thesis, it is usually sufficient to describe the QD by a phenomenological model, which is an extension of the pure classical description. Following for example Ref. [Kel01] and referring to Fig. 1.1, the QD can be described as a conductive island that contains an integer number of electrons $N = |Q_0|/e$. Voltages V_i applied to nearby electrodes (electron gas reservoirs, as well as gate electrodes) couple capacitively to the island. The corresponding capacities $C_{i,j}$ are assumed to be independent of the number of electrons. They induce a charge of

$$Q_0 = \sum_{i=1}^{3} C_{0,i}(V_0 - V_i) \tag{1.3}$$

on the QD. Using the total capacity of the QD, $C = \sum_{i=1}^{3} C_{0,i}$, the total potential of the QD is given by

$$V_0 = \frac{Q_0}{C} + \sum_{i=3}^{3} \frac{C_{i,0} \cdot V_i}{C}. \tag{1.4}$$

Thus, the total electrostatic energy $E_{el.stat.}(N)$ needed to charge N electrons onto the QD is

$$E_{el.stat.}(N, V_i) = \int_0^{-eN} V_0(q) dq = -Ne \cdot \sum_{i=1}^{3} \frac{C_{i,0} \cdot V_i}{C} + \frac{(Ne)^2}{2C}. \tag{1.5}$$

In QDs, which are of the size of the de Broglie-wavelength $\lambda_F = h/m^* v_F$, the quantum confinement causes a discrete energy spectrum in the QD. Thus, by increasing the number of electrons on the dot, the energies of the QD states ϵ_p has to be provided in addition to $E_{el.stat.}(N)$. The total energy of the N-electron QD is given by the sum of the classical electrostatic energy and the sum of the occupied QD states[1].

$$E(N) = \sum_{p=1}^{N} \epsilon_p + E_{el.stat.}(N, V_i) \tag{1.6}$$

In the limit $T \to 0$, the electrochemical potential $\bar{\mu}(N+1)$ of the QD, is given by the difference in the ground state energies of the N+1 and N electron system:

$$\bar{\mu}(N+1, 0; N, 0) = E_{N+1} - E_N = \epsilon_{N+1} - e \cdot \sum_{i=1}^{k} \frac{C_i}{C} V_i + (N + 1/2) \frac{e^2}{C}. \tag{1.7}$$

Within this model, the interaction between the electrons is considered by the constant electrostatic energy $E_C = e^2/C$; this is why it is called the *constant interaction model*.

1.2   First and second order transport

While in the previous section the QD was considered as an isolated system, this section presents the basic concepts of the electron transport from adjacent reservoirs through the QD. The overview follows Ref. [KMM$^+$97] and gives an introduction about the basic properties of Coulomb blockade (CB) transport.

In order to accomplish charge transport through the QD in the classical sense, electrons have to be added to and removed from the QD. From Eq. (1.7), it follows that there are two possible ways to change the number of electrons on the QD. First, at constant gate voltage, the number of electrons is increased by one, when the electrochemical potential changes by

$$\bar{\mu}(N+1, 0; N, 0) - \bar{\mu}(N, 0; N-1, 0) = \frac{e^2}{C} + (\epsilon_{N+1} - \epsilon_N) = E_C + \delta E. \tag{1.8}$$

Second, the change in gate voltage ΔV_i which is needed to change the number of QD electrons by one is given by

$$\Delta V_i = \frac{C}{eC_i}(E_C + \delta E). \tag{1.9}$$

---

[1]The QD states can be approximated by the quantum mechanical single particle states. The occupation of theses states results according to Hund's rules [TAH$^+$96]. Their energy is measured with respect to the bottom of the confining potential.
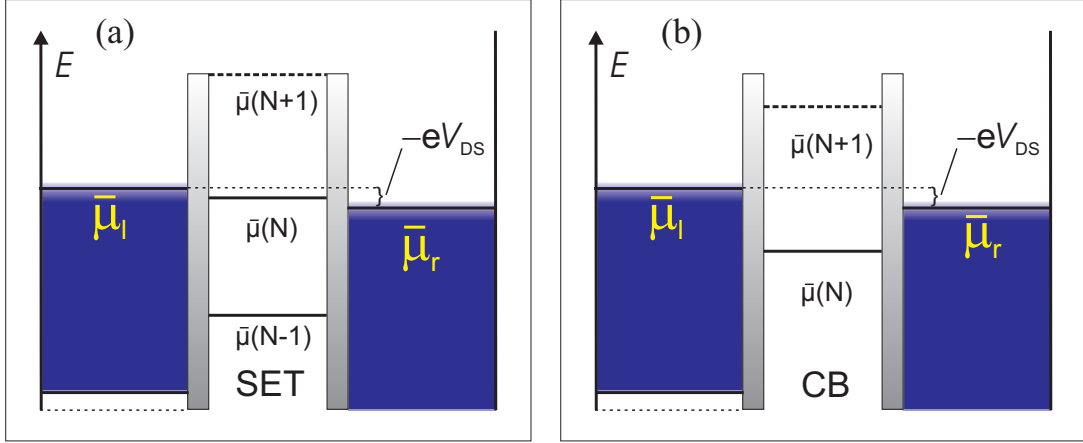
Fig. 1.2: Schematic energy diagram of the QD and the adjacent reservoirs. Panel (a) shows the situation in the case of single-electron-tunneling (SET). Panel (b) depicts the situation, where the transport through the QD is blocked due to Coulomb blockade (CB).

In the first case, the effective charging energy $E_C^* = E_C + \delta E$ has to be provided by the incoming electron from the reservoir. In the second case, E_C^* originates from the electric field energy of the continuously variable mirror charge on electrode i.

In order to observe these sequential charging effects,[2] the thermal excitations have to be small compared to the effective charging energy ($k_B T \ll E_C^*$), and the electrons have to be localized either in the QD or in the reservoirs. The latter requirement is satisfied, if the time required to change the number of electrons on the QD, $\Delta t = R_t C$, is large compared to the fundamental measurement time limit, which is given by the Heisenberg uncertainty principle

$$\Delta E \Delta t = \frac{e^2}{C} R_t C > h. \tag{1.10}$$

Thus, electrons are classically localized either in the reservoir or in the QD, when the tunnel (transfer) resistance $R_t \gg h/e^2$.

In this thesis, this basic model of the so called (extended) orthodox Coulomb blockade will be taken as the starting point for the investigations of further thermoelectric transport phenomena. In the following, some results of the orthodox model are reviewed and their application to the linear and nonlinear transport is discussed.

1.2.1   First order linear transport

Figure 1.2 depicts the potential landscape of a QD in the regime of linear transport. The QD is separated by two tunneling barriers from the reservoirs, which are characterized by

---

[2]This phenomenon was first reported by Gorter in 1951 [Gor51].

their electro-chemical potentials $\bar{\mu}_{l,r}$ and their temperature T. The occupation probability of states in the reservoirs is given by the the Fermi distribution

$$f(E, T, \mu) = \frac{1}{e^{\frac{E-\mu}{k_B T}} + 1}. \tag{1.11}$$

The relative position of the QD electrochemical potential can be varied reversibly by a gate voltage (V_{P}). A current can be driven through the QD when the electrochemical potential of the QD lies between the Fermi energies of the reservoirs [cf. Fig.1.2(a)] by means of a small bias voltage V_{DS} applied between the left and the right reservoirs, where $eV_{\mathrm{DS}} < k_B T$. In the first step, an electron, which has enough energy, enters the QD from the left reservoir and increases the number of electrons from $N-1$ to N. In the second step, an electron from the QD tunnels into the free states of the right reservoir. Of course, the electron which is leaving the QD has to have enough energy to occupy the free state in the lead. The transport of electrons is blocked, if $\bar{\mu}(N) < \bar{\mu}_{l,r} < \bar{\mu}(N+1)$ [situation depicted in Fig. 1.2(b)]. Neither have the electrons in the reservoir enough energy to increase the number of electrons on the dot from N to $N+1$, nor can an electron from the dot tunnel into the reservoirs, since all states of the same energy are occupied. Upon increasing the gate voltage continuously ($\Delta V_{\mathrm{P}} = V_{\mathrm{P},f} - V_{\mathrm{P},i} > 0$), the number of electrons is increased successively. Each time the electrochemical potential of the QD is aligned between the Fermi edges of the reservoirs, an electric current I can flow through the QD, and a single-electron-tunneling (SET) conductance peak results in the linear conductance $G = \lim_{V_{\mathrm{DS}} \to 0} I/\Delta V_{\mathrm{DS}}$.

For first order transport (sequential tunneling), a linear-response theory has been presented in Ref. [Bee91]. This theory describes the Coulomb blockade conductance oscillations quantitatively. The theory extends the classical theory of Coulomb blockade oscillations by Kulik and Shekhter [She73, KS75] to the regime where the influence of the charging energy on resonant tunneling is formulated for a QD with discrete energy spectrum and which is weakly coupled to two electron reservoirs. The model assumes that the thermal energy exceeds the width of the transmission resonance $k_B T \gg h\Gamma_{l,r}$, i.e. the SET conductance peaks are thermally broadened. The QD states are equally spaced and the coupling does not depend on the energy. It should be noted that the model assumes that the distribution of electrons among the levels in the QD is given by the Gibbs distribution, and this differs from the Fermi-Dirac distribution in the case $k_B T \approx \delta E$.

In the regime of the classical Coulomb blockade ($k_B T \ll \delta E$) and in the regime of the quantum Coulomb blockade ($\delta E \ll k_B T$), the line shape of the SET conductance peaks can be expressed by

$$
\begin{aligned}
G &= \frac{e^2 \rho}{2} \frac{\Gamma_l \Gamma_r}{\Gamma_l + \Gamma_r} \cosh^{-2}\left(\frac{\Delta_{min}}{2 k_B T}\right) \\
&\quad \text{if } k_B T \ll \delta E,
\end{aligned} \tag{1.12}
$$

$$
\begin{aligned}
G &= \frac{e^2}{4 k_B T} \frac{\Gamma_l \Gamma_r}{\Gamma_l + \Gamma_r} \frac{\Delta_{min}/k_B T}{\sinh(\Delta_{min}/k_B T)} \approx \frac{e^2}{4 k_B T} \frac{\Gamma_l \Gamma_r}{\Gamma_l + \Gamma_r} \cosh^{-2}\left(\frac{\Delta_{min}}{2.5 k_B T}\right) \\
&\quad \text{if } \delta E \ll k_B T.
\end{aligned} \tag{1.13}
$$

Here, ρ denotes the density of states in the QD, and $\Delta_{min} = \bar{\mu}_{QD}(N) - \bar{\mu}_{l,r}$ the minimum energy gap between the electrochemical potentials of QD and reservoirs. This theory is used to fit the line shape of the SET conductance peaks obtained by linear conductance measurements. The fit allows the temperature of the electron gas to be extracted, since the charging energy of the QD can be obtained independently by nonlinear conductance measurements. In order to fit the SET conductance peaks in the intermediate temperature regime ($k_B T \ll \delta E$), the exact equations have to be used. These are given in Chap. 4, where a comparison between first and second order transport processes with respect to the thermoelectric transport behavior is given.

1.2.2 Elastic and inelastic cotunneling

In linear response, the sequential charge transport through the QD is mainly mediated by thermally activated electrons in the leads and the QD. An increasing energy gap between the electrochemical potential of the QD and the Fermi energies of the adjacent reservoirs (E_g) leads to an exponential suppression of the QD conductance away from the SET conductance peak. This is also reflected in Eqs. (1.12) and (1.13). Quantum mechanically, however, the electrons of the leads do not necessarily need the excitation energy E_g (with respect to the Fermi energy) to traverse the QD. Tunneling through the QD is possible by means of the virtual occupation of an intermediate state. This so called second order transport (cotunneling) decreases according to a power law behavior with increasing E_g. Thus, for low enough temperatures, conduction is mediated by cotunneling processes in the conductance valleys between CB resonances [AN90, GAM90, HTT92]. Figure 1.3 shows a schematic energy diagram of an inelastic cotunneling process. Initially the QD is in the N electron ground state. An electron from the reservoir enters the QD and transfers the QD into a virtual intermediate ($N+1$)-electron state. Then, a second electron leaves the QD to the second reservoir, and the QD ends in an excited N-electron state. The energy difference δE between the initial and the final QD states is provided by the tunneling electron entering the QD. Since the energy of the total process has to be conserved, the intermediate ($N+1$)-electron QD state can only be occupied virtually.

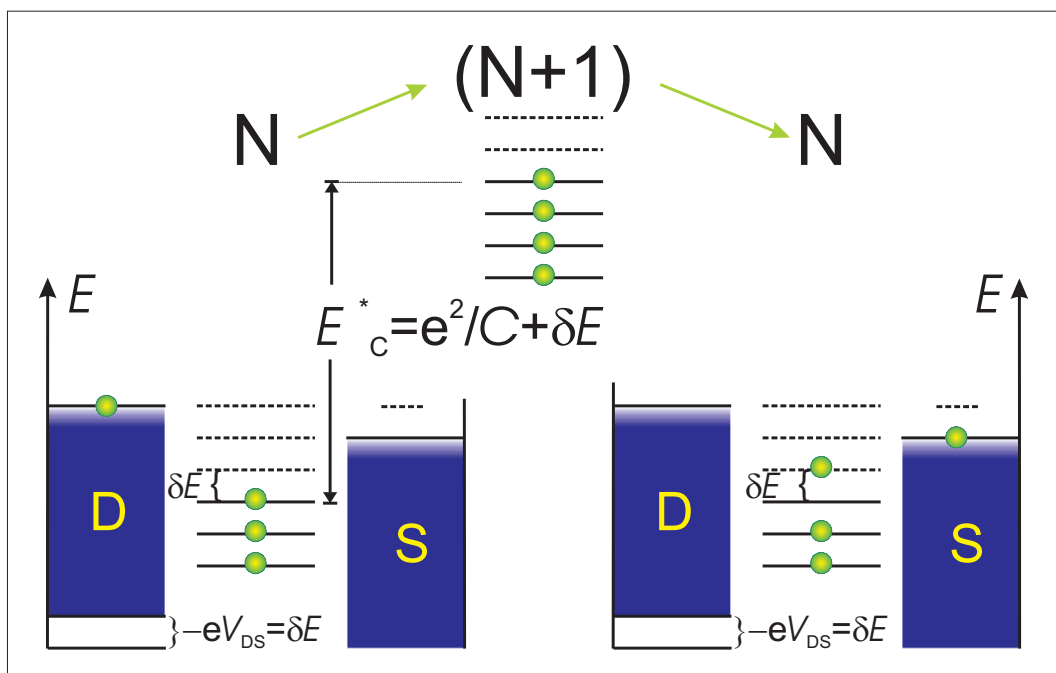**Fig. 1.3:** Schematic energy diagram of an inelastic cotunneling process. From left to right: initially the QD is in the N electron ground state, then it is transferred into a virtual intermediate $N + 1$-electron state and finally ends in an excited N-electron state. The energy difference δE between the initial and the final QD states is provided by the tunneling electron entering the QD.

Figure 1.3 depicts just one possible contribution to the cotunneling. For the complete description of cotunneling transport, other possible intermediate excited states also have to be included, as well as hole-like excitations of the QD. Cotunneling processes can be either elastic (coherent) or inelastic (incoherent), depending on whether the dot is left in its ground state or is left in an excited state after the charge transfer, respectively [DFSE$^+$01]. Their contributions to the average conductance are respectively:

$$\langle G_{\mathrm{el}} \rangle = \frac{\hbar G_{\mathrm{l}} G_{\mathrm{r}} \delta E}{4\pi e^2} \left(\frac{1}{E_e} + \frac{1}{E_h} \right) \tag{1.14}$$

$$\langle G_{\mathrm{in}} \rangle = \frac{\hbar G_{\mathrm{l}} G_{\mathrm{r}} \pi}{3 e^2} (k_B T)^2 \left(\frac{1}{E_e} + \frac{1}{E_h} \right)^2, \tag{1.15}$$

where $G_{l,r}$ denote the conductances of the left and the right tunnel barrier, E_e and E_h the energy differences between the Fermi energy of the reservoirs and the electrochemical potential of the corresponding QD state above or below E_F. Note that the tunneling rates depend on the characteristic time scale $\tau = E_{\mathrm{C}}^*/\hbar$, since $E_{e,h}$ are of the order of E_{C}. This is a consequence of the Heisenberg principle and corresponds to the time which the electron can spend propagating via the virtual state from one reservoir to the other.

1.3 Nonlinear transport

In the previous sections, it was shown that charge transport through QDs can be accomplished by various transport mechanisms. Experimentally, the transport of charges results in a measurable current. For a given set of external experimental parameters P_i, defining the potential differences between the QD reservoirs and the gate voltages, the current is proportional to the transmission probability of electrons through the QD. In the framework of the Landauer-Büttiker formalism [Lan57, Lan70, BILP85, Büt86], the *change* of the current dI due to a *change* in the potential difference dV_{DS} between the two connecting reservoirs (source and drain) is interpreted as a change in the transmission probability at a given set of external parameters P_i. Thus, the differential conductance dI/dV_{DS}, reflects the strength of the change in the transmission probability, which is either due to an increasing or a decreasing number of transport channels or transport mechanisms.

During the last two decades, a large number of investigations involving finite-bias differential conductance measurements on QDs in the Coulomb blockade and SET transport regimes were carried out. The advances in measurement techniques have lead to a far-reaching understanding of the interpretation of these measurements. In the following, a short introduction to the interpretation of such measurements by means of graphs is given. The actual experimental technique is described in Chap. 3.
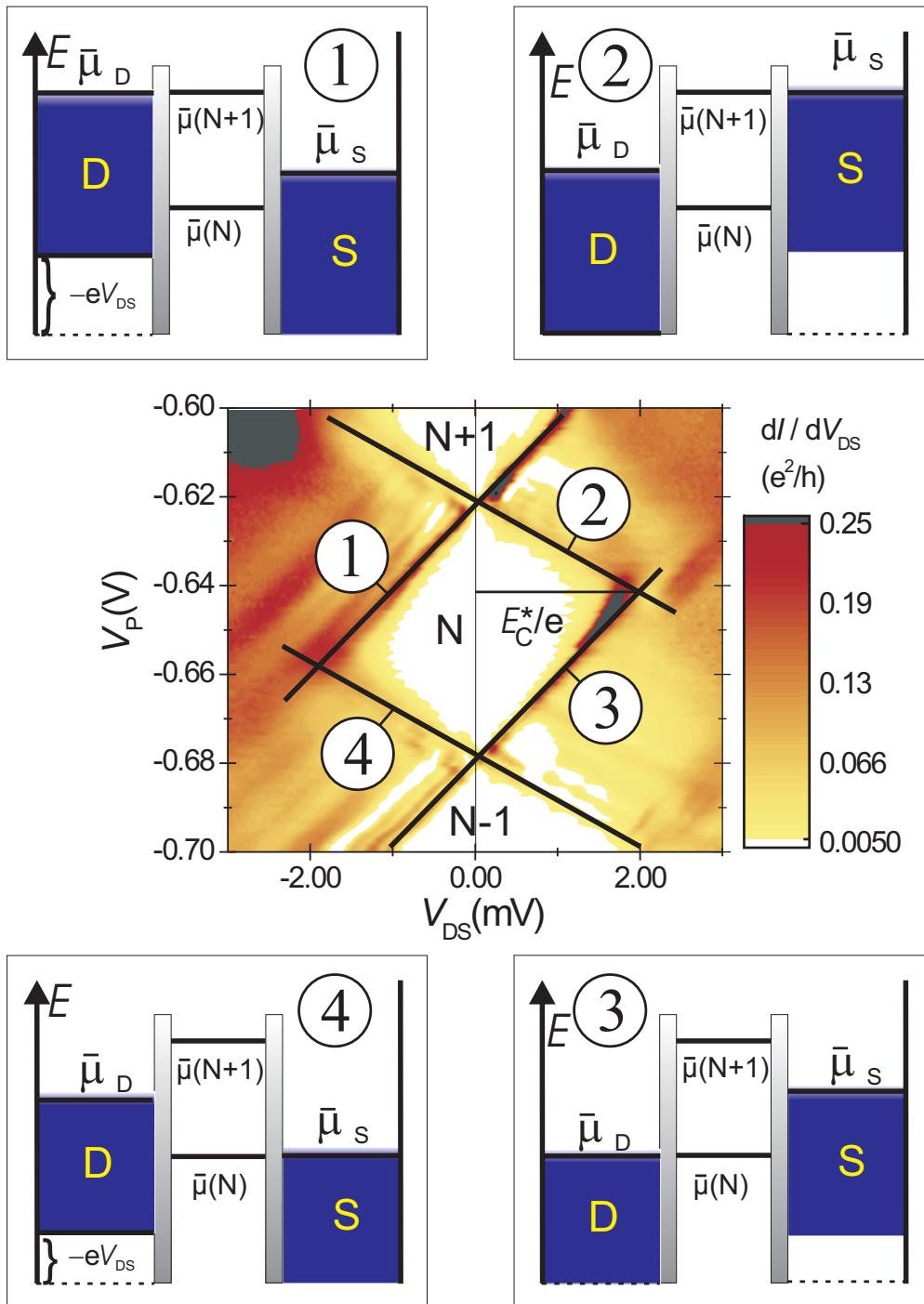
Fig. 1.4: Color scale plot of the nonlinear differential conductance (middle panel) and corresponding schematic energy diagrams of the transitions from Coulomb blocked transport to the single electron tunneling regime [(1)-(4)]. Black lines are added as a guide to the eye for the cases, where either source or drain is aligned with the electrochemical potential of the QD.

1.3.1   Coulomb Blockade Diamonds

The middle panel of Fig. 1.4 shows a color scale plot of the nonlinear differential conductance as a function of the gate voltage V_{P} and applied drain-source voltage $V_{\mathrm{DS}} = -(\bar{\mu}_D - \bar{\mu}_S)/e$. Dark and bright colors correspond to high and low differential conductance, respectively. In the middle, a region of low dI/dV_{DS} indicates the transport regime, where the charge transport is blocked. Here, the electrochemical potentials of the source and the drain contacts lie between the electrochemical potentials of the N and $(N + 1)$-electron QD, i.e.

$$\bar{\mu}_{N,0}(V_{\mathrm{P}}) < \bar{\mu}_D, \; \bar{\mu}_S < \bar{\mu}_{N+1,0}(V_{\mathrm{P}}). \tag{1.16}$$

Black lines are added as a guide to the eye at the border lines of the Coulomb blockaded transport regime. Outside this Coulomb blockade diamond, sequential charge transport sets in, since the electrochemical potential of the QD lies between the electrochemical potentials of the reservoirs. The schematic energy diagrams [(1)-(4)] depict the situations, where either the drain contact [lines (2) and (4)] or the source contact [lines (1) and (3)] are aligned with the electrochemical potentials of the QD ground states. The slopes of lines (2) and (4) m_S, and (1) and (3) m_D depend on the capacitive coupling of the reservoirs and the gates to the QD. Taking the source potential to be constant,[3] the latter (m_D) can be calculated by considering that the change in the QD energy $\Delta E_{QD} = -eV_{\mathrm{DS}}$ is equal to the energy shift due to the capacitive coupling of the drain contact ($\Delta E_D = -e\frac{C_D}{C}V_{\mathrm{DS}} = -ec_D V_{\mathrm{DS}}$) and to the gate voltage ($\Delta E_{V_{\mathrm{P}}} = -e\frac{C_P}{C}V_{\mathrm{P}} = -ec_P V_{\mathrm{P}}$) so that

$$\begin{aligned} \Delta E_{QD} &= -eV_{\mathrm{DS}} = -e\left(\frac{C_D}{C}V_{\mathrm{DS}} + \frac{C_P}{C}V_{\mathrm{P}}\right) \\ &\Leftrightarrow \quad \frac{\Delta V_{\mathrm{P}}}{\Delta V_{\mathrm{DS}}} = m_D = \frac{1 - c_D}{c_P}. \end{aligned} \tag{1.17}$$

In a similar way, the slope of lines (2) and (4) m_S can be calculated. Here, the electrochemical potential is aligned with the fixed electrochemical potential of the source, and $\Delta E_D = -ec_D V_{\mathrm{DS}}$ has to be compensated by $\Delta E_{V_{\mathrm{P}}} = -ec_P V_{\mathrm{P}}$:

$$\begin{aligned} \Delta E_{QD} &= 0 = -e\left(\frac{C_D}{C}V_{\mathrm{DS}} + \frac{C_P}{C}V_{\mathrm{P}}\right) \\ &\Leftrightarrow \quad \frac{\Delta V_{\mathrm{P}}}{\Delta V_{\mathrm{DS}}} = m_S = -\frac{c_D}{c_P}. \end{aligned} \tag{1.18}$$

The scaling factor $\alpha = E_{\mathrm{C}}^*/\Delta V_{\mathrm{P}}$, which can be obtained from the transport spectrum directly for an estimate, is then given by

$$\alpha = \frac{1}{m_D - m_s}. \tag{1.19}$$

---

[3] In the experiments, the source contact is usually connected to an I-V converter, which keeps V_S on virtual ground ($V_S = 0$).

The value of α has to be determined separately for each QD-sample. It is constant only in the case of constant capacities c_i. In few-electron QDs, this is not quite the case and α has to be determined for each Coulomb blockade diamond.

1.3.2   Transport via excited states in the SET regime

So far, the sequential tunneling via the ground states of the QDs $\bar{\mu}(n,0)$ has been considered. However, the excited states $\bar{\mu}(n,i)$ with $i\epsilon\mathbb{N}^+$ also contribute to the sequential tunneling transport in the SET regime once the corresponding electrochemical potentials are between $\bar{\mu}_D$ and $\bar{\mu}_S$. The increase or decrease in the transmission probability of electrons through the QD results in a positive or negative dI/dV_{DS} in a line parallel to the edge of the Coulomb blockade diamond, respectively. Figure 1.5 shows the schematic energy diagrams, of the situations where either the first excited state of the $(N+1)$-electron system [(1) and (2)] or the N-electron system [(3) and (4)] participates in the transport. In Fig. 1.5, panels (1)-(4) depict special situations, where the electrochemical potentials of the QD are aligned with $\bar{\mu}_S$ or $\bar{\mu}_D$. The schematic color-scale plot shows the positions of the expected structures caused by $\bar{\mu}(N+1,1;N,0)$ and $\bar{\mu}(N+1,0;N,1)$ in dI/dV_{DS} as dashed and dotted lines, respectively.

The level spacing is given by $e\Delta V_{\mathrm{DS}}^*$, where ΔV_{DS}^* is the difference in applied drain-source voltage between the intersection points of the dashed lines with the CB diamond border (red dots in Fig. 1.5).

Note that only transitions which involve the participation of the ground state intersect with the CB diamond border (red dots in Fig. 1.5), and those of the type $\bar{\mu}(N+1,i;N,j)$ with $i,j>0$ do not. In order to obtain the level spacing of these transitions, their lines have to be extrapolated to the border of the CB diamond.

1.3.3   Cotunneling in the CB regime

Corresponding to Sec. 1.2.2, charge transport through the QD is not completely blocked within the Coulomb blockade diamond. Elastic and inelastic cotunneling takes place via virtual intermediate, excited states of the QD. Cotunneling only depends on the coupling of the QD states to the reservoirs and the charging energy of the QD, provided energy conservation is obeyed. An increase in the conductance independent of gate voltage is expected within the CB diamond once the $e\Delta\bar{\mu}| > \delta E$, since inelastic cotunneling transport is mediated via the discrete excited energy states [see also Fig. 1.3]. Figure 1.6 shows a Coulomb blockade diamond where strong inelastic cotunneling sets in for $V_{\mathrm{DS}} > 0.5$ mV. A corresponding increase is also observable for $V_{\mathrm{DS}} < -0.5$ mV, though less pronounced. Red dashed lines have been added as a guide to the eye. At the diamond edges, the cotunneling lines connect to lines where first order tunneling via the corresponding excited state sets in. For these points, the panels (1)-(4) depict the schematic energy diagram, where the ground state transitions are aligned with source or drain, respectively.
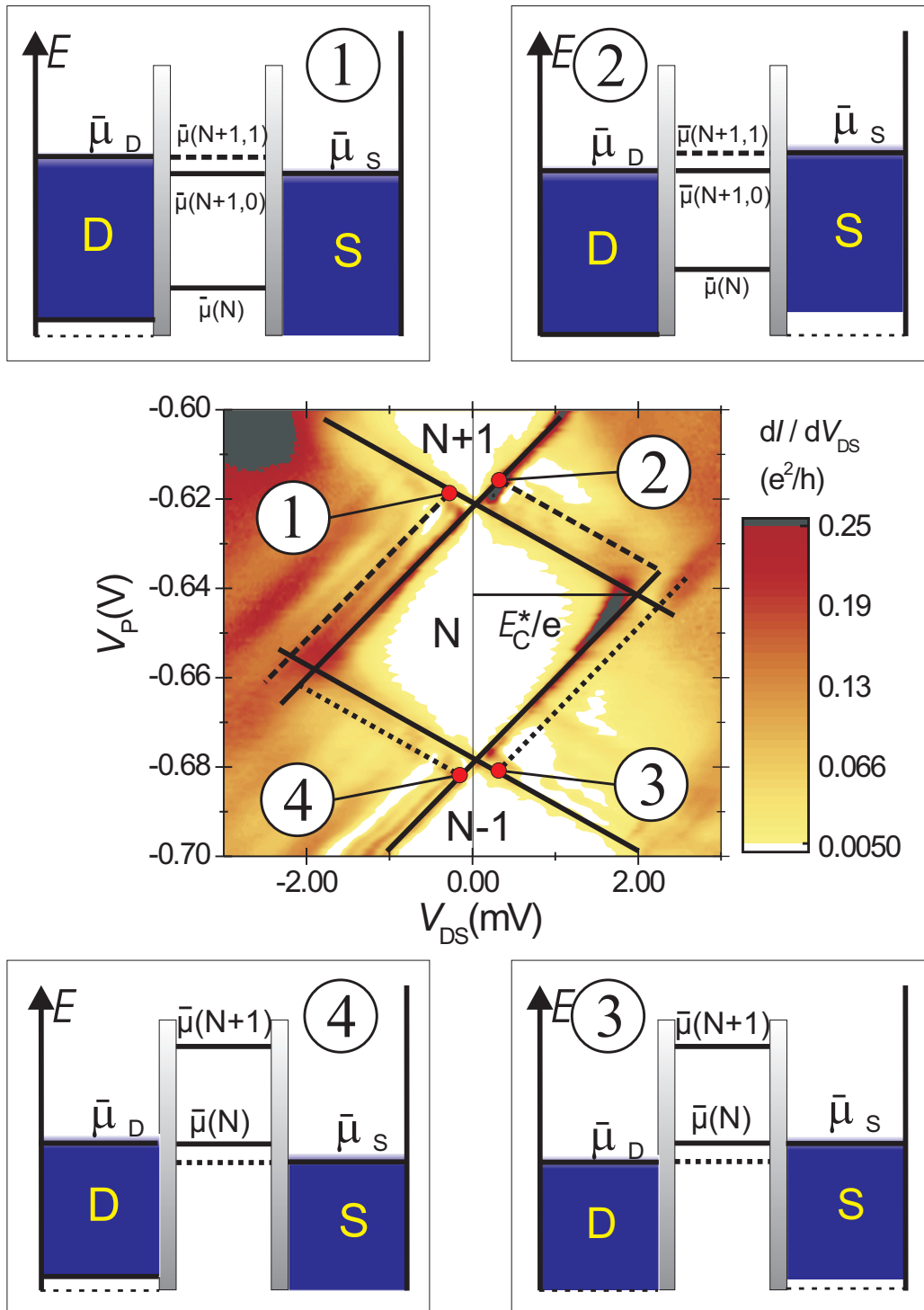
Fig. 1.5: Color scale plot of the nonlinear differential conductance (middle panel). For the positions of the red dots, the corresponding schematic energy diagrams [(1)-(4)] are added. Here, an excited state of the QD becomes available for transport in addition to the ground state transitions (SET regime). Full or dashed, black lines are added as a guide to the eye in the cases where either source or drain is aligned with the electrochemical potential of the QD ground or excited state, respectively.
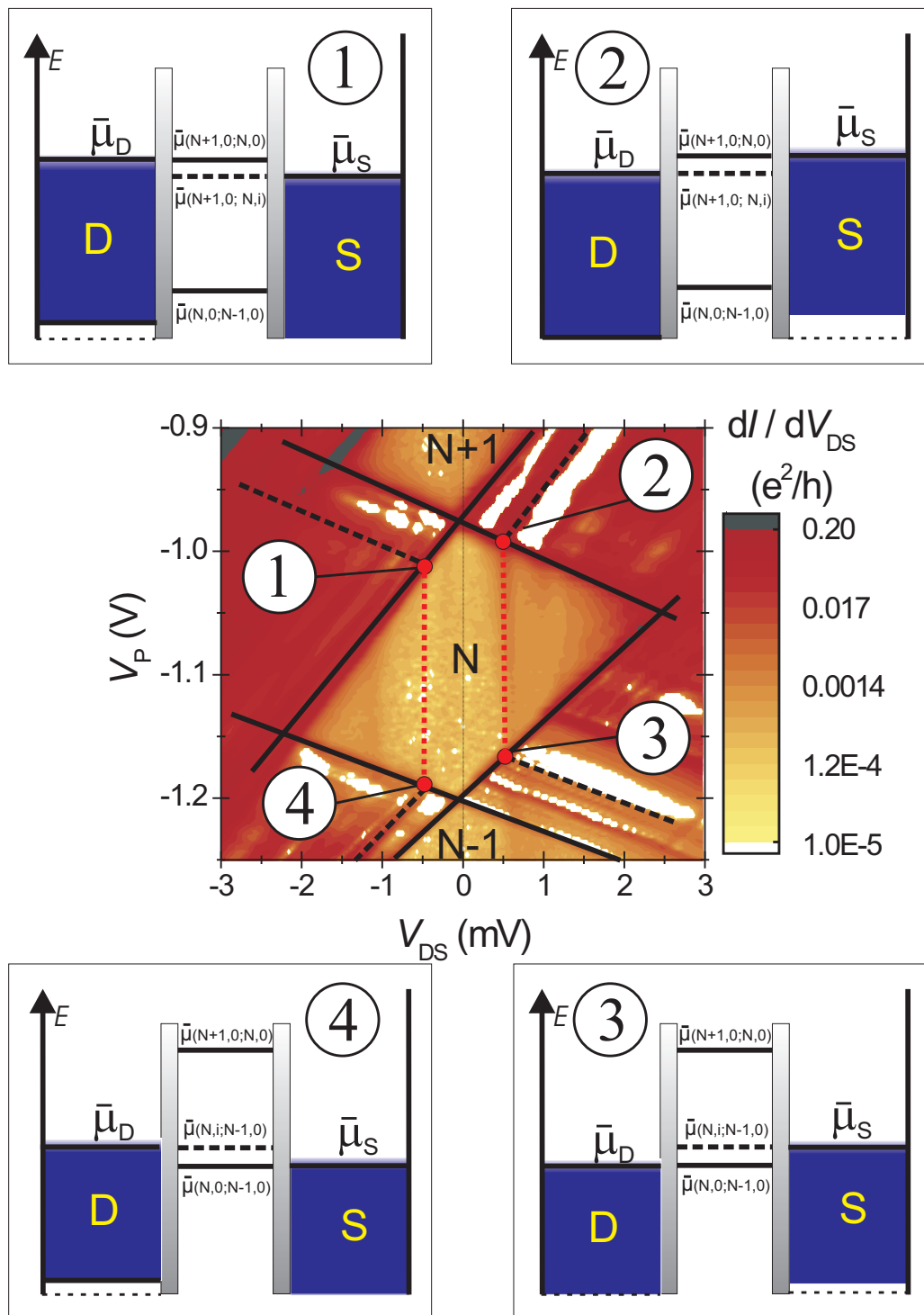
Fig. 1.6: Logarithmic color-scale plot of a Coulomb blockade diamond (middle panel). The red dotted lines indicate the edges of beginning conductance contributions due to cotunneling. Schematic energy diagrams are added for the QD configurations marked by red dots [(1)-(4)]. Here, transport is mediated via sequential tunneling using the QD ground states (black, solid lines) and excited states (black, dashed lines) and inelastic cotunneling (red, dotted lines).

The onset of inelastic cotunneling is characterized by its width. In the zero temperature limit, this width is determined by the lifetime broadening of the excited state.

In summary, the V_{DS}-V_P plane which contains the Coulomb blockade diamonds can be divided into areas corresponding to the various transport processes. Figure 1.7 presents a schematic drawing of the various tunneling regimes within a Coulomb blockade diamond [Tew04, SIR$^+$05]. Here, only one excited state is taken into account. It has an energy difference to the ground state of δE. For energy differences between the electrochemical potentials of source and drain smaller than the level splitting, ($\Delta\bar{\mu} < \delta E$), only elastic cotunneling is possible within the Coulomb blockade diamond (yellow area). Once $\Delta\bar{\mu} > \delta E$, inelastic cotunneling processes (can) set in (blue and orange area). If the QD remains in the excited state after an inelastic cotunneling process, the effective charging energy is reduced by the amount of the level spacing. In this case, it is possible that sequential tunneling occurs even *within* the CB diamond (blue area).
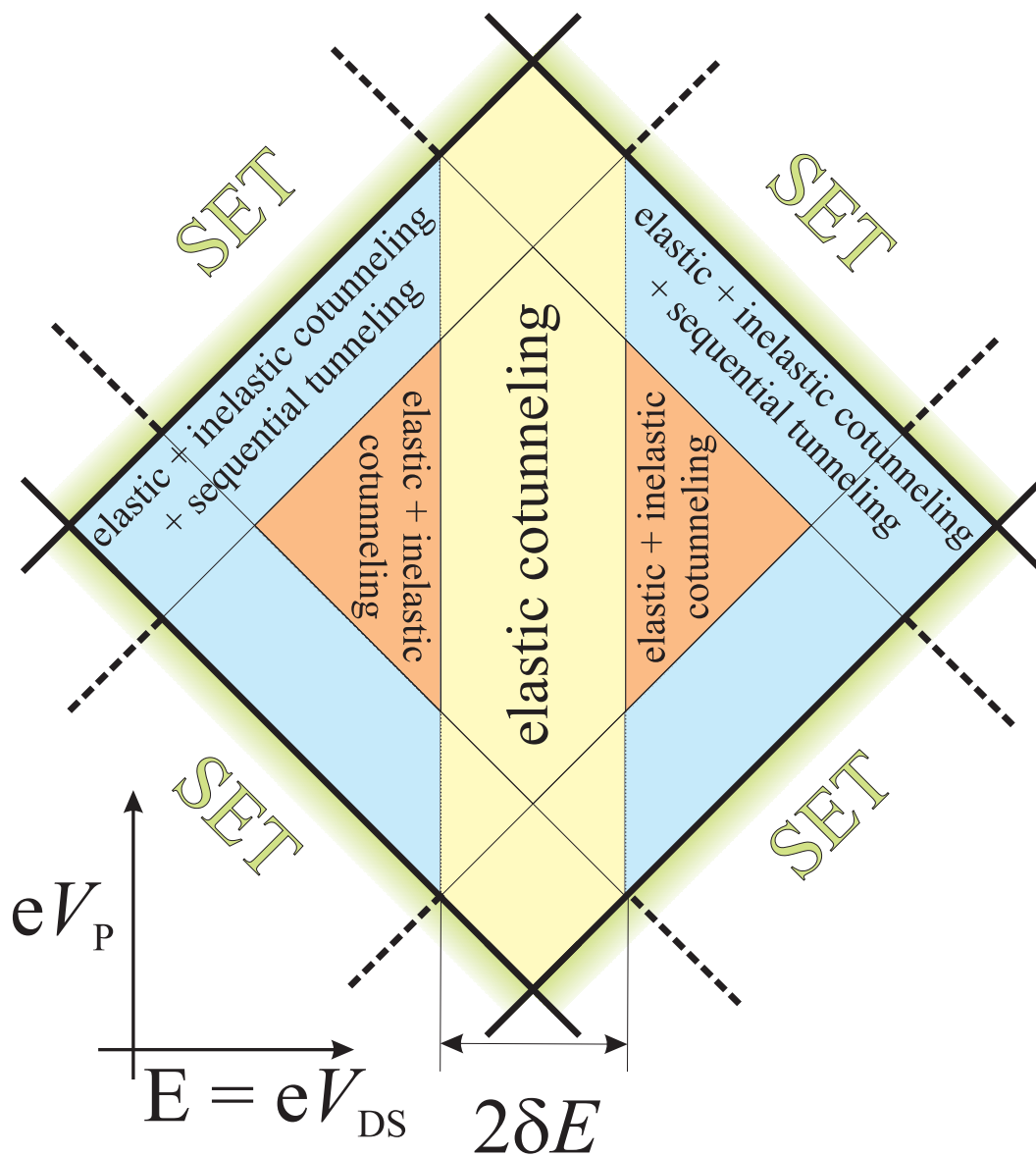
Fig. 1.7: Schematic drawing of the various tunneling regimes within the Coulomb blockade according to Refs. [Tew04] and [SIR$^+$05]. Thick solid lines correspond to the edges of the CB diamond. δE denotes the energy difference between the ground state and the first excited state.

Chapter 2

Fundamentals of thermoelectric transport

2.1 General considerations

The measurement of the thermoelectric properties of a system provides an alternative way to study transport of charged particles besides the common electric transport measurements. It also yields additional information about the dynamic processes during charge transport [Mah81]. For a detailed study, an introduction on thermoelectricity can be found in Ref. [Bar72]. Here, only the most important basics will be given in a short résumé.

In general, if one side of a conductor is heated, electrons at the hot end will acquire increased energy relative to the cold end and will diffuse to the side where their energy may be lowered.[1] The heat flow is accompanied by the accumulation of negative charge at the cold end, thus setting up an electric field or a potential difference ($V_{\mathrm{T}} = e^{-1}\Delta\bar{\mu} = e^{-1}\Delta(\mu - eV)$) between the two sides of the device. The electric field builds up until a state of dynamic equilibrium is established between electron flux due to the temperature difference ΔT and the electron flux due to the potential difference caused by the accumulation of electrons at the cold end. This phenomenon is considered to be the basic thermoelectric effect. In this sense, thermoelectricity concerns the direct generation of an electromotive force (e.m.f) by thermal means. This e.m.f. is called the Seebeck e.m.f. after its discoverer Johann Seebeck (1770-1831). In the limit of zero electrical current flow, the quotient

$$S \equiv -\left.\frac{V_{\mathrm{T}}}{\Delta T}\right|_{I=0} \tag{2.1}$$

is called the thermoelectric power or thermopower S. In the stationary state, the electrical energy which is required to transfer n electrons from the hot end to the cold end is

---

[1]This is essentially the manner in which heat is conducted through the device.

balanced by the change in thermal energy (that is, the heat $Q = \mathbb{S}T$), and it is possible to approximate: $neV_{\mathrm{T}} = \mathbb{S}_n \Delta T$; where n is the particle density and $\mathbb{S}_n$ is the entropy density of the charge carriers corresponding to the average potential and temperature of the sample [ZMFB05]. This results in the approximate relationship between the Seebeck coefficient and the entropy

$$S \equiv \frac{\mathbb{S}_n}{en}. \tag{2.2}$$

This is why the thermopower is often interpreted as entropy per charge carrier.

The described basic thermoelectric effect leads to a negative thermopower coefficient. However, the correct sign and the magnitude of the thermoelectric parameters for various materials strongly depend on the temperature, the type of conduction (p or n type) and the scattering interactions which charge carriers experience in their motion under a temperature gradient. If the electrons travelling down the temperature gradient are scattered in the same way as the electrons travelling upwards, the scattering would be expected to play no part in the determination of the thermopower. If the scattering is energy dependent, it might be that low energy electrons moving to the hot end would encounter less scattering than those moving to the cold end, thus resulting in a positive thermopower. Vice versa, it is possible that high energy electrons moving to the cold end encounter less scattering than those moving to the hot end, which results in an enhanced negative thermopower. Thus, the energy dependence of the scattering mechanisms is intimately related to the thermoelectric response. This simple example shows that by measuring the thermoelectric response of a material or a device, conclusions can be drawn about the dynamics of the charge carriers during the transport from the hot to the cold reservoir.

In this thesis, the thermoelectric response is investigated with respect to the underlying transport scattering mechanisms in single artificial impurities (QD) which are mostly known from studies of the electric conductance. In order to clarify the connection between conductance and thermopower measurements, the underlying thermodynamic concept is summarized in the following section.

2.1.1 Thermodynamics of irreversible processes

In bulk thermoelectricity, the flow of heat and charge under the action of an electric potential and a temperature gradient is considered. Reversible processes (Peltier and Thomson effects) take place simultaneously with irreversible processes (Joule heating and thermal conductance). In 1931, Onsager (Refs. [Ons31a, Ons31b]) derived relationships between the macroscopic observables by taking into account the irreversible processes. He presented a method, which relates the 'fluxes' in a system to the 'forces' present. Provided the 'forces' are not too large, linear relations exist between them and their appropriate 'fluxes'. In linear response there are currents $\mathbf{J_i}$ which flow as a result of forces $\mathbf{X_i}$ on the system. These forces might be temperature gradients, or electric fields,

or concentration gradients, which are expressed as gradients of the chemical potential. Linear response assumes that these are proportional and the system may be represented by a set of phenomenological or macroscopic transport equations of the form:

$$\mathbf{J}_i = \sum_j \mathbf{Z}_{ij} \cdot \mathbf{X}_j. \tag{2.3}$$

The coefficients $\mathbf{Z}_{ij}$ are the measurable quantities and may be divided into two classes, those with equal subscripts, which are associated with primary flows under primary forces and those with unequal subscripts which relate primary flows with interference or coupling forces. According to the analysis given by Onsager in which small deviations from the equilibrium state were considered at the molecular level, the reciprocal relationship

$$\mathbf{Z}_{ij} = \mathbf{Z}_{ji} \tag{2.4}$$

holds provided that the choice of the flows and forces are governed by given rules. The reciprocal relationship can be seen as axiomatic and reflects the reversible nature of the microscopic processes, i.e. the time invariance of classical and quantum mechanical equations of motion [dG63]. The adequate choice of the flows and forces results from the consideration of the entropy production in an adiabatic isolated system. The entropy production $d\bar{S}/dt$ is given by the product of the primary flows and primary forces

$$\frac{d\bar{S}}{dt} = \sum_i \mathbf{J}_i \mathbf{X}_i. \tag{2.5}$$

Provided that $d\bar{S}/dt$ remains unchanged, various specifications of the macroscopic transport equations are possible. One possible specification is given by

$$\begin{pmatrix} J \\ J_Q \end{pmatrix} = \begin{pmatrix} -\frac{Z_{11}}{T} & -\frac{Z_{12}}{T^2} \\ -\frac{Z_{21}}{T} & -\frac{Z_{22}}{T^2} \end{pmatrix} \begin{pmatrix} \nabla\bar{\mu} \\ \nabla T \end{pmatrix}, \tag{2.6}$$

where $J = -I/|e|$ is the particle current, J_Q is the heat current, $\bar{\mu} = \mu - |e|V$ is the electrochemical potential. Obviously $Z_{ik} = Z_{ki}$ holds within this choice of representation. However, very often, more convenient representations are chosen. For example, the following representation can be chosen

$$\begin{pmatrix} I \\ J_Q \end{pmatrix} = \begin{pmatrix} L_{11} & L_{12} \\ L_{21} & L_{22} \end{pmatrix} \begin{pmatrix} e^{-1}\nabla\bar{\mu} \\ \nabla T \end{pmatrix}, \tag{2.7}$$

where the conductivity σ, the diffusion thermopower S, the Peltier coefficient π and the thermal conductivity κ are given by

$$\sigma = L_{11}, \tag{2.8}$$

$$S = -\frac{L_{12}}{L_{11}}, \tag{2.9}$$

$$\pi = \frac{L_{21}}{L_{11}}, \tag{2.10}$$

$$\kappa = \frac{L_{21}L_{12}}{L_{11}} - L_{22}. \tag{2.11}$$

Note that in measuring the thermal conductivity κ, the heat flow is not measured under the condition $\nabla\bar{\mu} = 0$ but with $I = 0$. This is the origin of the first term of Eq. (2.11). When an isolated sample is subjected to a temperature difference, as it is in the typical arrangement for the measurement of κ, a potential difference exists between the two heat reservoirs. Due to the thermoelectric effect, a difference in the electrochemical potential develops ($\Delta\bar{\mu} = -L_{12}/L_{11}\Delta T$).

In this representation, the reciprocal Onsager relation is reflected by

$$S = \pi/T, \tag{2.12}$$

which is the so called the first Kelvin relation.

So far, only the macroscopic transport equations of bulk materials have been regarded. In the next section, the results of the extension to the field of microstructures is given.

2.1.2   Thermoelectric transport in microstructures

The general considerations of the thermodynamics of irreversible processes has been extended by Sivian and Imri, and Butcher [SI86, But90] to the physics of microstructures. In analogy to the Landauer-Büttiker formalism [Lan57, Lan70, BILP85, Büt86], one can express the thermal and thermoelectric transport matrices (coefficients) in terms of the scattering matrix **S** for a microstructure. In this model, the elastic scatterer (microstructure) is fed by two ideal leads each supporting a certain number of conduction channels. The leads are driven by heat and electron reservoirs with chemical potentials μ_1, μ_2 and temperatures T_1, T_2, respectively. The thermalization of the electrons by inelastic scattering, and hence Joule energy dissipation, occurs only in the heat reservoirs and not in the system itself. It is assumed that the heat reservoirs maintain a Fermi distribution.

In the measurement of a microstructure, only the total fluxes of charge and heat in each reservoir or terminal are accessible. Thus, the conductance between the reservoirs is defined as the total current divided by the potential difference between them. Similarly, the other transport coefficients are expressed in terms of temperature and potential differences instead of the gradients. The transport equations may then be written in the following way [GBJB95]

$$\begin{pmatrix} I \\ J_Q \end{pmatrix} = \begin{pmatrix} L_{11} & L_{12} \\ L_{21} & L_{22} \end{pmatrix} \begin{pmatrix} e^{-1}\Delta\bar{\mu} \\ \Delta T \end{pmatrix}, \tag{2.13}$$

where the macroscopic observables are given by

$$G = L^{(11)}, \tag{2.14}$$
$$S = -L^{(21)}/L^{(11)}, \tag{2.15}$$
$$\Pi = L^{(22)}/L^{(11)}, \tag{2.16}$$
$$\kappa = (L^{(21)}L^{(12)}/L^{(11)}) - L^{(22)}. \tag{2.17}$$

The total particle current carried by one mode n in the left lead is then

$$J_n \propto \int_{-\infty}^{\infty} D_n(E)v_n(E)f_L(E)t(E)dE. \tag{2.18}$$

Regarding the leads to the microstructure as 1D particle waveguide systems, J_n can be simplified, since the energy dependence of the density of states $D(E) \propto \sqrt{E}^{-1}$ and the group velocity $v_n \propto \sqrt{E}$ cancel each other. The transport coefficients can be evaluated accordingly using the following expression for the total generalized current between the reservoirs [GBJB95]:

$$J_{tot} = J_L - J_R = \int_{-\infty}^{\infty} dE \left(\frac{\Lambda}{h}\right) [f_L(E,T) - f_R(E,T)]t(E,T). \tag{2.19}$$

Here, Λ is equivalent to either the electron charge $-e$, which is used for the calculation of the charge current or to the kinetic energy $(E - \bar{\mu})$ carried by an electron, which is used for the calculation of the heat currents. The term $f_{L,R}(E,T)$ gives the Fermi distribution in the leads. L and R denote the left and the right reservoirs of the microstructure. The factor $t(E,T)$ is the energy dependent transmission function, which characterizes the microstructure. It has to be evaluated separately by considering the scattering properties of the actual device.[2] In the linear response approximation, where eV and ΔT are small perturbations of the chemical potential and temperature of the reservoirs, respectively, the Fermi distribution in the reservoirs can be approximated by

$$f(E - eV, T + \Delta T) \simeq f_0 + \left(-\frac{df_0}{dE}\right)[eV + (E - \mu)\Delta T/T] \tag{2.20}$$

and the transport coefficients can be evaluated using the following expressions:

$$L_{11} = \frac{e^2}{h} \int_{-\infty}^{\infty} dE\, t(E) \left(-\frac{df_0}{dE}\right), \tag{2.21}$$

$$L_{12} = -\frac{e}{hT} \int_{-\infty}^{\infty} dE(E - \mu)t(E) \left(-\frac{df_0}{dE}\right), \tag{2.22}$$

$$L_{21} = -\frac{e}{h} \int_{-\infty}^{\infty} dE(E - \mu)t(E) \left(-\frac{df_0}{dE}\right), \tag{2.23}$$

$$L_{22} = -\frac{1}{Th} \int_{-\infty}^{\infty} dE(E - \mu)^2 t(E) \left(-\frac{df_0}{dE}\right). \tag{2.24}$$

By applying the first Kelvin relation [Eq. (2.12)], or by combining Eqs. (2.15) and (2.22), the thermopower is found to be proportional to the average energy $\langle E \rangle$ of the charge carriers during transport:

$$S \propto -\langle E \rangle / eT. \tag{2.25}$$

---

[2]Since spin effects can also influence the scattering in the microstructure the spin degeneracy is included in $t(E,T)$.

The product $(E - \mu) \left(-\frac{df_0}{dE}\right)$ is an odd function of energy; therefore large L_{12}, i.e. strong thermoelectric effects, can only be expected if $t(E)$ is asymmetric with respect to the chemical potential in the reservoirs.

Note: this treatment assumes that the heat flux $\mathbf{J_Q}$ is due to the kinetic energy of the charge carriers with respect to the Fermi energy in the reservoirs. Additional contributions to the heat flux, e.g. due to changes in the chemical potential, are neglected, which is a good approximation in many cases. However, it should be noted that in systems, where the kinetic contribution to the thermal transport is very small, additional terms may dominate the heat transport [see discussion at the end of Chap. 6].

2.1.3   Remark on Mott's law

Within the semiclassical treatment of the electron gas in metallic systems, a close connection exists between the thermopower and the energy dependent conductance (conductivity). The thermopower can be expressed in terms of the energy dependent conductivity at the Fermi energy [Zim63]

$$S_M = -\frac{\pi^2}{3}\frac{k_B^2 T}{e} \left.\frac{\partial \ln[\sigma(E)]}{\partial E}\right|_{E=E_F} . \tag{2.26}$$

The so called Mott-formula is derived by the Sommerfeld expansion, taking into consideration only the first order in $k_B T$. Furthermore, it is assumed that the particles do not interact and the conductivity varies slowly as a function of the energy in the close vicinity of the Fermi energy. Thus, it is a good approximation as far as the product $t(E)[-\partial f/\partial E]$ is sufficiently large near the Fermi energy.

The Mott formula can be applied to the physics of microstructures by replacing the conductivity by the conductance. Studies of the applicability of the Mott formula to microstructures, such as quantum point contacts, show that the Mott formula gives qualitatively good results as long as the above mentioned conditions are satisfied [LF05]. However, particle interactions and quantum confinement can lead to sharp peaks and a strongly varying density of states far from the Fermi energy. For example, in a Coulomb blockaded QD, the characteristic energy scale associated with the charge transport is not given by the temperature scale but by the charging energy and the level spacing. The density of states near the Fermi energy is zero and shows a sudden step once the Coulomb energy gap is overcome.

2.2   Thermoelectric transport in the Coulomb-blockade

From the general discussion of thermoelectric effects we will now turn to the thermoelectric effects of QDs. Equations (2.21- 2.24) of the previous section indicate that strong thermoelectric effects can be expected, if the transmission function $t(E)$ describing the scattering exhibits a very strong asymmetry with respect to the electrochemical potential

in the reservoirs. Due to the discrete energy spectra in quantum structures, a highly nonlinear transport behavior and thus strong thermoelectric signals are expected.

For the characterization of QDs, the thermopower can be regarded as a different "spectroscopic" tool besides the linear conductance. The variation of the QD potential by means of a gate voltage measures the addition spectrum in a linear conductance experiment. This means, it measures differences in ground state energies with increasing number N of electrons on the QD. The thermopower contains information about the average energy of the charges during the transport. It gives information about the excitation spectrum, i.e. the energy differences at constant N, and thus can be compared to the measurement of the nonlinear conductance and nonlinear differential conductance. However, the fundamental difference is that the thermopower oscillations are a linear response phenomenon, which involves only a small perturbation of the QD system from equilibrium.

2.2.1 Sequential tunneling

In 1992, Beenakker and Staring [Ref. [BS92]] presented results of a linear-response theory for the thermopower of a QD. The Coulomb repulsion was treated within the framework of the "orthodox model" (CI-model) of single electron tunneling [AL91, Bee91]. A possible dependence of the tunneling rates on the number of electrons on the QD was ignored, and the energy level spacing and $k_B T$ were taken much larger than the coupling of the QD states to the leads $h(\Gamma_l + \Gamma_r) \ll k_B T, \delta E$. These assumptions facilitate the characterization of the QD by a set of occupation numbers, one for each energy level. The transport through the dot can then be described by the tunneling rate equations of the transport of electrons from the reservoirs to the QD and vice versa. The result of the stationary solution of the kinetic equation is presented in Chap. 4, where the sequential tunneling theory is used to fit the experimental curves. Here, a descriptive explanation is given for the interpretation of the measured thermovoltage $V_{\mathrm{T}} = -S\Delta T$. It considers only ground state transitions in the QD. In the first order transport, the excited states do not modify the presented concept considerably and simply lead to an additional fine structure on top of the measurement curves; these are discussed in more detail at the end of Chap. 5.

As depicted in Fig. 2.1 for a thermopower measurement, one reservoir has a higher temperature and therefore more occupied states above (a) or more empty states below (b) the Fermi energy E_F than the second reservoir. At low temperatures ($k_B T \ll E_C$), the thermally activated transport takes place mostly through the minimum energy gap between E_F and the QD states. When the electrochemical potential of the QD [here $\bar{\mu}(N + 1)$] has an energy slightly higher than the Fermi level E_F of the reservoirs, the dominating first order transport process is the transport of electrons from the hot reservoir via $\bar{\mu}(N + 1)$ to the cold reservoir [Fig. 2.1(a)].[3] In the thermopower measurement setup,

---

[3]The dominating transport process is the one, which is most probable before the dynamic equilibrium is established.
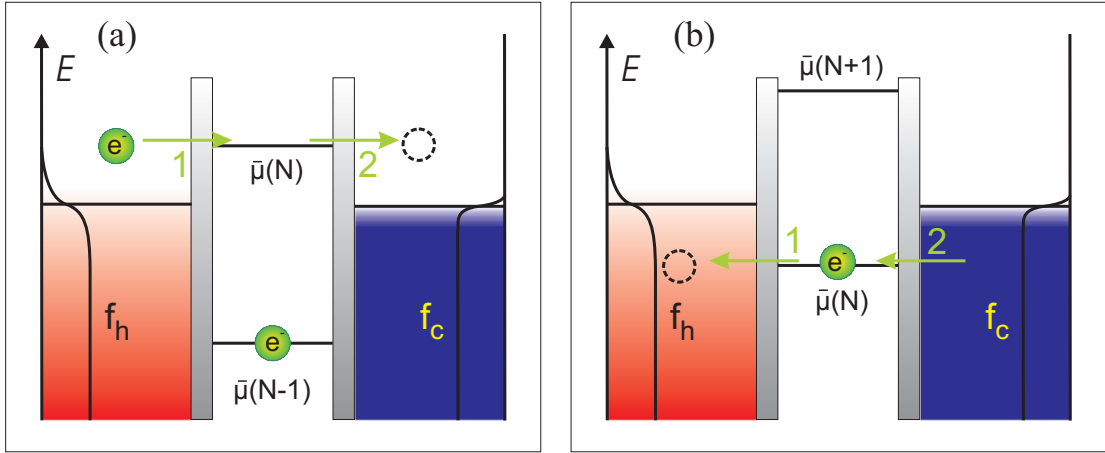
Fig. 2.1: Schematic energy diagram of positive (a) and negative (b) thermovoltage contributions due to sequential (thermally activated) transport. Positive thermovoltage contributions result from the transport of electrons from the hot reservoir to the cold reservoir. The negative thermovoltage contributions correspond to the transport of electrons from the cold reservoir to the hot reservoir. The latter process can also be described as a hole-like transport process, where an empty state (hole excitation) moves from the hot reservoir to the cold reservoir.

the transferred electrons cannot discharge through the electrical connections back to the hot reservoir. Thus an increase in the electrochemical potential of the cold reservoir results, until the transport processes in the reversed direction are of equal strength and the net current flow through the QD is zero. Since the sign of the thermopower (in this case negative) is determined by electrons from above the Fermi level, the transport is described to be electron-like, which is in accordance with the thermopower of n-doped semiconductors and most metals. The average energy $\langle E \rangle$ of the charges moving from the hot reservoir to the cold reservoir is positive with respect to E_F. Figure 2.1(b) illustrates the situation where the electrochemical potential of the QD [here $\bar{\mu}(N+1)$] has an energy slightly lower than the Fermi level E_F of the reservoirs. The dominating transport process can be described by a sequence where first an electron leaves the QD to the hot reservoir, followed by an electron from the cold reservoir entering the QD and reestablishing the initial number of electrons on the dot. The resulting difference in the electrochemical potentials of the reservoirs, as well as the average energy, are of opposite signs (negative) compared to the situation in Fig. 2.1(a). Obviously, the process, which is depicted in Fig. 2.1(b), can also be described by considering a hole that moves from the hot reservoir to the cold reservoir. The charge transport then corresponds to p-doped semiconductors and is said to be a hole-like process.

In general, the thermopower is a result of the competition between the electron- and hole-like transport processes, which have the same strength once the dynamic equilibrium has been reached, i.e. $I_{QD} = 0$. Two situations, where the thermopower contributions from electron and hole like processes exactly cancel each other, are depicted in Fig. 2.2.
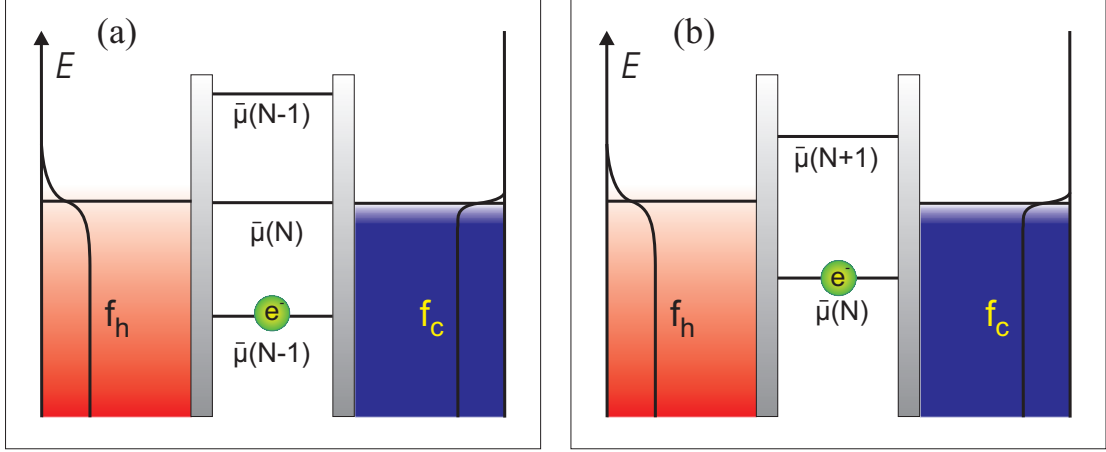
Fig. 2.2: Schematic energy diagram of a QD adjustment that leads to a zero thermovoltage signal amplitude. (a) The electrochemical potential of the QD is aligned with the chemical potentials of both reservoirs. (b) The electrochemical potentials of both reservoirs are aligned in the middle of the effective energy gap.

Here, either the electrochemical potential of the QD is in resonance with the Fermi energy in the leads [Fig. 2.2(a)], or the electrochemical potential from below E_F and above E_F have the same energetic distance to the Fermi energy [Fig. 2.2(a)]. In the latter case, a small shift in the QD potential leads to either dominating electron-like or to hole-like processes via a maximum energy gap. In the limit $T \to 0$, the energy gap determines the average energy which is then given by $\langle E \rangle = \pm \Delta E_C / 2$. Using the Kelvin relation, this yields a maximum thermopower of $S_{extremal} = -\langle E \rangle / eT = \pm E_C / 2eT$.

2.2.2 Cotunneling

In addition to first order tunneling processes, higher order transport processes are expected to take place for the gate voltage range between two single electron tunneling (SET) conductance peaks. The transport mechanism is the same as shown in Chap. 1, Fig. 1.3. However, since the electrochemical potentials of source and drain are in equilibrium, the additional energy that is needed for inelastic cotunneling processes to occur has to be provided by the thermal excitation in the reservoirs [see Fig. 2.3]. The thermoelectric signature of these cotunneling processes (inelastic as well as elastic) in few-electron QD is part of the investigations presented in this thesis.
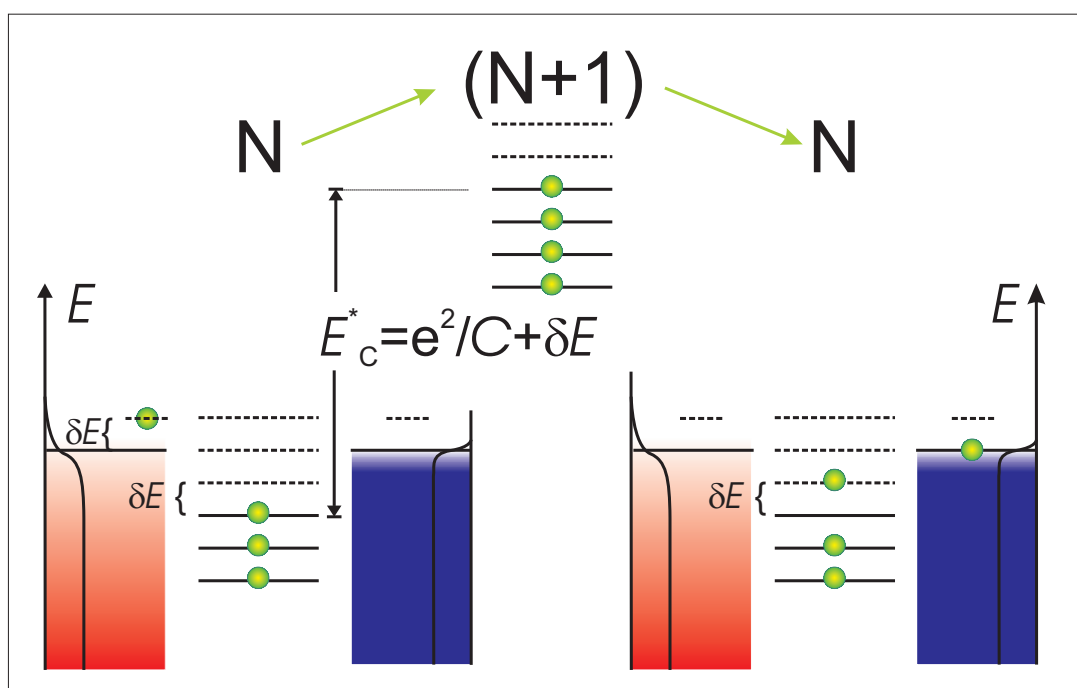
Fig. 2.3: Schematic energy diagram of a cotunneling process (inelastic) in the presence of a temperature difference across the QD. The necessary activation energy is provided by thermally excited electrons in the leads.

Chapter 3

Experimental setup

For the electric and thermoelectric characterization of QD structures special experimental techniques are needed. These are summarized in this chapter in three parts and they are also discussed with respect to their limitations. In the first part, the design of the QD sample is presented, focusing on the material system and the actual QD structure. In the second part, a general overview is given about the experimental techniques which are used for electric and thermoelectric characterization. The third section deals with the current heating technique, which is used for the thermoelectric characterization.

3.1   Quantum dot sample design

3.1.1   Material properties

The few-electron QD structures studied are based on lithographically patterned high electron mobility heterostructures that contain a two dimensional electron gas (2DEG). The GaAs/(Al,Ga)As heterostructures have been grown using molecular beam epitaxy (MBE) by external groups.[1] The results presented in this thesis use 2DEG wafers grown in the group of Dr. D. Reuter and Prof. A.D. Wieck from the Ruhr-Universität Bochum. Ohmic contacts, optical and electron-beam lithography have been done mainly by Dipl. Phys. Markus König and Dr. Tanja Borzenko at the clean-room facilities of the Experimentelle Physik 3 at the Physikalisches Institut der Universität Würzburg.

Figure 3.1 shows the layer sequence of a typical heterostructure with the corresponding valence and conduction band energy diagram. A discontinuity in the potential of the valence band develops at the interface between the GaAs buffer layer and the $Al_{0.33}Ga_{0.67}As$ spacer layer due to the band gap difference of GaAs (1.52 eV) and $Al_{0.33}Ga_{0.67}As$ ($\sim$ 1.67eV).[2] Electrons from the donor layer accumulate in the resulting triangular quantum

---

[1] The 2DEG wafers have been provided by the groups of Prof. W. Wegscheider (Institut für Angewandte und Experimentelle Physik II, Universität Regensburg), Prof. A.D. Wieck (Lehrstuhl für Angewandte Festkörper Physik, Ruhr-Universität Bochum).

[2] The band gap of $Al_xGa_{1-x}As$ ranges from 1.52 eV for $x = 0$ to 2.16 eV for $x = 1$.
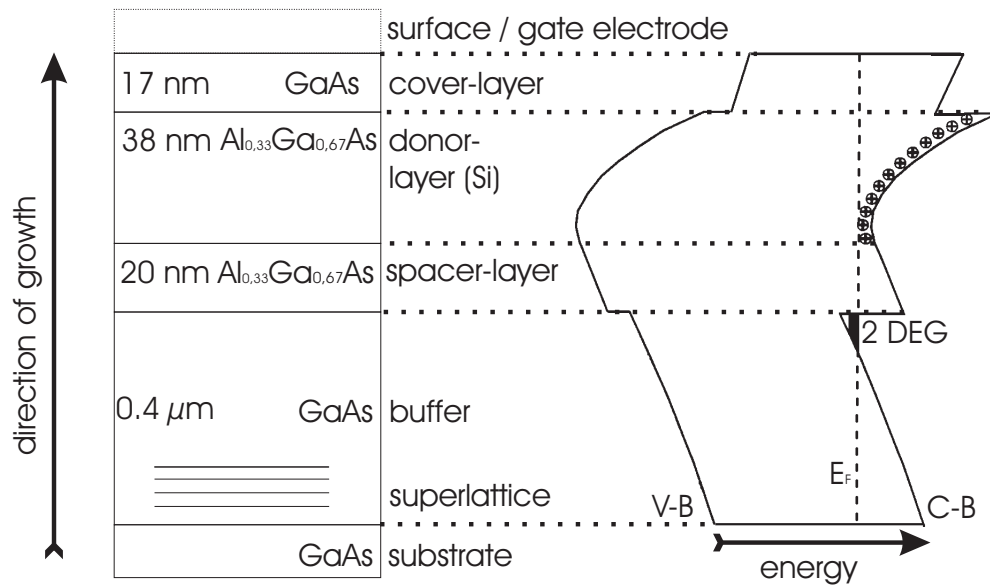
Fig. 3.1: Schematic diagram of an (Al,Ga)As heterostructure similar to the ones used for the experiments. The corresponding schematic band diagram of valence and conduction band (V-B, C-B) is shown on the right. The encircled crosses represent the ionized donor lattice sites. The layer thicknesses given in the graph may vary slightly from sample to sample. Here, a homogeneous doping throughout the donor layer is shown; alternatively, delta doping can be chosen, where just a single layer of Si is placed between the spacer layer and the AlGaAs-layer.

well and form a 2DEG. For electron densities $n_e \lesssim 5 \times 10^{15}$ m^{-2}, only the lowest sub-band (transversal mode in growth direction) of the quantum well is occupied. In the examined samples, the 2DEG is located 75-80 nm below the surface. Electrical contact to the 2DEG is achieved by alloying standard NiAuGe ohmic contacts.

Due to the high purity of the materials used, the very low interface roughness,[3] and the spacial distance of ionized donors and electrons in the quantum well, the lattice defect and impurity-scattering rates are very low for the electrons in the 2DEG. Consequently, very high mean free paths can be achieved for electrons. The samples investigated had a nominal mobility of the order of 10^6 cm^2/Vs at 4.2 K prior to processing. This corresponds to elastic mean free paths $l_e \geq 100$ μm. A detailed table containing the layer sequence and some material parameters of the heterostructures is given in Appendix A.

The basic parameters for electrons in the 2DEG are given here for the ease of reference: The effective mass m^* of the electrons in the 2DEG for GaAs is equal to $0.067 m_0$, where m_0 denotes the free electron mass. A typical electron density of $n_e = 3 \times 10^{11}$ cm^{-2} yields a Fermi-energy of $E_F = n_e / D_{2D}(E) = n_e \pi \hbar^2 / m^* = 10.7$ meV, and a Fermi wavelength of $\lambda = \sqrt{2\pi / n_e} = 46$ nm.

3.1.2   Split gate quantum dot structure

In order to locally control the density of electrons in the 2DEG, metallic (Ti/Au) electrodes (gates) are placed on top of the heterostructure. The isolation to the 2DEG is provided automatically by the metal-semiconductor Schottky barrier. By tuning the bias voltages applied to the individual surface electrodes, the shape of the confining potential in the 2DEG can be modified reversibly. By means of optical and electron-beam lithography, the shape of the Ti/Au-electrodes can be patterned on length scales of just a few 10 nm. This allows devices with dimensions of the order of the Fermi wave length to be fabricated, so that the transport properties are determined by quantum size effects [TPA$^+$86].

Figure 3.2 shows a scanning electron micrograph (SEM) of the central part of the gate structure. Gates R$_1$ and R$_2$, form a quantum point contact (QPC), which serves together with gates T and S$_2$ as the boundaries of an electron heating channel. The functionality of the heating channel will be explained in more detail in Sec. 3.3 of this chapter. Gates T, S$_1$, S$_2$ and P form the QD with a nominal diameter of approximately 250 nm. The surface electrode layout of the gate electrodes is similar to the QD gate structures used in previous QD experiments, where it has been shown that the design allows great flexibility in the number of electrons on the dot to be achieved [CSH$^+$00]. In principle, the number of electrons on the QD can be successively increased, starting from 0 up to above 50, by changing the plunger gate voltage V_P. However, at the same time, the voltages applied to gates T, S$_1$ and S$_2$, which form the tunneling barriers, have to be varied separately in

---

[3]The lattice constants a of GaAs and AlAs are $a_{\text{GaAs}} = 0.56325$ nm and $a_{\text{AlAs}} = 0.566139$ nm. Thus, the lattice mismatch between GaAs- and AlGaAs-layers is smaller than 1%.
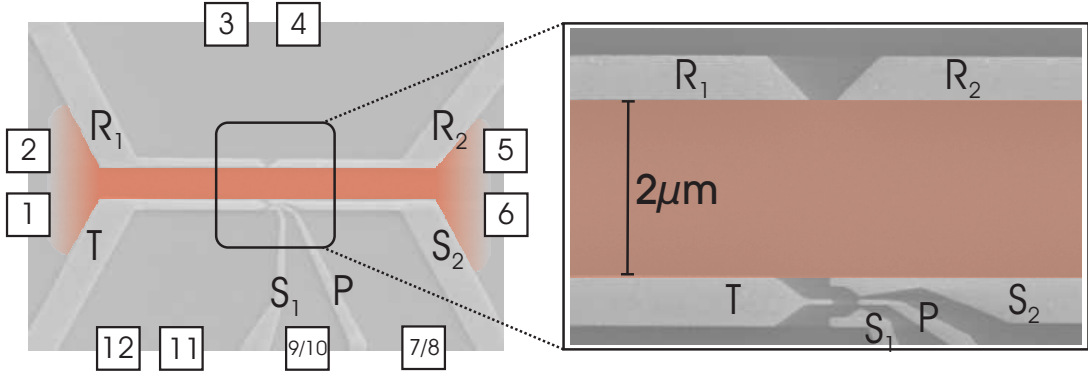
Fig. 3.2: Scanning electron microscope image of the central part of the sample structure. Schottky gates shown by light gray stripes are labeled R_1, R_2, T, P, S_1 and S_2. Ohmic contacts which are schematically indicated by enumerated squares serve as current and voltage contacts via the corresponding sample areas marked in dark gray. The red shaded sample areas mark the electron heating channel.

order to maintain a constant coupling of the QD to the two contacting reservoirs. For the present experiments, the barriers are adjusted in a way that the number of electrons can be varied conveniently, i.e. by changing only the voltage V_P applied to the plunger gate P.[4]

The electrostatic confinement potential can be calculated following an approach of [DLS95, LS94]. The height of the total electrostatic confining potential $\Phi(r)$ is given by the superposition of the confining potentials of the individual gates i:

$$\Phi(R) = \frac{1}{2\pi} \sum_i V_i \tilde{I}_i(r, z), \tag{3.1}$$

where

$$\tilde{I}_i(r) = \int \int_{S_i} \frac{z \, dr'}{(|r - r'|^2 + z^2)^{2/3}} \tag{3.2}$$

is the surface integral over the area of the gate electrodes.

Figure 3.3 shows the results of the calculations of the QD confining potential for two different plunger gate voltages. At the boundaries of the gate electrodes, a smooth step in the potential is observed, due to the large lateral depletion length (of the order of 100 nm for a step height of 10 meV). For $V_P = 0$ V, the QD is large and the distance between the QD and the reservoirs is small. For $V_P = -2.0$ V, the size of the QD is reduced, and the distance between the QD and the reservoirs has increased.

---

[4]The number of electrons on the QD can be deduced from the magnetic-field evolution of the CB peaks [MFM$^+$91, MFK$^+$92]. In order to use a charge read-out technique, an additional quantum point contact has to be placed in the close vicinity of the QD [EHG$^+$03]. Measurements of comparable single QD structures have shown that it is possible to successively fill up the QD starting from zero electrons [Sch06].
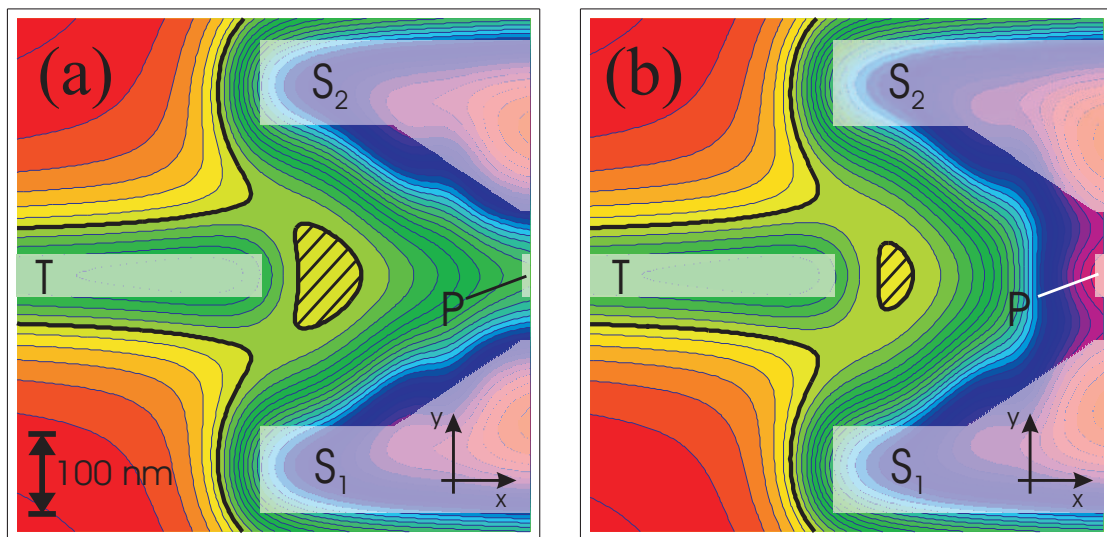
Fig. 3.3: Color-scale plot of the calculated electrostatic confining potential of a single QD structure. Red and blue colors correspond to low and high electrostatic potential, thus to high and low electron density domains, respectively. White shaded areas mark the positions of the surface gate electrodes. The black thick equipotential line is added as a guide to the eye. This line corresponds to the Fermi energy level of the 2DEG. The black hatched area marks the position of the QD. The numerical values of the voltages applied to the tunnel barrier gates are: $V_{\text{top}} = -1.1$ V, $V_{\text{S}_1,\text{S}_2} = -0.75$ V. The plunger gate voltages correspond to (a) $V_{\text{P}} = 0$ V and (b) $V_{\text{P}} = $ -2.0 V.

From the potential landscape, one can infer that the size of the QD in the y-direction depends on the voltage ratio of the voltages applied to the side gates and the top gate. In order to obtain very small QDs, large side gate voltages and small top gate voltages are desirable. The thickness of the tunnel barriers, which determine the coupling of the QD to the reservoirs, crucially depends on the overlap of the side gates and the top gate (in the x-direction). In order to examine the strong coupling regime of the QD to the reservoirs, a maximum nominal overlap of 25 nm has been chosen.

3.2 Measurement setup

3.2.1 General considerations

The material system and the size of the QDs determine the energy scale which has to be considered for the experiments. Typical charging energies of $E_C = 1$ - 3 meV and QD level spacings of the order of $\delta E = 100$ μeV have to be resolved in the transport experiments. Thus, the temperature range of interest is between 10 mK and 1-4 K. This temperature range lies in the operating regime of commercially available dilution cryostat systems. For the experiments, the samples are either mounted inside the mixing chamber of a top loading dilution refrigerator (Oxford Instruments, Model 400 TLM Dilution Refrigerator) or in thermal contact outside the mixing chamber of a bottom loading system (Leiden Cryogenics B.V., Model Minikelvin 126-TOF Dilution Refrigerator). Generally speaking, it is necessary to keep excitation as well as noise signals small compared to the temperature energy scale for the characterization in the linear transport regime. The excitation voltages applied in linear conductance measurements have to be smaller than $k_B T/e = 86.2\mu$V, in order to avoid unwanted sample heating or non-equilibrium situations. Below $T = 100$ mK, signal amplitudes of a few μV have to be detected with a reasonable resolution.[5] Furthermore, the measurement apparatus has to provide a high dynamical range since the sample resistance ranges from a few kΩ to several 100 MΩ.

In order to accomplish all these requirements, low-frequency lock-in techniques are used for the electrical and thermoelectrical transport experiments.

3.2.2 Electrical characterization

Figure 3.4 shows a schematic block diagram of the measurement circuit for the electric characterization. In order to measure the linear conductance, an ac modulated excitation

---

[5]In order to reduce electron heating by radio frequency electrical noise, low-pass RLC- and Π-filters are used in the electrical wiring connected to the device at the top of the cryostat. In the bottom loading system, it is possible to use thermally anchored Thermocoax® cables for the connection between the mixing chamber and the sample. For the Minikelvin 126-TOF dilution refrigerator system, the length of the Thermocoax® cables is approximately 45 cm. A comparison of various low temperature electrical filter techniques can be found in Ref. [BGH+03].
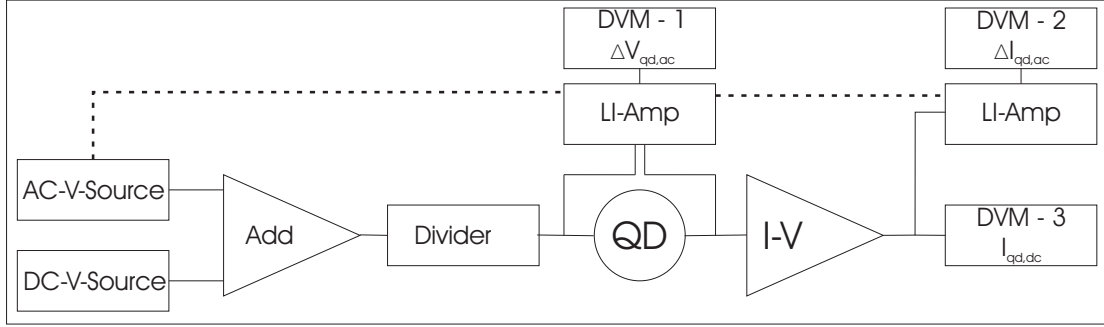
Fig. 3.4: Schematic block diagram of the measurement setup for the electric characterization. Excitation voltages from the ac- and dc voltage sources are added by means of a summing voltage amplifier (Add). The excitation amplitude is reduced by a voltage divider prior to the QD. For most of the measurements, I/V-converter with amplifying factors ranging from 10^6 V/A to 10^8 V/A have been used. ac-voltages are detected by phase sensitive lock-in amplifiers. The effective voltage output of the lock-in amplifiers as well as the dc-voltage component of the I/V-converter output are monitored by digital voltmeters (DVM). The lock-ins are phase synchronized with the ac-voltage source.

voltage $V_{ex,ac} < k_B T/e$ is applied across the QD. The resulting current $I_{QD} = \Delta I_{QD,ac}$ is converted by an Ithaco 1211 current-voltage converter into a voltage signal which is measured by a lock-in amplifier (LI-amp). In order to eliminate the series resistance of the ohmic contacts, a second lock-in amplifier is used to measure the amplitude modulated voltage drop across the QD, where $V_{QD} = \Delta V_{QD,ac}$. The conductance of the QD is $G_{QD} = I_{QD}/V_{QD} = \Delta I_{QD,ac}/\Delta V_{QD,ac}$. The LI-amps are phase locked to the ac-voltage source. The dc output voltage is related to the peak to peak input voltage by $V_{eff,dc} = 1/2\sqrt{2}V_{inp,pp}$. The (effective) dc voltages are measured by digital voltmeters (DVM) which are connected to the computer via an optical fiber. Prior to the signal processing in the mixer stage of the LI-amp, the voltage signal is amplified either by an external (differential) amplifier or the internal amplifier stage of the lock-in. Using an external preamplifier turns out to be useful in order to reduce noise coupling into the measurement circuit, since the external preamplifier can be placed close to the sample, keeping the cables at room temperature outside the cryostat as short as possible. Ground loops are prevented by electrically isolating all measurement devices from each other. The electric ground of the cryostat serves as common ground of the measurement circuit and the individual measurement devices. Source-drain bias and gate bias voltages are applied with regard to this fixed potential.

By adding a finite dc drain-source voltage V_{DS} to the ac modulated excitation voltage, where $V_{ex,ac} < k_B T/e$, the nonlinear differential conductance $\frac{dI_{\mathrm{DS}}}{dV_{\mathrm{DS}}}$ can be measured with the same setup. The necessary dc-bias voltage V_{DS} is added to the ac-modulated excitation

voltage by means of a summing amplifier. $\frac{dI_{\text{DS}}}{dV_{\text{DS}}}$ is given by

$$\left.\frac{dI_{\text{DS}}}{dV_{\text{DS}}}\right|_{V_{\text{DS}}\neq 0} \approx \left.\frac{\Delta I_{QD,ac}}{\Delta V_{QD,ac}}\right|_{V_{\text{DS}}\neq 0}. \tag{3.3}$$

This represents the derivative of the finite-bias conductance $G = I_{\text{DS}}/V_{\text{DS}}$ with respect to the applied drain source voltage V_{DS} in the limit of a small $V_{ex,ac}$. $dI_{\text{DS}}/dV_{\text{DS}}$ is interpreted as the convolution of the thermally broadened Fermi distributions of the leads with the transmission function (spectral density) of the QD $t(E)$. The derivative $\frac{dI_{\text{DS}}}{dV_{\text{DS}}}$ will be large if the conductance increases due to an increase in the QD transmission. $\frac{dI_{\text{DS}}}{dV_{\text{DS}}} < 0$ can be observed if the transmission decreases although V_{DS} increases. This scenario occurs if an increasing number of transport channels through the QD leads to destructive interference between the travelling paths of the electrons and thus to a reduced transmission probability. Using this technique, one has to keep in mind that a finite V_{DS} applied across the device (QD) creates a non-equilibrium situation for the QD, and may alter the unperturbed internal properties of the device itself under test.

Referring to Fig. 3.2, gates R_1 and R_2 are grounded for linear and, especially, for finite-bias conductance measurements. This procedure eliminates the finite channel contact resistance, and prevents a significant heating of the electron gas in the heating channel at high source-drain currents, which would lead to thermal smearing and unwanted temperature differences between the QD reservoirs. Since the gates of the reference quantum point contact R_1 and R_2 are in the vicinity of the QD gates, they couple capacitively to the QD. For a direct comparison of conductance and thermopower measurements, where in the latter a constant voltage is applied to R_1 and R_2, the capacitive coupling of the QD and the quantum point contact gates has to be taken into account. The capacitive coupling leads to a linear shift of the QD potential. The capacitive coupling of gates $R_{1,2}$ to the QD is about a factor of 5 smaller than the capacitive coupling of the plunger gate ($C_{\text{P}}/C_{\text{R}_1,\text{R}_2} \approx 0.2$). This slightly modifies the effective height of the tunnel barriers.[6] The measurements presented in this thesis are corrected for this potential shift in order to allow direct comparison of conductance and thermopower measurements to be made.

3.2.3 Thermoelectrical characterization

The basic principle of thermoelectric measurements is explained in the first part of this section, following Ref. [Bar72]. In the second part, the setup for the thermoelectric characterization of the QD sample is presented.

For measuring the potential difference which develops across a device subjected to a temperature gradient (or temperature difference), electrical connections must be made to either end of the device, thus setting up a similar temperature gradient (difference) in the

---

[6]Since both tunnel barriers are located at different distances to the quantum point contact gates, careful readjustment of the barrier height is necessary in order to maintain the same situation as in the case of the undefined reference quantum point contact ($V_{\text{R}_1,\text{R}_2} = 0$ V)
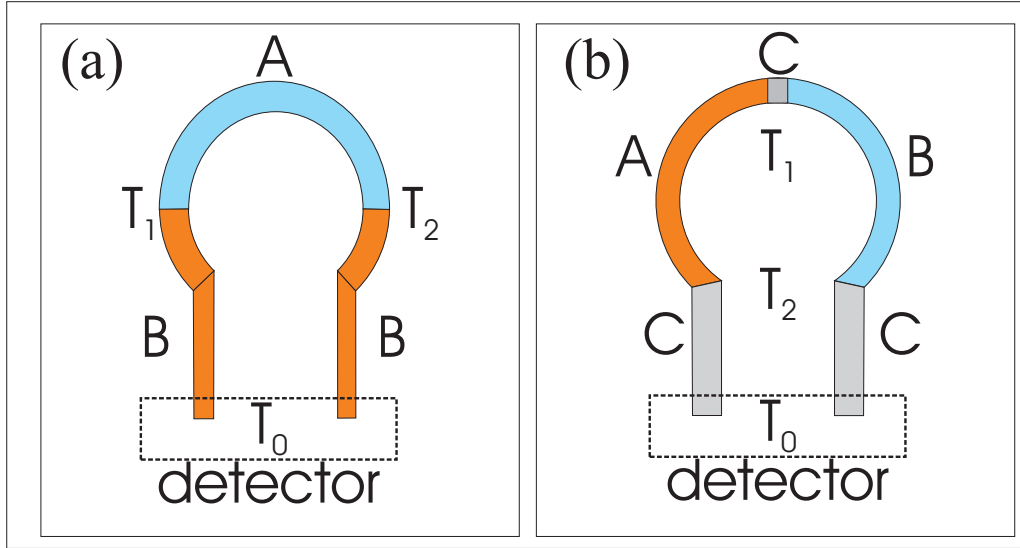
Fig. 3.5: Schematic diagrams of asymmetrical circuits constructed from different components (metals and/or devices) for thermoelectric measurements. (a) Most simple configuration, using only two different components. (b) Configuration used for measuring the thermopower of mesoscopic or QD devices. In both cases, the Seebeck electro motive force, determined solely by the components A and B, is measured by the detector.

complete electrical detecting system. This will contribute its own thermoelectric electro motive force (e.m.f.) to the circuit. If the entire detecting circuit is made of the same material as that under test, a symmetrical circuit will result and no net e.m.f. will be detected. Thus, in order to measure a thermoelectric e.m.f., asymmetrical circuits of at least two different materials must be constructed. This implies that only the differences of the thermoelectric e.m.f. of two different materials can be measured.[7] Figure 3.5 shows two examples of possible electrical circuit configurations, which can be used to determine the thermoelectric e.m.f. created by material or device A with respect to the thermoelectric e.m.f. created by material or device B. The circuit diagram of Fig. 3.5(a) represents the most basic configuration. However, for measuring the thermoelectric properties of the QD sample, this configuration cannot be used due to the following reasons. First, the materials of the sample and the wiring into the cryostat can not be made of the same materials, and second, using an electric current for local heating of the electron gas on a mesoscopic scale helps to avoid the direct connection of the hot reservoir to a voltage probe. In order to circumvent these problems, a third component is inserted in the electric circuit [cf. Fig. 3.5(b)]. In the actual QD sample [see Fig. 3.2], components A and B correspond to the QD and the quantum point contact respectively. The component C, which is at temperature T_2, corresponds to the electron gas in the heating channel formed by gates

---

[7]The absolute thermoelectric power of a material or a device can be measured if the second material is a superconductor, since the thermoelectric e.m.f. of superconductors vanishes.
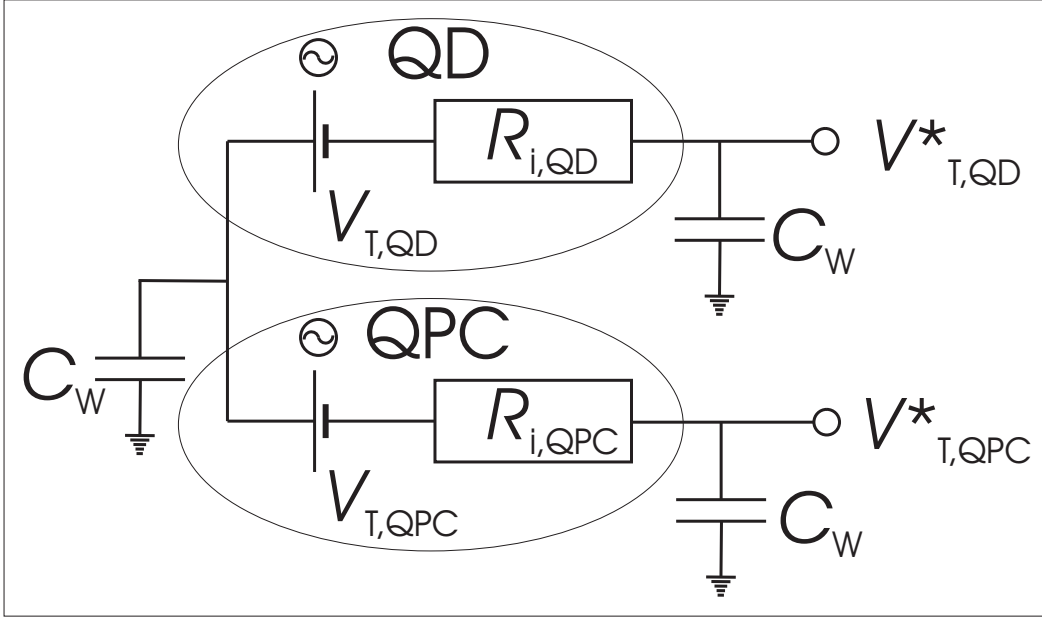
Fig. 3.6: Schematic circuit diagram of the QD-QPC equivalent thermovoltage measurement circuit. QD and QPC act as alternating voltage sources ($V_{T,QD}$ and $V_{T,QPC}$) with internal resistances $R_{i,QD}$ and $R_{i,QPC}$. The wiring from the voltage probes into the cryostat has the capacitance C_W, the heating channel has the capacitance C_C.

R_1, R_2, T and S_1 (red shaded area). The component C, which is at temperature T_1, corresponds to the electron gas of the 2DEG regions connected to ohmic contacts labeled 3, 4, 11 and 12.

By means of an electron heating technique, which is described in more detail in Sec. 3.3 of this chapter, the temperature of the electron gas in the current heating channel (red shaded area in Fig. 3.2) is increased by an amount $\Delta T = T_{e,\text{hot}} - T_{e,2\text{DEG}}$ with respect to the temperature of the surrounding 2DEG areas (dark grey areas of Fig. 3.2). The temperature difference across the QD and the quantum point contact creates two thermovoltages $V_{T,QD}$ and $V_{T,QPC}$. The voltage difference $V_T = V_{T,QD}$-$V_{T,QPC}$ is measured by a differential voltmeter, which is connected to ohmic contacts 3 and 11 (or 4 and 12). V_T contains the thermopower of the QD ($S_{QD} = V_{T,QD}/\Delta T$) as well as that of the QPC$_{R_1R_2}$ ($S_{QPC} = V_{T,QPC}/\Delta T$). For convenience, the thermopower of QPC$_{R_1R_2}$ is adjusted to zero by setting its conductance at the center of a conductance plateau [vHMBF92].

In order to separate the small thermoelectric signal from offset voltages and improve the signal to noise ratio, the temperature difference ΔT is amplitude modulated. This is accomplished by driving an ac-modulated heating current of frequency $\nu = 13$ Hz through the heating channel. The dissipated power is proportional to the temperature increase $V_T \propto \Delta T \propto P = RI^2(\nu)$, and thus the thermovoltage can be detected at twice the frequency [$V_T \propto I_0 \cos^2(\nu t) = I_0(1 - \cos(2\nu t)/2)$].

In the thermopower measurement setup, the QD-QPC-system acts as a voltage source. Like all voltage sources, this system is not ideal, and the internal resistance of the voltage source has to be taken into account. The equivalent circuit diagram of the thermovoltage signal path is sketched in Fig. 3.6. The QD as well as the quantum point contact consists of an ideal voltage source in series with their internal resistances $R_{i,QD}$ and $R_{i,QPC}$, and generate the thermovoltages $V_{T,QD}$ and $V_{T,QPC}$. The voltage signals pass the feed-through capacitances C_W of the wiring into the cryostat. Outside the cryostat, the differential voltmeter detects the difference of the corresponding voltages $V_{T,QD}^*$ and $V_{T,QPC}^*$. This electric circuit shows a low pass filter behavior, where the ratio between the detected signal amplitude and the actual thermovoltage created is given by

$$\frac{|V_T^*|}{|V_T|} = \frac{1}{\sqrt{1+(\omega RC)^2}}. \tag{3.4}$$

The cut-off frequency $2\pi\nu_g = \omega_g = 1/RC$ depends on C_W and $R_{i,QD}$. The internal resistance of the QPC usually is much smaller than the internal resistance of the QD, and $V_{T,QPC}$ is not attenuated. A typical measurement signal modulation frequency of $\nu_g = 26$ Hz and a capacitive load of the order of 5 nF thus yield a -3 dB signal attenuation for internal resistances of 1.22 MOhm ($\hat{=}4.2\times10^{-3}e^2/h$). Additionally, the low pass filter induces a phase shift of the signal with respect to the excitation signal (heating current); this can be measured by phase-sensitive lock-in detection. The magnitude of the phase shift is given by

$$\tan\varphi = \frac{V_{T,y}^*}{V_{T,x}^*} = -\omega RC, \tag{3.5}$$

where $V_{T,x}^*$ and $V_{T,y}^*$ are the x and y-components of the phase dependent signal of the QD thermovoltage. Equations (3.4) and (3.5) can be used to eliminate the low pass filter effect of the measurement circuit, and rescale the thermovoltage data. This method extends the measurement range by one to two orders of magnitude. However, it is limited by the phase stability of the lock-in detection and the signal noise of the (in-phase) x-component of the thermovoltage signal.

Figure 3.7 shows the zero-bias conductance G and the corresponding thermovoltage V_T of a single-electron-tunneling (SET) conductance peak as a function of the plunger gate voltage V_P at a lattice temperature of $T_L = 20$ mK. For comparison, the x- and y-components of the detected thermovoltage signal together with the calculated full magnitude $|V_T^*| = \sqrt{(V_{T,x}^*)^2 + (V_{T,y}^*)^2}$ have been added to the graph. Towards more negative V_P, the height of the tunnel barriers increases, leading to a very low conductance in the Coulomb blockade conductance valley ($G \leq 10^{-4}e^2/h$). At these plunger gate voltages, the attenuation of the thermovoltage signal is strongest and the rescaled thermovoltage shows strong fluctuations due to the high measurement uncertainty. These fluctuations can be reduced by averaging multiple curves. Note that the y-component shows an additional wiggle at the center of the SET conductance peak. This non-monotonous behavior
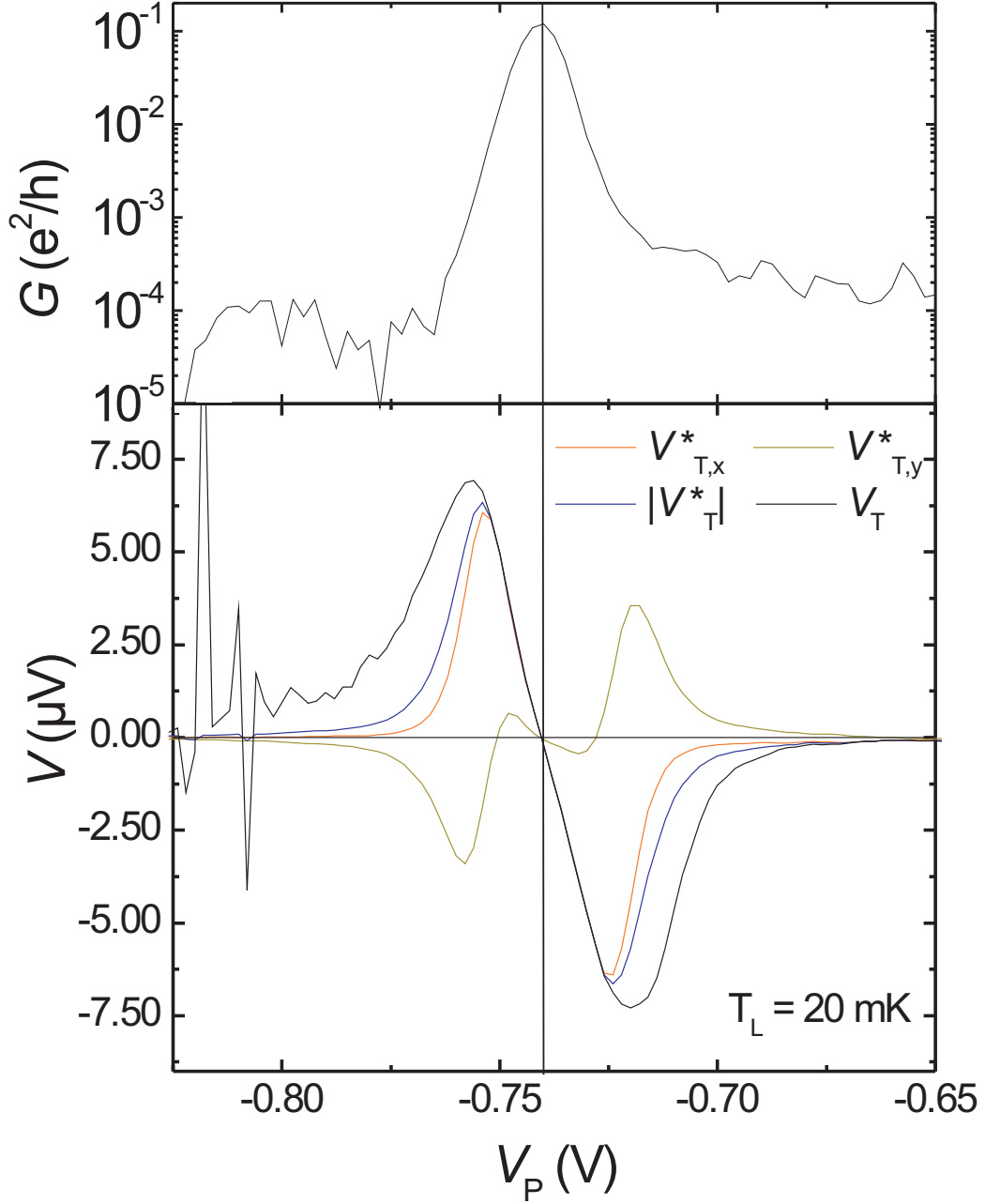
Fig. 3.7: Zero-bias conductance G (upper panel) and corresponding thermovoltage (lower panel) of a single electron tunneling conductance peak both at $T_L = 20$ mK. The solid vertical line indicates the position of the conductance peak. The lower panel shows the x- and y-components of the detected thermovoltage signal (orange and dark yellow line, respectively) together with the calculated full magnitude $|V_T^*| = \sqrt{(V_{T,x}^*)^2 + (V_{T,y}^*)^2}$ (blue line), and the rescaled actual thermovoltage created by the QD V_T (black line).

results from the fact that the phase adjustment of the lock-in amplifier has to be done a little away from the center of the SET conductance peak at finite signal amplitude.

The low pass filter effect results from the low temperature measurement setup. Attempts to reduce this effect by choosing lower modulation frequencies resulted in an increased noise level, mostly due to $1/f$ noise. Thus, a compromise has to be made between the necessary filtering and the QD impedance (coupling of the QD to the leads) in order to obtain a reasonably low temperature of the electron gas and the capability to measure the thermovoltage of a very high impedance source, respectively. The thermopower measurement data shown throughout this thesis has taken into account this limiting low-pass effect.

3.3 Current-heating technique

3.3.1 Basic principle

Experimentally, the main problem in performing thermopower measurements on nanostructures is how to obtain a sizable temperature difference across a very small device. Here, a current heating technique is used [GHL$^+$90], that previously has been successfully applied to measure the diffusion thermoelectric properties of quantum point contacts [MvHB$^+$90, MGvH$^+$92, ANS$^+$98, ANS$^+$98], and metallic QDs [SMA$^+$93, MBGM98].

This technique is based on the fact that the coupling between electrons in the 2DEG and phonons (lattice) is significantly reduced at low temperatures. For $T < 1$ K, heated electrons relax to the lattice temperature over a distance of several 100 μm [MWK$^+$96]. For bias voltages exceeding $k_B T$, and device sizes smaller than the electron-phonon scattering length l_{e-ph}, the distribution of the electrons is not necessarily in equilibrium with the surrounding lattice, since the thermalization due to electron-phonon scattering is strongly reduced. As a result, the temperature of the electrons can vary locally, and differs from the temperature of the lattice at very low temperatures. The local electron temperature depends on the dissipated power, the device geometry as well as on the interaction of the electrons with phonons, local lattice defects and other electrons.

In particular, the local heating of just one QD reservoir is accomplished by electrostatically defining a two dimensional wire next to the QD through which an electric heating current is driven. Figure 3.2 shows a SEM micrograph of the gate structure, where gates R_1, R_2 define, together with gates T and S_1, the electron heating channel. The length l_C and width w_C of the heating channel are $l_C = 20$ μm and $w_C = 2$ μm, respectively. Energy dissipation in the channel results in the local heating of the electron gas.

Due to the small electron-phonon coupling in (Al,Ga)As 2DEGs at low temperatures ($l_{e-ph} \gg l_C$), hot electrons can only dissipate their excess energy to the lattice in the wide 2DEG area behind the channel exit, while rapid electron-electron scattering leads to thermalization of the electrons in the channel to a temperature $T_{e,\text{ch}}$ which is higher than the lattice temperature (T_L ($l_{e-e} < l_C$). Hence, the QD is embedded between the hot electron reservoir in the channel (with electron temperature $T_h = T_{e,\text{ch}}$) and the cold surrounding 2DEG ($T_h > T_{2\text{DEG}} \geq T_L$). The constant temperature difference $\Delta T = T_{e,\text{ch}} - T_{2\text{DEG}}$ across the QD can be adjusted via the current through the channel.

Note that by using this electron heating technique, the 2DEG is heated directly, without raising the lattice temperature T_L. Thus, the phonon drag contribution to the thermopower can be neglected and only the contribution of electron diffusion is detected [ANS+98, CB86].

3.3.2 Temperature calibration

While the temperature of the electron gas $T_{2\text{DEG}}$ can be determined by fitting the temperature dependent line shape of the SET conductance peaks, an additional method is needed that reliably determines the increase of the temperature in the current heating channel as a function of the applied heating current.

Fitting the thermovoltage measurement curves with the available theoretical models for thermopower oscillations in the Coulomb blockade regime represents one possibility to obtain a value for the applied temperature difference. However, this method depends on the validity and applicability of the used theoretical models. In previous studies of the thermoelectric power of nanostructures, various methods have been used to *independently* determine the temperature increase of the 2DEG due to an applied heating current. Most techniques have employed the visibility of features in the electrical transport; among these are Shubnikov-de Haas (SdH) oscillations [MFZ+91, MAE+87, LNHF89, BimcVC95], the zero magnetic field resistance and weak localization corrections [WYGB86, MWK+96]. Additionally, the quantized conductance of 1-dimensional wires [ANS+98] can be utilized. In the following, the techniques mentioned will be discussed shortly with respect to their applicability to the given sample structure.

3.3.2.1 Quantum point contact

As pointed out in the previous section [Sec. 3.2.3], the thermopower of a device can only be determined in comparison with a reference material or device. For the given sample structure, the quantum point contact located at the opposite side of the heating channel is used for this purpose. The electric and thermoelectric properties of QPCs are well understood [vWvHB+88, WvHB+88, MvHB+90, vHMBF92], allowing a comparison of the experimental thermovoltage of the QPC with theory to be made. Thus, it seems reasonable to employ the known behavior of the QPC as a thermometer for the 2DEG itself, as has been done in Ref. [ANS+98].

For the measurement of the thermovoltage of QPC_{R_1,R_2}, only the gates of the current heating channel are defined, leaving V_{S_2} and V_{top} at a constant voltage, while V_{S_1} and V_P are kept at zero voltage. The heating current is applied between contacts 1 and 5, and the created thermovoltage is detected at contacts 3 and 11. As the gate voltages V_{R_1} and V_{R_2} are made more negative, the QPC_{R_1,R_2} constriction is narrowed, and the conductance drops in steps of $2e^2/h$ each time the number of subbands i is reduced. As the conductance $G_{QPC_{R_1,R_2}}$ falls, a peak is observed in the thermovoltage $V_{\mathrm{T,QPC}_{R_1,R_2}}$.[8] The peak height can be used to determine the electron temperature of the hot electrons in the heating channel. The maxima are given by [Str89, MvHB$^+$90, vHMBF92]

$$S = -\frac{k_B}{e}\frac{\ln 2}{i - 1/2}, \tag{3.6}$$

where a step-function model has been assumed for the transmission function $t(E)$ of the quantum point contact. A more realistic model accounts for the rounding of the steps in $t(E)$ by modelling the electrostatic confining potential by a saddle-shaped function. This yields a value of $S \approx -20~\mu\mathrm{VK}^{-1}$ for the thermovoltage peak near $G = 1.5~(2e^2/h)$ instead of $S = -40~\mu\mathrm{VK}^{-1}$ predicted by the pure step-function model.

The prerequisite for this calibration procedure is a well defined behavior of the QPC, i.e. the existence of well defined conductance plateaus. Unfortunately, the samples investigated, show a strongly oscillating behavior of the QPC resistance as a function of the gate voltage [cf. Fig. 3.8(a)], especially at very low (millikelvin) temperatures. Correspondingly, the thermovoltage also oscillates instead of showing a pronounced peak like structure [cf. Fig. 3.8(b)]. This behavior results from potential fluctuations in the 2DEG in the close vicinity of the QPC [KBM00] and the reflection of ballistic electrons at the opposite boundary of the current heating channel. In order to calculate the expected QPC thermopower, a detailed knowledge of the QPC confining potential or the energy dependent transmission function $t(E)$ would be desirable, and a more sophisticated treatment would possibly be necessary. Furthermore, additional many body effects, as the so called 0.7 anomaly, would have to be incorporated [ANP$^+$00, TM06]. Although the mentioned uncertainties limit the accuracy of this temperature calibration technique, it is a reasonably reliable method. Even in the case of very strong QPC fluctuations, as it is shown in Fig.3.8, the method has proved useful for estimating the order of magnitude of the temperature increase due to the current heating. Assuming the oscillation amplitude at $V_{S_1} = 1.0$ V to correspond to a thermopower of -20 μV/K yields a temperature difference of $\Delta T \simeq 10$ mK for $I_H = 4.2$ nA.

It is noteworthy that the single particle thermopower line shape, that is calculated by using the Mott-formula [Eq. (2.26)], often yields qualitatively good agreement with the measured thermovoltage curve. However, especially in the presence of strong conductance fluctuations, the calculated Mott thermopower shows poor agreement with the measured

---

[8]Alternatively, the same procedure can be applied to measure the thermovoltage of $\mathrm{QPC}_{S_2,T}$.
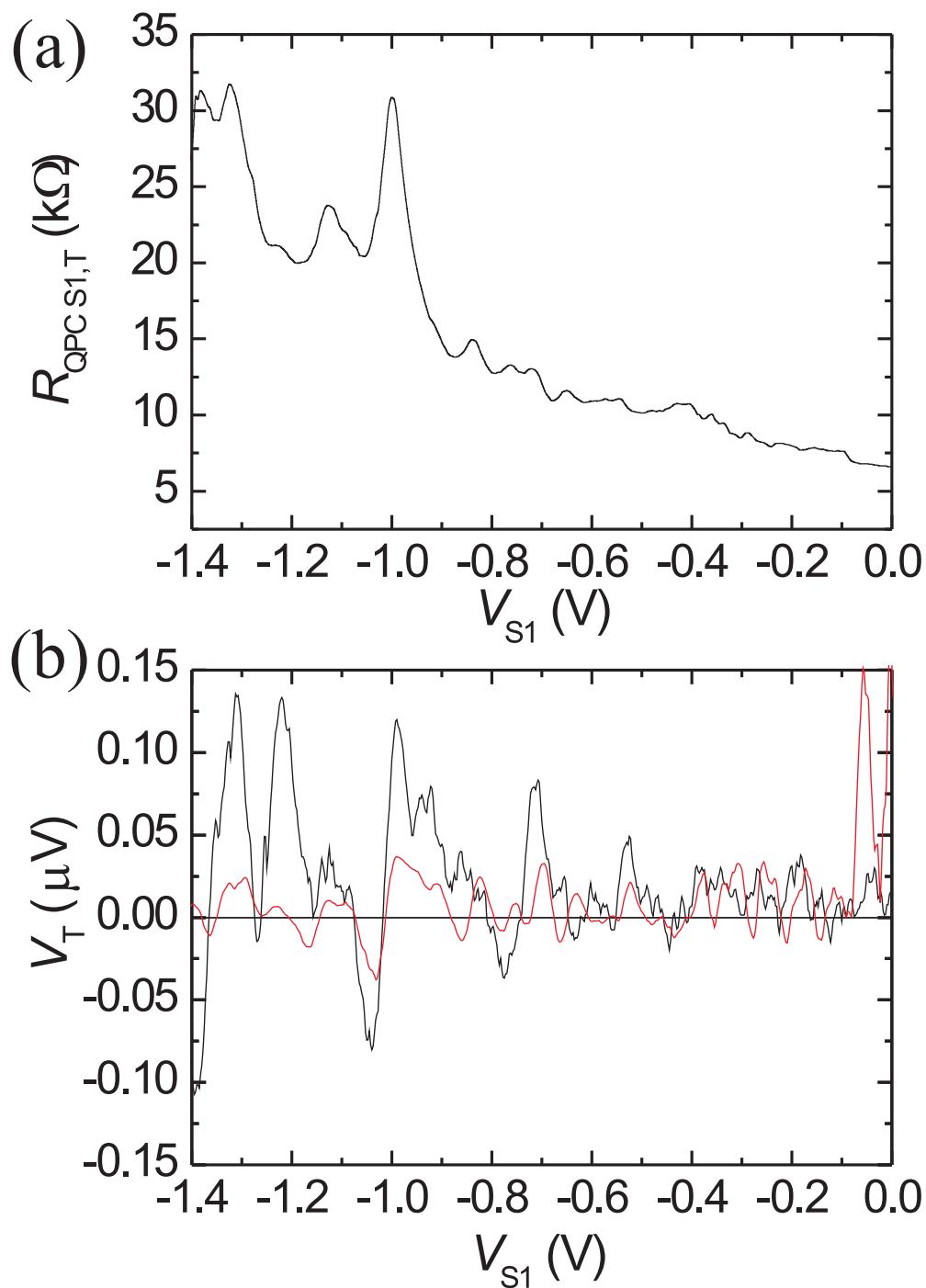
Fig. 3.8: (a) Resistance of $QPC_{S_1,T}$ with gates R_1 and R_2 defined and $V_{top} = 0.76$ V. (b) Corresponding thermovoltage (black line) and calculated Mott-thermopower (orange line, arbitrary scale).

QPC thermopower [cf. Fig. 3.8(b)]. In any case, care has to be taken for fitting the temperature difference, since the numerical pre-factor of S_{Mott} is only valid if the temperature represents the smallest energy scale in the system [LF05].

3.3.2.2 SdH-Oscillations

The amplitude of Shubnikov-de Haas (SdH) oscillations in the longitudinal resistance R_{xx} of the heating channel are temperature as well as heating current dependent. The comparison of $R_{xx}(T)$ with $R_{xx}(I_H)$, allows a calibration for the temperature of the electron gas in the heating channel $T_C(I_H)$ to be obtained.

Following factors have to be considered when this method is applied: These measurements have to be done in strong magnetic fields perpendicular to the 2DEG in the quantum Hall regime. At high fields, the scattering of the electrons is modified, because the electrons are forced on circular trajectories. The wave functions are those appropriate to Landau levels, and the momentum transfer in the plane is restricted to $\hbar/l_c$, where $l_c = m^* v_F/eB$ is the cyclotron length [MSKH94]. Additionally, on a quantum Hall plateau the dissipation of the injected heat takes place at so called "hot spots" close to the ohmic contacts of the samples, where the current is injected [RDC98]. Since the heat transport and the scattering also crucially depend on the spacial extension of compressible or incompressible regions at the center of the 2DEG, a variation of ΔT as a function of the applied magnetic field can be expected. A careful analysis of this method has to consider how the temperature increase determined at high magnetic fields can be extrapolated to the low magnetic field range. So far, it has been shown that different thermometry techniques yield different temperatures under the same heating conditions [ANS+98].

Due to these inherent problems, this method has not been chosen for determining the temperature difference created by the heating current at small magnetic fields. In Chap. 6, it is shown that indeed a strong variation of the thermovoltage signal amplitude as a function of the magnetic field can be observed. Hence, the present work leaves the quantitative investigation of the thermopower of QDs in the quantum Hall regime as a future perspective.

3.3.2.3 Analysis of the heating channel resistance

The local electron temperature in the heating channel does not only affect the transport through the QD and the quantum point contact, but also the scattering of the electrons in the heating channel itself. Thus, the measurement of the temperature and heating current dependent resistance of the heating channel provides a method for the temperature calibration at zero and low magnetic fields perpendicular to the plane of the 2DEG.

Figure 3.9, shows the magneto-resistance of the heating channel R_C for various lattice temperatures T_L and heating currents I_H. In this measurement, the magnetic field is applied parallel to the 2DEG. The resistance curves show a fluctuating R_C as a function of the applied magnetic field, which is nearly symmetric with respect to the zero
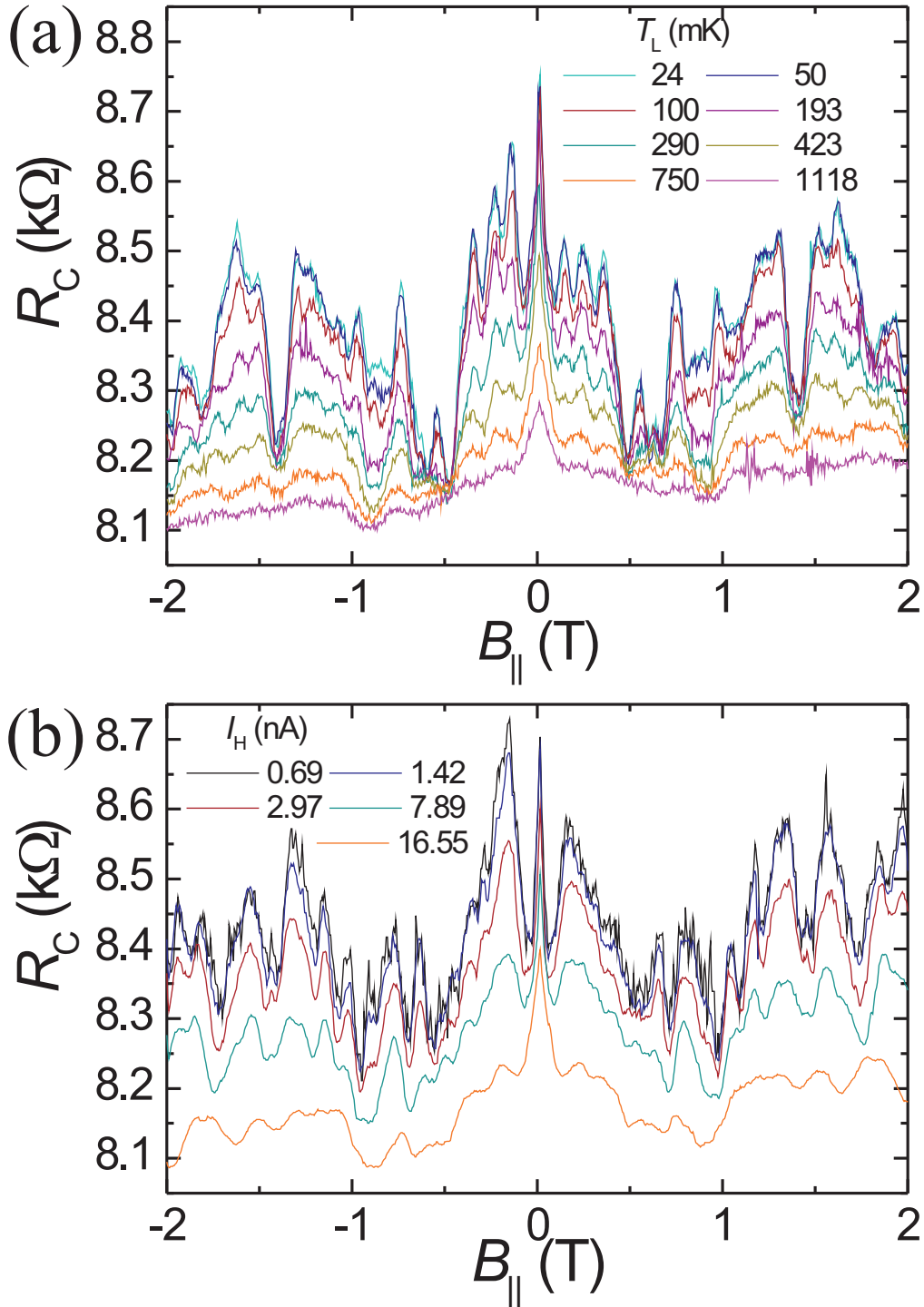
Fig. 3.9: Resistance of the heating channel as function of magnetic field applied parallel to the 2DEG at various lattice temperatures (a) and various heating currents (b).

magnetic field line. The fluctuation amplitude decreases for higher temperatures and increasing heating currents. At $B_\parallel = 0$ T, a sharp peak can be observed, which shows a slightly different temperature (current) dependence than the other magneto-resistance fluctuations. This is most obvious at higher temperatures (currents). For $T_L = 1118$ mK ($I_H = 16.55$ nA), this peak is still visible while the fluctuations for $B_\parallel \neq 0$ T, have almost vanished. Thus, it can be inferred that the peak at $B_\parallel = 0$ T is caused by a different effect than the other fluctuations.

A magnetic field applied parallel to the 2DEG changes the Zeeman energy of spin up and spin down electrons in the 2DEG, which is not expected to modify the scattering at these small fields. Thus, the magneto-resistance pattern most probably results from a small misalignment of the field out of the plane of the 2DEG. Under this assumption, the observed pattern represents the magnetic fingerprint of the sample due to the orbital effects of a finite perpendicular field component. The finger print can be divided into two parts. The first part, the peak at $B_\parallel = 0$ T, is a result of the coherent back-scattering of the electrons traversing the heating channel, which is commonly known as weak localization. This quantum mechanical interference effect dominates in long channels $L \gg l_\phi$ (l_ϕ: phase coherence length), and can be lifted by applying a small magnetic field, which is perpendicular to the plane of the 2DEG and which breaks the time-reversal symmetry of the back-scattering processes. The second part, the resistance fluctuations for finite magnetic fields, are due to the quantum mechanical interference of the electron waves along different paths through the narrow channel, which can be reversibly modified by the $B_\perp$-component of the magnetic field. This interference effect predominates in shorter samples since it is proportional to $(l_\phi/L)^{3/2}$. A more detailed discussion can be found in Ref.[BvH91] and references therein. In this context, it is more important that the phase coherence length l_ϕ depends on the temperature of the electron gas, and that both effects are caused by the local confinement of the heating channel.

For the temperature calibration, the temperature and current dependence can be analyzed with the help of either the weak localization peak, or the resistance fluctuations at finite magnetic fields. Here, the analysis of the resistance fluctuations, which shows higher statistical stability, is presented.[9] Figure 3.10(a) shows the relative standard deviation of the magneto-resistance fluctuations as a function of the lattice temperature for two different heating currents. The double logarithmic plot is divided into three temperature regimes. (1) For lattice temperatures above $T_L \gtrsim 200$ mK, a linear decrease of the relative fluctuation amplitude is observed. (2) For intermediate temperatures, the fluctuation amplitude saturates toward lower temperatures. (3) For $T_L \lesssim 80$ mK, the relative fluctuation amplitude is constant.

---

[9]It is noted that there is a difference in the overall line shape between temperature and current dependent measurements of Fig. 3.9. This difference results from a potential shift of the QD. Note that the overall resistance of the heating channel can vary by $\delta R_C(V_P)/\bar{R}_C(V_P) = 0.05$ depending on the potential of the QD.
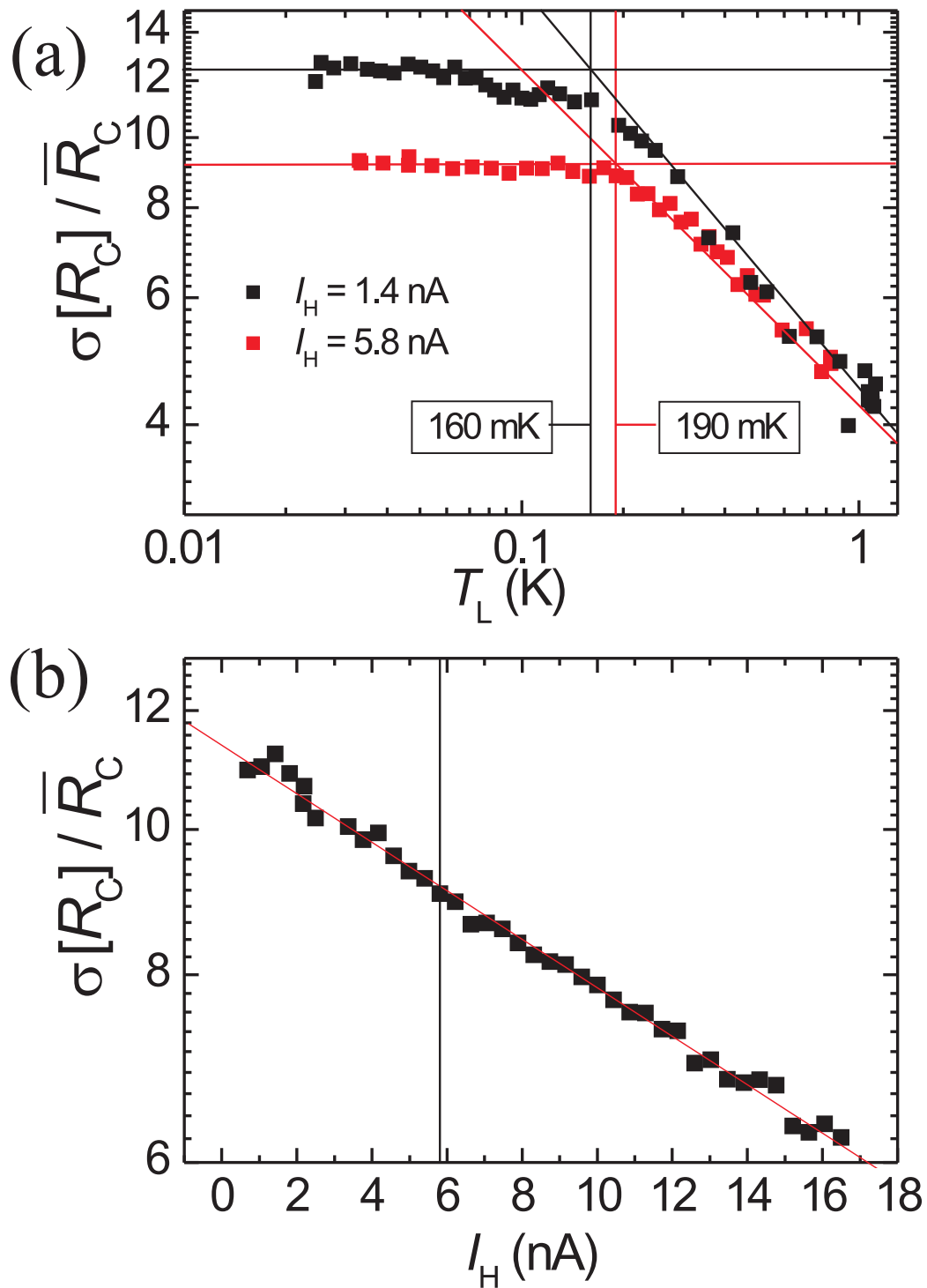
Fig. 3.10: Relative magneto-resistance fluctuation amplitude $\sigma(R_C)/\bar{R}_C$ as function of lattice temperature T_L (a), and heating current I_H (b). For the curves in (a) the heating current is $I_H = 1.4$ nA. The curves in (b) are taken at base temperature of the cryostat ($T_L = 10$ mK).

Besides unwanted electromagnetic noise, which cannot be filtered out completely, the saturation value at low temperatures depends on the applied heating current, as shown in the semi-logarithmic plot of Fig. 3.10(b).

The behavior can be explained by the temperature dependence of the electron gas-lattice coupling. For $T_{\mathrm{L}} \gtrsim 200$ mK, the temperature of the electron gas is coupled to the lattice temperature. For $T_{\mathrm{L}} \lesssim 80$ mK, the coupling to the lattice temperature is strongly reduced. Here, the cooling power of the electron-phonon coupling is not sufficient enough to compensate the incoming heat due to the heating current and additional electromagnetic noise. The intersection point of the extrapolated high and low temperature behaviors marks the point where the excess heating contributions are comparable to the cooling due to the lattice-coupling. The difference between the corresponding lattice temperatures then is a measure of the temperature increase due to different heating currents. In the example shown here, the temperature difference is $\Delta T = 30$ mK [cf. Fig. 3.10(a)].

This technique has the advantage to locally probe the temperature of the heating channel. The result agrees well with the experimental findings presented in Chap. 5. However, it would take more than two temperature cycles to be able to make a more quantitative analysis.

Chapter 4

Cotunneling contribution to the thermopower of few-electron quantum dots

4.1 Introduction

In the past, thermopower measurements on QDs in the Coulomb blockade (CB) regime have yielded qualitatively different results: either a sawtoothlike line shape, or a line shape similar to the derivative of a single-electron-tunneling (SET) conductance peak is observed when the electrochemical potential is varied in order to change the number of electrons occupying the QD. So far, a sawtoothlike behavior has been observed mainly for many-electron QDs, while derivative-like line shapes are predominantly reported for smaller QDs at very low (millikelvin) temperatures [SMA$^+$93, GMB$^+$99, DSB$^+$97, DSB$^+$98]. In the following, thermovoltage measurements on gate-defined, lateral QDs, containing a few tens of electrons, are presented which allow the low-temperature line shape profile to be analyzed in detail. For a series of SET conductance peaks, a transition is observed from a full sawtooth line shape to a sawtooth with a periodic intermittent zero thermovoltage signal while the temperature is lowered from $T = 1.5$ K to $T < 100$ mK. This behavior is in qualitative agreement with recent theoretical considerations of Turek and Matveev [TM02] for many-electron QDs. The transition is associated with an increasing dominance of cotunneling processes for decreasing temperatures. In the measurements, it has been found that the regime of sequential tunneling, which dominates the transport in the vicinity of the SET conductance peaks, extends much further than anticipated for many-electron dots. This leads to an enhanced absolute thermopower for few-electron devices.
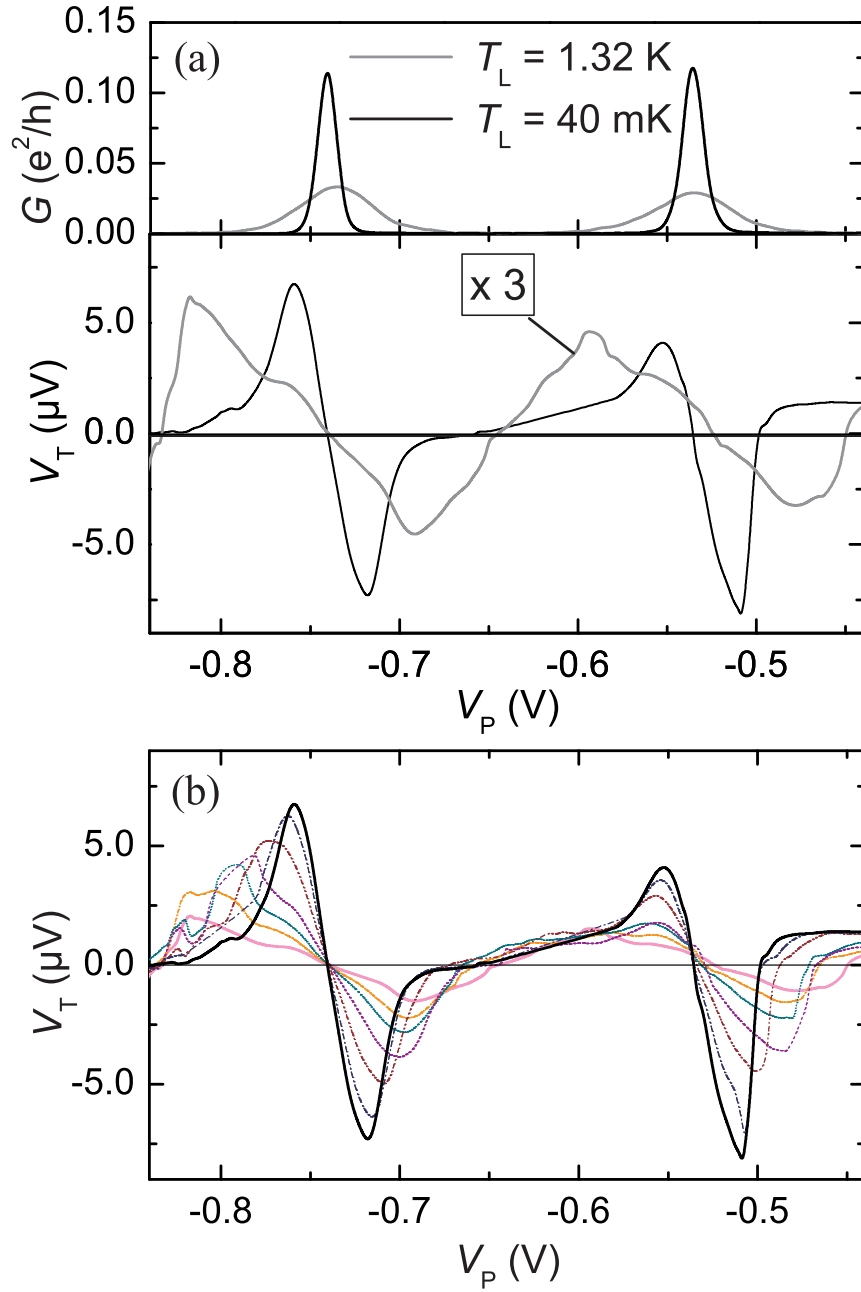
Fig. 4.1: (a) Conductance G (upper panel) and the corresponding thermovoltage V_T (lower panel) of QD1 as a function of the plunger-gate voltage V_P. (b) Thermovoltage curves as a function of V_P at seven different temperatures: $T_L = 40$ mK (black), 66 mK (brown), 158 mK (cyan), 257 mK (blue), 425 mK (orange), 1.04 K (pink) and 1.5 K (purple).

4.2   Experimental results

Here, two QD samples [QD1 (Bochum I3C) and QD2 (Bochum I4A)] are investigated that
have the same gate structure design [see Chap. 3.1.2 Fig. 3.2] but are adjusted differently
in their electrostatic confinement. They differ in their number of electrons, the coupling
to the reservoirs and level spacing. QD1 contains between 15 and 20 electrons, while QD2
contains between 30 and 40 electrons. In the whole temperature range, a constant ac
current of $I_H = 9.7$ nA (4.2 nA) has been used to increase the electron temperature in
the heating channel.

Figure 4.1 (a) shows the conductance G and the corresponding thermovoltage V_T
of QD1 for an electrostatic charging energy $E_C = 1.43$ meV at lattice temperatures
$T_L = 40$ mK (black lines) and 1.32 K (gray lines). At 1.32 K, thermal broadening
determines the shape of the SET conductance peaks. The corresponding thermovoltage
signal shows a sawtooth-like line shape with a maximum in the vicinity of the center of
the CB. An additional fine structure on the sawtooth line shape, which is even visible at
elevated temperatures, is due to the finite level spacings in the QD. At $T_L = 40$ mK the
SET conductance peaks have an increased height, a reduced width, and are well separated
by regimes of approximately zero conductance. The line shape of the corresponding
thermovoltage now resembles more the negative derivative of the conductance G. The
extremal values of the thermovoltage have increased by a factor of three and their positions
are shifted towards the SET conductance peaks.

A small asymmetry between the thermovoltage values of positive and negative am-
plitudes is observed for all measurements (cf. Fig. 4.1 and Fig. 4.10). Lower tunneling
probabilities, for strongly negative plunger gate voltages V_P, reduce this asymmetry. The
asymmetry is intrinsic and has been ascribed to the energy dependent transmission proba-
bility of the tunnel barriers and possible multi-channel tunneling processes [XY02, XX99].
Additionally, long shoulders are observable in the thermovoltage for the SET conductance
peak at $V_P = -0.54$ V. In this regime, the thermovoltage is highly sensitive to any asym-
metric contribution of cotunneling processes from above or below the Fermi-level, which
leads to a non zero V_T. As discussed in more detail in Chap. 5, the magnitude of these
contributions is controlled by the coupling and energetic position of the QD states. Sim-
ilar features occur in the spin correlated transport regime [SBR+05]; this is discussed in
Chap. 6.

Figure 4.1(b) shows V_T for seven different temperatures in the range from $T_L = 1.32$ K
down to 40 mK. It is evident that the change in line shape occurs continuously. In the
vicinity of the SET conductance peak, the thermovoltage varies linearly with V_P. Its slope
increases with decreasing T. In between the SET conductance peaks, however, a region
develops, where $V_T \simeq 0$. The observation of two different line shapes indicates that at
different temperatures different transport mechanisms dominate the electronic transport
properties.

4.3   Model calculations and comparison

Near the SET conductance peaks, the charge transport is dominated by sequential tunneling (ST) processes and is explained within the so-called orthodox model [BS92], where only first order tunneling processes are considered (see Chap. 1.2.1 and Chap. 2.2.1). Between the SET conductance peaks, the transport can also be due to ST processes, but only at relatively high temperatures (~ 1 K). In ST transport, the average electron energy is proportional to an effective energy gap E_{g} which is defined as the difference between the Fermi energy of the leads and the energy of the closest QD state. The value of E_{g} varies linearly between $-E_C^*/2$ and $+E_C^*/2$ with increasing electrochemical potential of the QD, Φ_{QD}, and subsequently jumps back to $-E_C^*/2$ at the center of the CB. According to Eq. (2.25), the thermovoltage follows this sawtoothlike behavior. Thermal smearing at higher temperatures leads to a more sinusoidal variation of E_{g} and thus the extremal values of the thermovoltage oscillations are located slightly away from the center of the CB. The ST mechanism thus explains the line shape at temperatures around 1 K.

The very low (millikelvin) temperature line shape is attributed to the occurrence of inelastic cotunneling (CT) transport in between the SET conductance peaks [TM02]. Sequential tunneling processes are thermally activated and thus exponentially suppressed by lowering the temperature, while CT processes scale only according to a power law [AN90]. Thus, the higher order processes dominate the transport away from the SET conductance peak at low temperatures. The average (kinetic) energy transferred by cotunneling processes is proportional to the temperature ($\langle E_{\mathrm{co}} \rangle \propto T$), because energy has to be conserved in CT transport. Therefore, the expected low temperature thermoelectric signal of CT processes is vanishingly small [TM02]. Decreasing the sample temperature implies a transition from ST- to CT-dominated transport in the CB regime away from the SET conductance peaks and thus a suppression of the thermovoltage signal in the corresponding gate voltage ranges. The sawtooth line shape becomes interrupted by regions of nearly zero signal amplitude, as observed in Fig. 4.1.

In order to discuss this transition more quantitatively, the thermovoltage oscillations at $V_{\mathrm{P}} = -0.73$ V are compared with the behavior of the orthodox (pure ST) [BS92] model, and a model that also includes CT effects [TM02].

For fitting the experimental findings with the pure ST model, Eqs. (3.13) and (3.14) from Ref. [BS92] have been used. Within the ST, picture the thermopower S is given by

$$
\begin{aligned}
S \;=\; \frac{L_{12}}{G} &= -\frac{e}{k_B T^2 G^{ST}} \sum_{p=1}^{\infty} \sum_{N=1}^{\infty} \frac{\Gamma_p^l \Gamma_p^r}{\Gamma_p^l + \Gamma_p^r} [\epsilon_p + E_{\mathrm{C}}(N) - E_{\mathrm{C}}(N-1) - E_F] \\
&\times\; P_{eq}(N) F_{eq}(\epsilon_p|N) \{ 1 - f[\epsilon_p + E_{\mathrm{C}}(N) - E_{\mathrm{C}}(N-1) - E_F] \},
\end{aligned} \tag{4.1}
$$

where the electrical conductance G^{ST} of the QD is given by

$$
\begin{aligned}
G \;=\; &-\frac{e^2}{k_B T} \sum_{p=1}^{\infty} \sum_{N=1}^{\infty} \frac{\Gamma_p^l \Gamma_p^r}{\Gamma_p^l + \Gamma_p^r} \\
&\times\; P_{eq}(N) F_{eq}(\epsilon_p|N) \{ 1 - f[\epsilon_p + E_{\mathrm{C}}(N) - E_{\mathrm{C}}(N-1) - E_F] \}. \tag{4.2}
\end{aligned}
$$

Fig. 4.2: (a) Calculated thermovoltage for the CT-included model (dotted lines) and measured thermovoltage (solid lines) as a function of V_P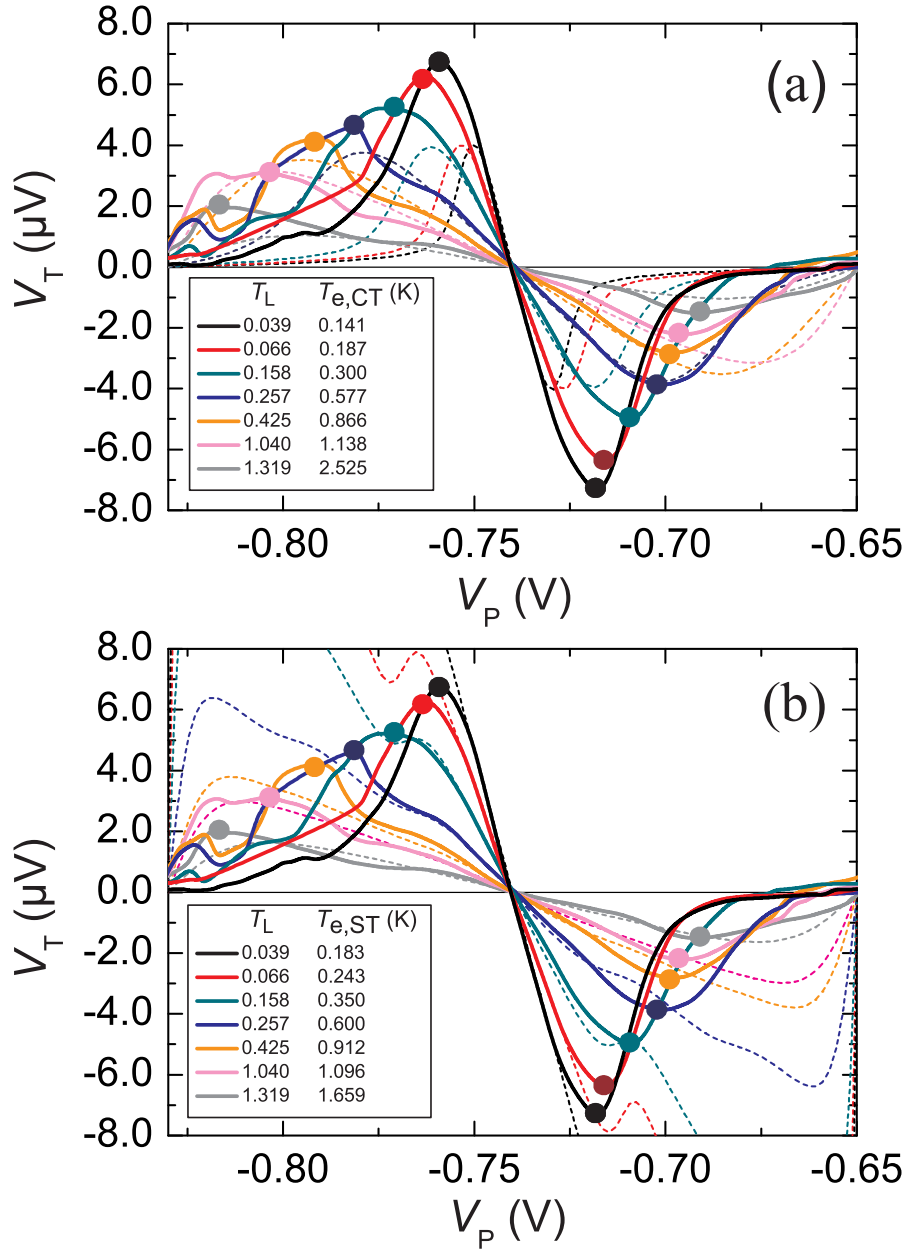. (b) Calculated thermovoltage for the ST model (dotted lines) and measured thermovoltage (solid lines) as a function of V_P. The insets give the extracted electron temperatures from the curve fitting. Dots mark the extremal values of the thermovoltage line shape. Their positions are the same as the positions of the dots in Fig. 4.3.

Here, p denotes the individual QD states, $\Gamma^{(r,l)}$ the tunnel coupling to the right and the left reservoir, $E_C(N)$ the charging energy of the N-electron QD, P_{eq} the probability that the QD contains N electrons, F_{eq} the conditional probability in equilibrium that level p is occupied, given that the QD contains N electrons, and f the Fermi distribution. Furthermore, the ST curves shown in Fig. 4.2 (b) and Fig. 4.3 are computed for a series of equidistant non-degenerate QD levels, assuming level-independent tunnel rates.

The CT-included model incorporates the effects of cotunneling by assuming that the thermoelectric (kinetic) coefficient L_{12} and the electrical conductance G are given in an expansion of first and second order transport processes:

$$S = \frac{L_{12}}{G} = \frac{L_{12}^{ST} + L_{12}^{CT}}{G^{ST} + G^{CT}}. \tag{4.3}$$

The sequential tunneling contributions to the electric conductance and the thermoelectric coefficient are calculated by using the results from the Beenakker [Bee91, BS92] theory in the limit of negligible spacing of the QD states at low temperatures $k_B T \ll E_C$.

$$L_{12}^{ST} = \frac{G_l G_r}{4(G_l + G_r)} \frac{e(\phi - \phi_N)^2/T^2}{\sinh[e(\phi - \phi_N)/T]} \tag{4.4}$$

$$G^{ST} = \frac{G_l G_r}{2(G_l + G_r)} \frac{e(\phi - \phi_N)/T}{\sinh[e(\phi - \phi_N)/T]} \tag{4.5}$$

In the same limit, the inelastic cotunneling contributions of the electrical and thermal conductances can be approximated in the following way:

$$L_{12}^{CT} = -\frac{4\pi^3}{15} \frac{\hbar}{e^3} G_l G_r (k_B T)^3 \left(\frac{1}{u_1} + \frac{1}{u_{-1}}\right)\left(\frac{1}{u_1^2} - \frac{1}{u_{-1}^2}\right), \tag{4.6}$$

$$G^{CT} = \frac{\pi \hbar}{3e^2} G_l G_r (k_B T)^2 \left(\frac{1}{u_1} + \frac{1}{u_{-1}}\right)^2, \tag{4.7}$$

where $u_{\pm 1} \equiv E(N \pm 1) - E(N) = e(\phi_N - \phi)$ and N is determined by minimizing the electrostatic energy of the dot for a given potential ϕ. From Eqs. (4.6) and (4.7), the cotunneling thermopower S_{CT} is given by the following:

$$S_{CT} = \frac{4\pi^2}{5} \frac{k_B T}{e^2} \left(\frac{1}{\phi - \phi_N} + \frac{1}{\phi - \phi_{N-1}}\right), \tag{4.8}$$

which reflects the $1/\phi$ behavior in the potential range between two conductance peaks. Note that Eq. (4.8) formally diverges at the center of the conductance peaks. The regularization of the divergencies is presented in Ref. [TM02], and will not be repeated here. The results for the cotunneling contributions L_{12}^{CT} and G^{CT} at arbitrary temperatures which have been used for fitting the line shape of the measured thermovoltage oscillations

are given by

$$
\begin{aligned}
G^{CT} &= \frac{\hbar}{e^2}\frac{G_l G_r}{4\pi}\sum_{N=-\infty}^{\infty}\left[(W_{N-1}^{(0)}+W_N^{(0)})F\left(\frac{E(N)-E(N-1)}{2k_BT}\right)\right.\\
&\left.-\frac{4k_BTC}{e^2}(W_{N-1}^{(0)}+W_N^{(0)})F^*\left(\frac{E(N)-E(N-1)}{2k_BT}\right)\right],
\end{aligned}
\tag{4.9}
$$

$$
\begin{aligned}
L_{12}^{CT} &= -\frac{\hbar}{e^3}\frac{G_l G_r}{4\pi}\sum_{N=-\infty}^{\infty}\left[(W_{N-1}^{(0)}+W_N^{(0)})F_T\left(\frac{E(N)-E(N-1)}{2k_BT}\right)\right.\\
&\left.-\frac{4k_BTC}{e^2}(W_{N-1}^{(0)}+W_N^{(0)})F_T^*\left(\frac{E(N)-E(N-1)}{2k_BT}\right)\right],
\end{aligned}
\tag{4.10}
$$

where $W_N^{(0)}\equiv e^{-E_N/k_BT}/\sum_N e^{-E_N/k_BT}$ stands for the equilibrium probability distribution of the dot charge, and the functions $F(x)$, $F^*(x)$, $F_T(x)$ and $F_T^*(x)$ are defined by

$$
F(x) \equiv |x|\int_0^\infty \frac{dz}{z^2}\left(\frac{(1+z)^2}{\sinh^2[x(1+z)]}+\frac{(1-z)^2}{\sinh^2[x(1-z)]}-\frac{2}{\sinh^2[x]}\right),
\tag{4.11}
$$

$$
F^*(x) \equiv x|x|\int_0^\infty \frac{dz}{z}\left(\frac{(1+z)^2}{\sinh^2[x(1+z)]}-\frac{(1-z)^2}{\sinh^2[x(1-z)]}\right),
\tag{4.12}
$$

$$
F_T(x) \equiv x|x|\int_0^\infty \frac{dz}{z^2}\left(\frac{(1+z)^3}{\sinh^2[x(1+z)]}+\frac{(1-z)^3}{\sinh^2[x(1-z)]}-\frac{2}{\sinh^2[x]}\right),
\tag{4.13}
$$

$$
F_T^*(x) \equiv x^2|x|\int_0^\infty \frac{dz}{z}\left(\frac{(1+z)^3}{\sinh^2[x(1+z)]}+\frac{(1-z)^3}{\sinh^2[x(1-z)]}\right).
\tag{4.14}
$$

At $T_{\rm L}= 1.0$ K, both models exhibit nearly the same thermovoltage amplitude and approximately the same line shape [cf. Fig. 4.3]. For this temperature, the temperature of the electron gas $T_{\rm e}$ is assumed to be equal to the lattice temperature $T_{\rm L}$, and the QD fulfills the condition $\hbar\Gamma \ll k_BT \ll E_{\rm C}$, which allows the relevant model parameters to be extracted. From fits of the SET conductance peaks [cf. Fig. 4.5], we obtain $E_C^* = 1.712$ meV, $\alpha = \Phi_{\rm QD}/(-eV_{\rm P}) = 0.0095$, and $G_{l,r} = 0.072\,e^2/h$, where $G_{l,r}$ describes the tunnel conductance to the left and right reservoirs, respectively. The temperature difference can be extracted by fitting the thermovoltage line shape at the same temperature ($T_{\rm L} = 1.0$ K). The result is a temperature difference of $\Delta T = 9$ mK [cf. Fig. 4.2]. The temperature dependent thermovoltage shown in Fig. 4.3 is calculated by considering these parameters as temperature independent. Since sequential tunneling, and hence the charging energy of the QD, determines the slope $m_{V_{\rm T}}$ of the thermovoltage signal in the close vicinity of the SET conductance peaks, the direct comparison with experiment allows the effective electron temperature $T_{\rm e}$ under the experimental conditions to be extracted. The slope $m_{V_{\rm T}}$ is given by

$$
m_{V_{\rm T}} \approx \frac{\Delta V_{\rm T}}{\Delta V_{\rm P}} \propto \frac{\langle E\rangle}{T},
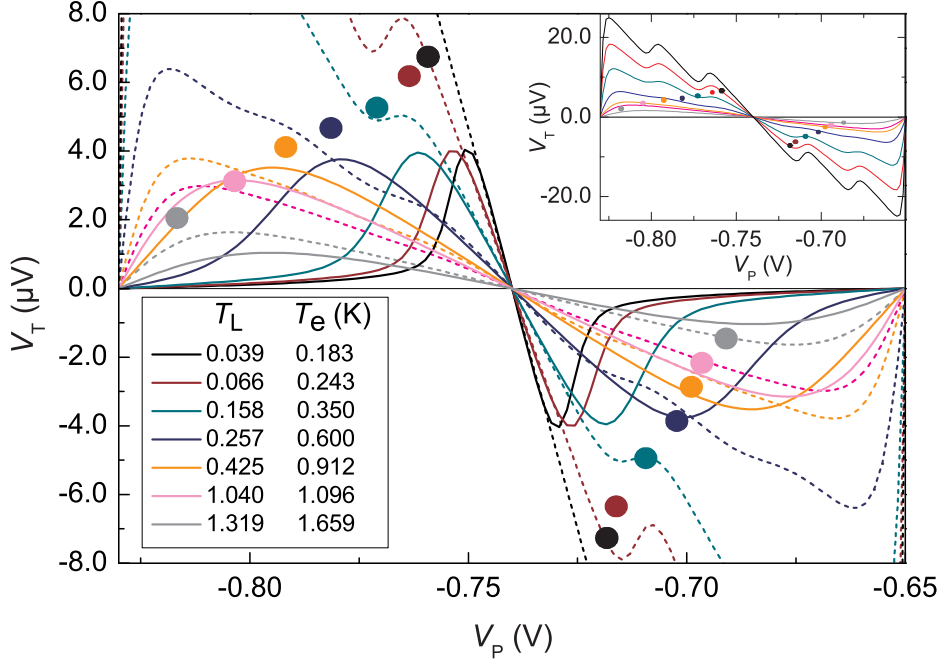\tag{4.15}
$$

Fig. 4.3: Calculated thermovoltage for the orthodox (dotted lines) and CT-included model (full lines) as a function of V_P. The dots indicate the maxima of the measured thermovoltage signal. The inset shows the orthodox model at full scale.

where Eq. 2.25 has been used. Figure 4.2 shows the model calculation for the CT-included model [Fig. 4.2 (a)], and the pure ST model [Fig. 4.2 (b)] together with the experimental data. The temperature dependent change of m_{V_T} results in a difference between the extracted electron temperatures of the two models. The difference occurs due to the fact that the CT-included model neglects the finite level spacing in the QD, whereas the ST-model accounts for these effects. The temperature dependent evolution of m_{V_T} is given in Fig. 4.4. In contrast to the CT-included model, which shows a uniform temperature dependence of m_{V_T} in the whole temperature range, the ST model calculations reveal a non-linear behavior in the higher temperature range of the double logarithmic plot. In Fig. 4.3, only the extremal values of the measured thermovoltage are indicated together with the results of the model calculations. In the orthodox model, a sawtooth line shape is predicted for all temperatures (Fig. 4.3, upper right inset). The wiggles at the declining slope of the sawtooth come from excited states and have the periodicity of the level spacing. At the same time, the CT-included model does indeed reproduce a transition from a sawtooth to a periodically suppressed sawtooth line shape. However, while the CT-included model predicts an approximately constant peak amplitude, the experiments show a strong increase in peak amplitude with decreasing temperature. In addition, the model
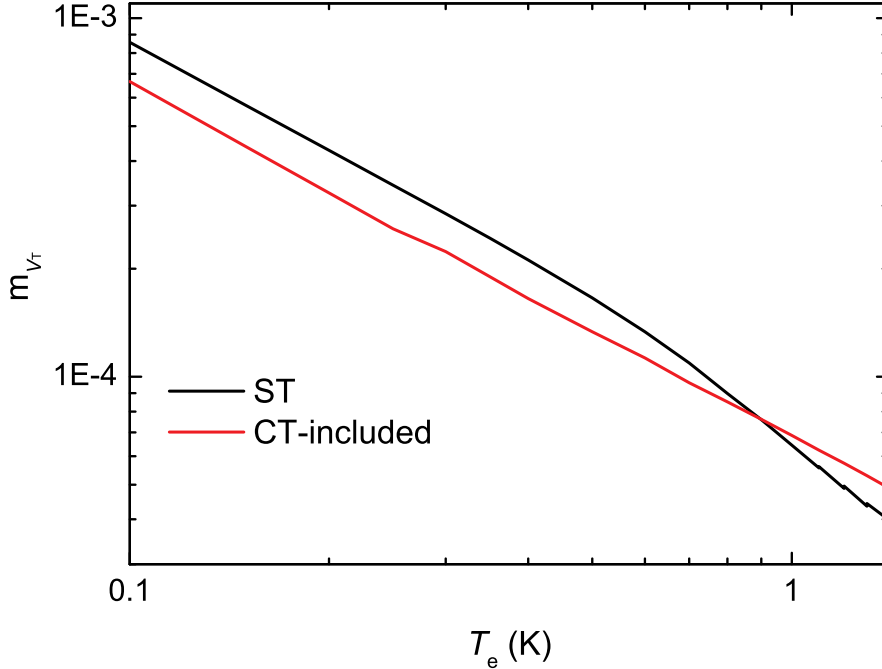
Fig. 4.4: Calculated slope of the thermovoltage in the close vicinity of a SET conductance resonance for ST and CT-included model.

does not predict the gate voltage position of the maxima correctly. The comparison of Fig. 4.1 and Fig. 4.3 reveals that in the experiment the linear increase of the thermovoltage around the SET conductance peak extends much further than anticipated by the CT-included model, and rather follows the behavior of the orthodox model, i.e., the voltage range where ST dominates the transport is larger than given by the CT-included model. In other words, the CT-included model does not describe quantitatively the influence of CT processes for the few-electron QD.

The bottom left inset of Fig. 4.3 presents the deduced values for T_e from the ST model fit. These values represent an upper limit at low temperatures, and are in better agreement with the lattice temperature at high temperatures. The extracted temperatures have been confirmed independently by fitting the corresponding conductance peaks [Bee91, Vor04], which are shown in Fig. 4.5. The fitting procedure focused on the reproduction of the maximum peak amplitude of the SET conductance peak, since sequential tunneling is expected to be the main contribution at this point. Figure 4.6 shows the comparison of the temperatures determined from conductance measurements and thermovoltage measurements. The nonlinear temperature dependence which appears in all curves of Fig. 4.6 (a) is caused by the spacial separation of the sample and the temper-
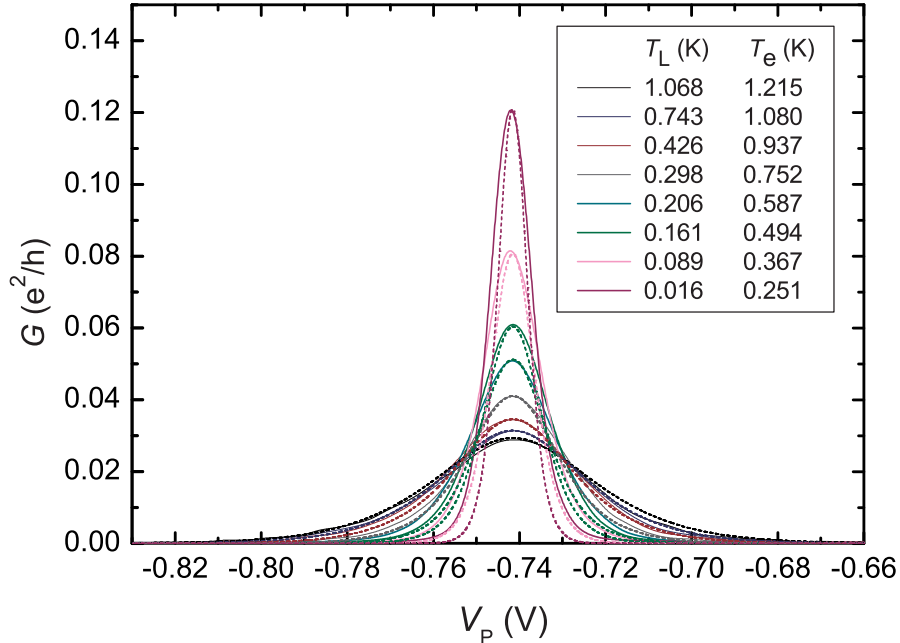
Fig. 4.5: Conductance of QD1 as a function of the plunger gate voltage. Full lines depict the experimental data, and dashed lines represent the corresponding fitted curves. The inset presents the measured lattice temperature T_L and the extracted electron temperature T_e.

ature sensor in the cryostat. Figure 4.6 (b) presents the good agreement between the temperature scales obtained from the fitting of the SET conductance peaks $T_\mathrm{e,G-fit}$ and the slope of the thermovoltage in the vicinity of the SET conductance peak $T_\mathrm{e,S-fit}$ at a constant temperature difference.

4.4   Discussion and conclusion

The deviations between the experimental observations and the results from the theoretical calculations originate from three different effects.

1   The CT-included model assumes a negligible energy spacing of the QD states ($\delta E_\mathrm{QD} \ll k_B T$), as applicable for metallic dots. For the present few-electron QD, clearly, δE_QD is not negligible, since the energy gap between the ground state and the first excited state is of the order of 250 μeV. Even at temperatures around 1 K, only a few excited states are available for transport, which reduces the probability for inelastic cotunneling events. Interestingly, the deviations between the calculations and the experiment are small in the measurement of the thermovoltage, while the finite energy spacing shows strong ef-
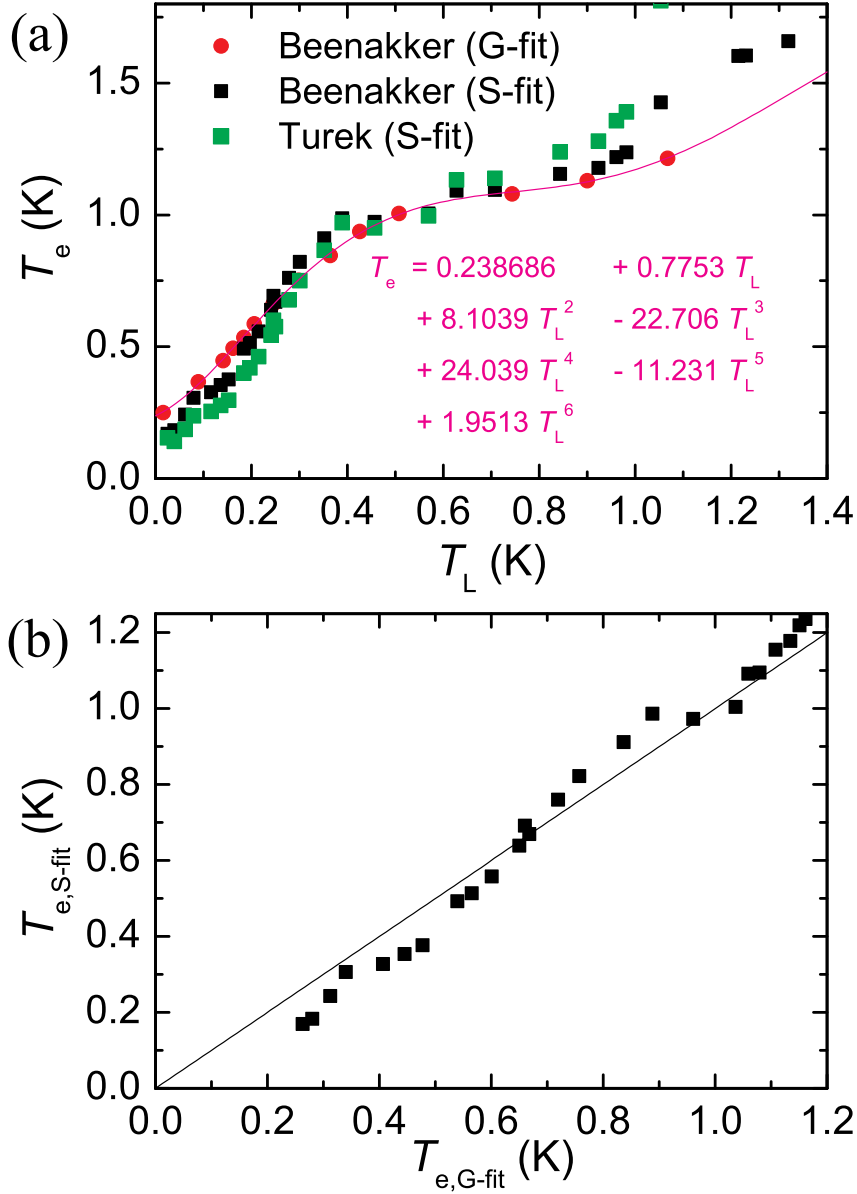
Fig. 4.6: (a) Electron temperatures T_e extracted from conductance measurements and thermovoltage measurements as function of lattice temperature T_L. The conductance has been fitted with a sequential tunneling model [Beenakker (G-fit)] [Bee91], the thermovoltage has been fitted with the ST-model [Beenakker (S-fit)] [BS92] and the CT-model [Turek (S-fit)] [TM02]. The red line is a polynomial fit to the conductance fit points. (b) Electron temperatures $T_{e,S-fit}$, which have been obtained from fitting the thermovoltage as a function of the electron temperature scale $T_{e,G-fit}$, which is shown by the red line in (a). The black line in (b) indicates $T_{e,G-fit} = T_{e,S-fit}$.

Fig. 4.7: Calculated temperature dependence of the SET conductance peak amplitude for the CT-included model (brown line), the ST model (blue line). For comparison, the experimental data (red squares) have been added.

fects in the temperature dependence of the maximum amplitude of the SET conductance peaks G_{max}. Figure 4.7 displays G_{max} as a function of the electron temperature for the CT-included and the ST models. While the maximum electrical conductance used in the CT-included model is temperature independent, th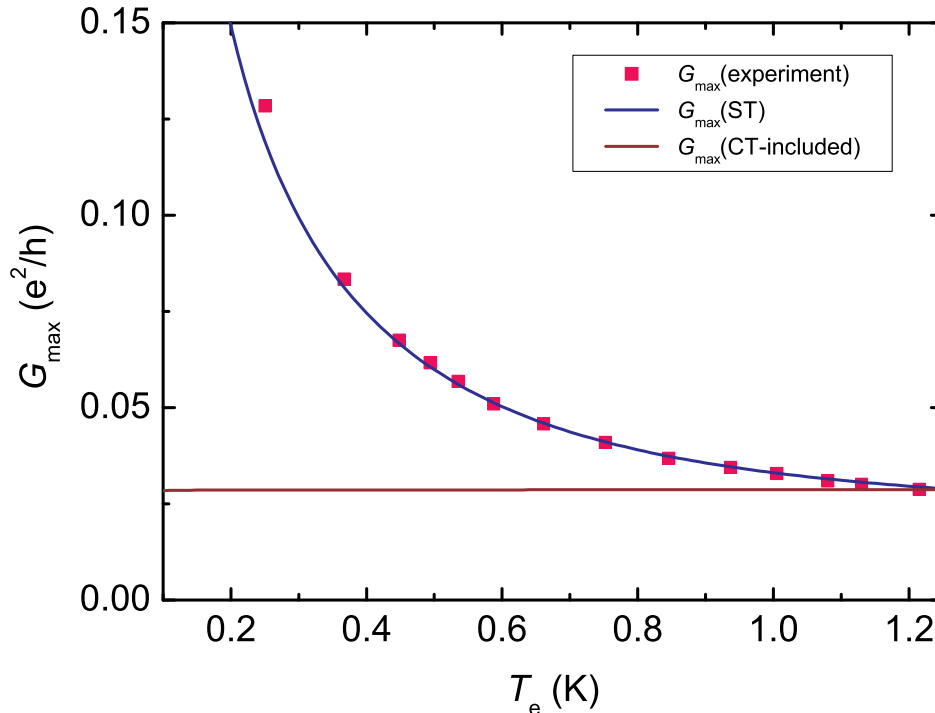e ST model shows a $1/T$ increase towards low temperatures, which agrees with the experimental observation. The behavior of G_{max} in the CT-included model and in the ST model is characteristic for the transport regimes of classical Coulomb blockade and quantum Coulomb blockade, respectively [KMM+97]. It shows that only individual QD levels are available for the charge transport through the QD. In the CT-included model, however, a quasi continuum of QD states contributes to the transport. This assumption may lead to an overestimation of the total number of inelastic cotunneling scattering channels and hence to the deviations of the measurement results with respect to the CT-included model calculations.

2 The reduction of the electron temperature leads to a considerable increase in the electron-electron scattering length l_{ee} [GQ82]. If l_{ee} exceeds the length of the heat-

ing channel at very low temperatures,[1] one expects that the energy does not fully re-distribute among the electrons within the heating channel. In this case, the difference between electron distributions in the QD leads ($f_{\mathrm{hot}} - f_{\mathrm{cold}}$) is determined by the excitation voltage across the heating channel $V_{\mathrm{ex,chan}}$ and the temperature broadening of the electron distributions in the heating channel reservoirs given by ($f_{hot} - f_{\mathrm{cold}} \propto f_1(T, \mu + eV_{\mathrm{ex,chan}}/2) - f_2(T, \mu - eV_{\mathrm{ex,chan}}/2)$). The energetically weighted particle distribution difference [$E \times (f_{\mathrm{hot}} - f_{\mathrm{cold}})$], which enters into the calculation of the thermopower, is depicted in Fig. 4.8 for three different temperatures. Black lines correspond to the energetically weighted derivative of the Fermi-Dirac distribution, which represents the result in the linear response regime for a fully thermally distributed heating channel reservoir [see also Chap. 2, Eqs. (2.15) and (2.22)]. For $k_B T_{\mathrm{e}} > eV_{\mathrm{ex,chan}}$, only a tiny difference exists between the fully thermalized and the non-thermalized particle distribution. For $k_B T_{\mathrm{e}} < eV_{\mathrm{ex,chan}}$, the voltage drop across the heating channel leads to an enhanced occupation of higher energy states compared to the Fermi-Dirac distribution. Since the thermovoltage in the vicinity of a SET conductance peak reflects the weighted particle distribution as a function of the QD potential, this effect enhances the transport contributions of high energetic sequential tunneling events at very low temperatures. For the interpretation of thermopower measurements, this means that the actual particle distribution in the heated lead has to be taken into account if this kind of current heating technique is used.

3 The temperature difference across the QD depends on the temperature itself [$\Delta T(T)_{\mathrm{e}}$] and may not be constant over the whole temperature range. In this case, the measured thermovoltage curves have to be fitted using both the temperature and the temperature difference. To obtain a reasonable estimate for the actual electron temperature, the electron temperature of the conductance measurements can be used. Figure 4.9 shows the corresponding temperature differences, which have to be applied across the QD in order to maintain the measured slope of the linearly increasing thermovoltage signal at the positions of the SET conductance peaks. This procedure allows the temperature difference as a function of the electron temperature to be obtained. The temperature difference increases from $\Delta T \approx 8$ mK at $T_{\mathrm{e}} = 1.4$ K to $\Delta T \approx 12$ mK at $T_{\mathrm{e}} = 250$ mK. The data shows a plateau-like feature ($\Delta T \approx 9$ mK) in the temperature range from $T_{\mathrm{e}} = 1.2$ K to $T_{\mathrm{e}} = 600$ mK, and is strongly fluctuating in the subsequent temperature ranges. The small temperature difference and the strong fluctuations make it very difficult to further compare the data with independent measurements of the temperature increase in the heating channel. Thus, for future studies of this kind, it may be necessary to develop a reliable method for measuring the 2DEG temperature in the heating channel with an accuracy better than 10 %. Furthermore, more detailed studies should also

---

[1]A long-time cutoff in the theory of electron-electron interactions in a disordered conductor is given by the thermal length $\tau_T = \hbar/k_B T$, which gives a thermal length of 17.5 μm at $T = 100$ mK ($E_F = 10$ meV) [BvH91].
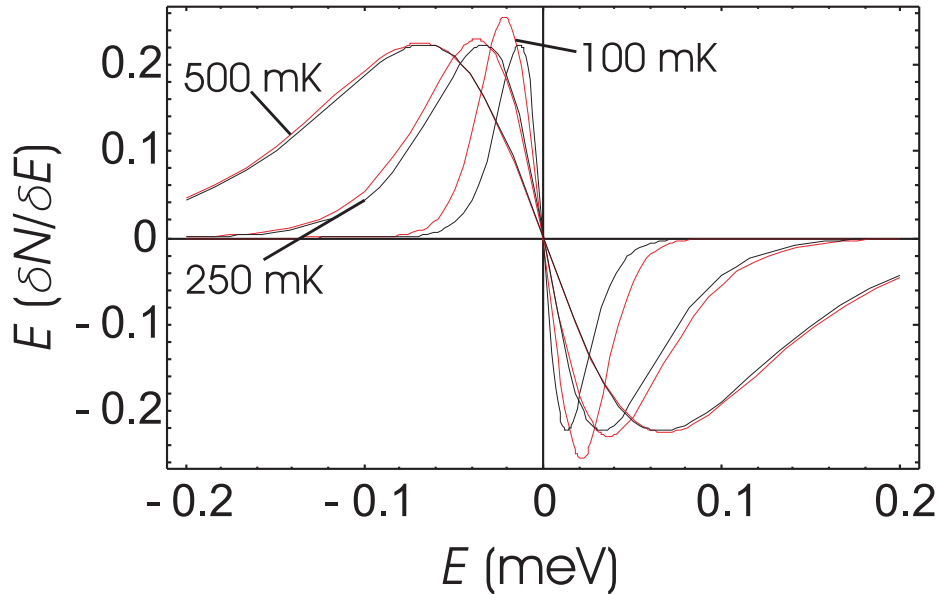
Fig. 4.8: Energy dependence of the energetically weighted particle distributions for various temperatures. Red lines correspond to the calculations for the case of missing energy redistribution via electron-electron scattering (see text). For the calculations, the excitation voltage across the heating channel has been set to $V_{\text{ex,channel}} = 50\mu$V. Black lines represent the energetically weighted derivative of the Fermi-Dirac distribution, which corresponds to a complete redistribution of the excess energy among the electrons in the heating channel system.

take into consideration quantum fluctuation effects in the thermopower of metallic QDs, which lead to an additional reduction of the charging energy gap [KK06], and thus also to the reduction in the slope of the thermovoltage oscillations at the center of the SET conductance peaks.

The above discussions show that the deviations between experimental observations and theoretical model calculations most likely result from a mixture of all three effects. In order to identify the individual contributions of these effects, more sophisticated experiments would be necessary. Especially, for the analysis of the particle distribution in the heating channel, it would be essential to provide a reliable technique which determines the temperature difference with high accuracy $[\delta(\Delta T) < 1$ mK] in the whole temperature range. From the theoretical point of view, further model calculations of S have to take into account the finite level spacing of the QDs. However, these effects do not necessarily modify the overall change in the line shape from a full sawtooth to a periodically intermitted sawtooth, which is the basis for further analysis of the additional (fine) structures in the following chapters.

In particular, the change of line shape persists in the strong coupling regime [see Chap. 6]. For the analysis of the thermopower in this regime, a second QD sample has been measured (cf. Fig. 4.10), which has the same layout as QD1. The quantum dot QD2
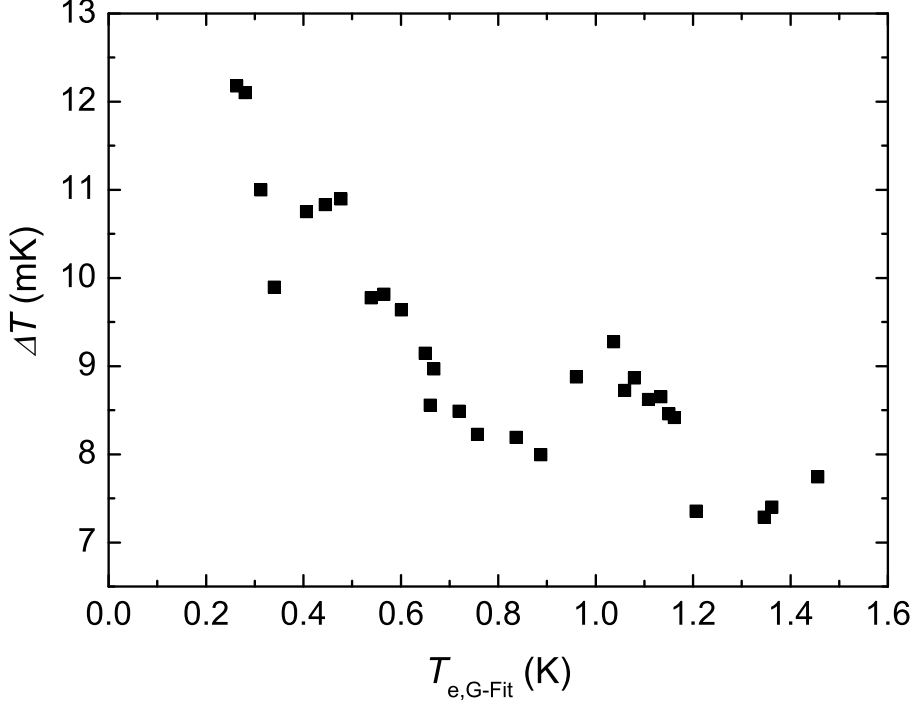
Fig. 4.9: Temperature difference across the QD as a function of the electron temperature, which has been extracted from the fitting of the SET conductance peaks.

exhibits a similar charging energy ($E_C^* \approx 1.5$ meV) but smaller level spacing ($\delta E \sim 50$ μeV) presumably due to variations in the potential landscape in the 2DEG [KBM00]. The characteristics of this sample go further into the many electron QD limit and the sample exhibits a very strong coupling of the QD states to the leads ($G_{l,r} \geq 0.7e^2/h$). Thus, one would expect strong cotunneling contributions to the thermopower. However, a similar behavior as for QD1 has been observed. Figure 4.10(a) shows the change of the thermovoltage line shape for a series of SET conductance peaks. The change in line shape with temperature is present. It can be identified by the shift of the thermovoltage extremal values towards the positions of the SET conductance peaks and by the appearance of a plateau like structure for low temperatures at $V_P = -1.85$ V. The change in line shape becomes less pronounced for more positive gate voltages, where the coupling of the QD states to the leads increases considerably. Since the theoretical models used are not really applicable in the strong coupling limit ($V_P > -1.85$ V), the line shape close to the SET conductance peak at $V_P = -1.9$ V has been used to evaluate the model calculations similar to QD1. Fig. 4.10(b) shows again that the regime of sequential tunneling is extended with respect to the expected curves based on the CT-included model.
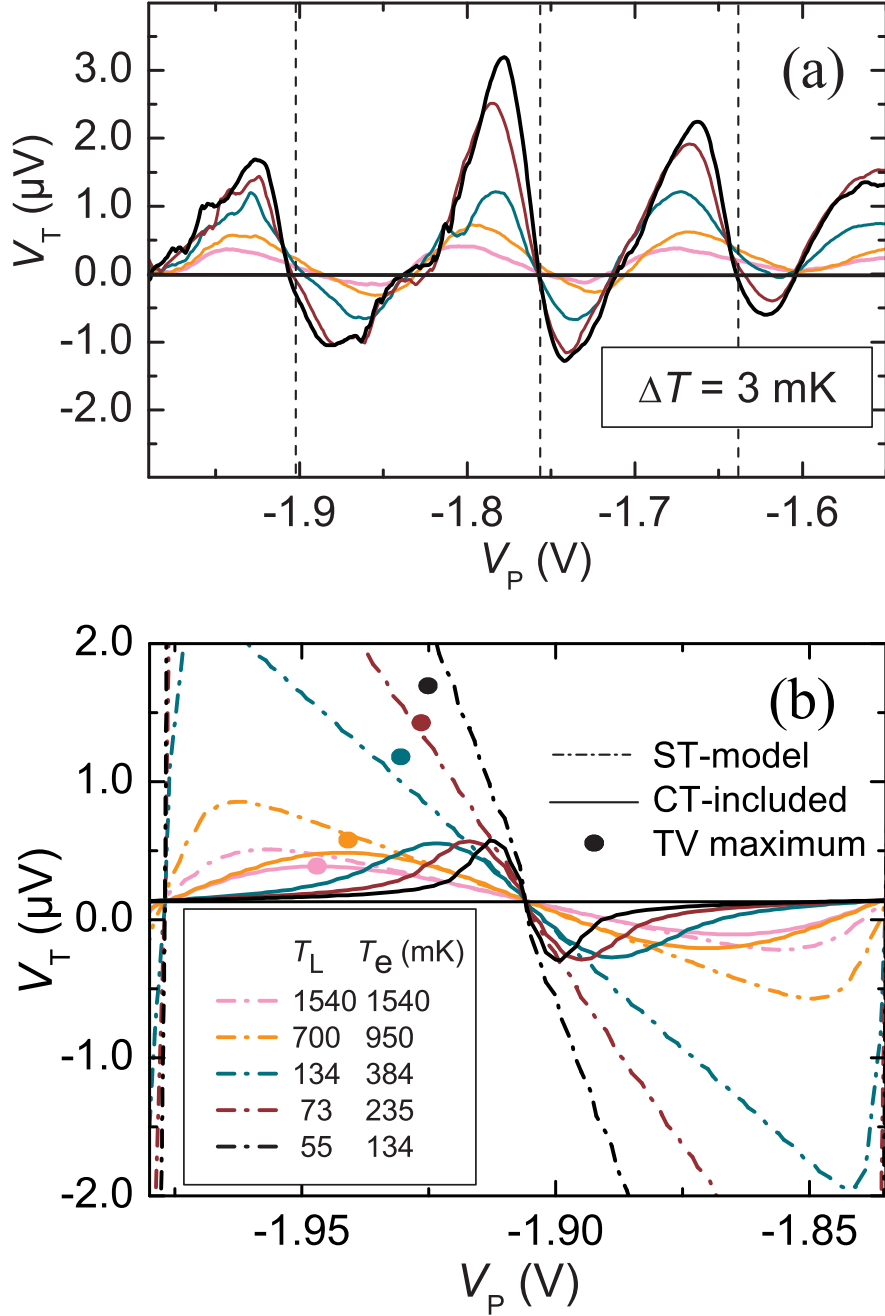
Fig. 4.10: (a) Thermovoltage for a series of SET conductance peaks as a function of the plunger gate voltage V_P for QD2. The positions of the SET conductance peaks are indicated by vertical dashed lines. (b) Calculated thermovoltage for the orthodox (dash-dotted lines) and CT-included model (full lines) as a function of V_P. The dots indicate the maxima of the measured thermovoltage signal near the SET conductance peak at $V_P = -1.9V$.

In summary, it has been established that the measurements of the thermopower of few-electron QDs show a temperature dependent change in the line shape of the thermopower oscillations as a function of the QD potential. This change agrees qualitatively well with the theoretical predictions for the contributions of sequential- and cotunneling transport. Deviations between model calculations and experimental data result because of the following three reasons. First, the model calculations do not account for the finite level spacing in the QD. Second, the electron distribution in the heated reservoir may differ from a fully thermalized Fermi distribution. Third, the calibration of the temperature difference varies over the temperature range of the measurement.

Chapter 5

Thermoelectric transport in the presence of asymmetries

In Chap. 4, it was shown that the overall line shape of the thermopower oscillations reflects the strength of the various transport mechanisms. Theoretical model calculations, which include sequential as well as cotunneling contributions to the thermoelectric transport, and experimental data show qualitatively good agreement. Very often, however, the experimental data deviates from the calculated ideal point-symmetric signal amplitude with respect to the position of the SET conductance peaks [e.g. see Chap. 4 Fig. 4.1 at V_{P} = -0.54 V].

Previous studies of the thermoelectric properties of QDs showed various types of asymmetries in the line shape of the thermopower oscillations. In Ref. [SMA+93], an overall offset has been reported for the thermopower of Coulomb blockade oscillations of large QDs. In Ref. [DSB+97] and in the previous chapter, an asymmetry has been observed between positive and negative oscillation amplitudes. In contrast to these results, no asymmetry of the thermopower oscillations has been observed in Ref. [GMB+99], although the difference between the tunneling barrier thicknesses has been varied in order to study the charging energy as a function of the dot-leads coupling strength.

So far, the underlying theoretical models consider energetically and spacially symmetric QD systems. The corresponding model calculations are based on the assumptions of an equidistant level spacing in the QD and a symmetric coupling of the QD states to both heat reservoirs. These assumptions are only partially fulfilled in a real QD structure. For example, the transition rates $\Gamma_{l,r}^{(i,j)}$ for electrons entering or leaving the QD have been assumed to be constant so far. However, in real QD systems, $\Gamma_{l,r}^{(i,j)}$ is given by [WHK95]

$$
\begin{aligned}
h\Gamma_{l,r}^{(i,j)} \;=\; & \frac{t_{l,r}}{2}|\langle S_i, M_i, \frac{1}{2}, \pm\frac{1}{2}|S_j, M_j\rangle_{CG}|^2 \\
& \times \left(f_{l,r}(E)\delta_{n_j,n_i+1} + [1 - f_{l,r}(-E)]\delta_{n_j,n_i-1} \right),
\end{aligned}
\tag{5.1}
$$

where $t_{l,r}$ denotes the transmittances of the tunneling barriers. The two participating n-electron states of the QD $|i\rangle$, $|j\rangle$ are associated with a certain electron number n_i, an

energy E_i, a total spin S_i, and a magnetic quantum number M_i. Besides the fact that the transmittance is not necessarily equal for electrons from the left and the right reservoirs, Eq. (5.1) contains Clebsch-Gordan coefficients $\langle...|...\rangle_{CG}$. Thus, the different states of the QD do not contribute in an equal way to the electric and thermoelectric transport.

This chapter deals with various deviations from an idealized QD structure and their implications for the thermopower measurements. Although, a broad variety of effects are presented, the selection does not claim completeness. There may be additional effects such as phase breaking [NK06], which have not been identified, and which are left for future studies.

Generally speaking, asymmetries in the line-shape of the thermopower oscillations can originate from three different sources: (a) the tunnel barriers, (b) a difference between the contacting heat reservoirs and (c) the internal degrees of freedom of the QD. In this regard, the chapter discusses the modification of the idealized line-shape of the thermopower oscillations as a result of (a) the energy dependence of the tunneling barriers, (b) the asymmetric coupling of given QD states to the source and the drain leads with respect to first order transport and (c) the influence of the excited QD states with respect to further asymmetries in first and second order transport.

5.1   Energy dependence of tunnel barriers

The QD connects to the leads via two tunnel barriers. Their shape can be characterized by an effective width and effective height. The transmission of an incident wave through a single barrier depends on the product of these two quantities [Sak94]. In linear conductance measurements, these two parameters cannot be accessed separately, so that the tunnel barriers are described by an overall transmission probability. The additional information on the tunnel barrier thickness and height, or shape, has to be obtained by the help of an additional experimental parameter such as the temperature, the bias voltage or the magnetic field.

The measurement of the linear thermoelectric power yields additional information about the dynamics of the system. Referring to Mott's formula [see Chap. Eq. (2.26)], the thermopower depends on the conductance and the derivative of the conductance with respect to the energy. Thus, one expects the information about the shape of the tunneling barriers to enter directly into the linear thermoelectric transport.

In the given QD structure, the shape of the tunneling barriers is determined by geometrical constraints and the dielectric material properties. Such geometrical constraints are, for example, the lithographical dimensions of the gates and the distance of the 2DEG to the surface. The dielectric material properties depend on the material composition, the donor concentration, the technique of doping (δ-doping or homogeneous doping) and, in the local vicinity of the gate electrodes, the cooling procedure of the sample [PLDL+05].
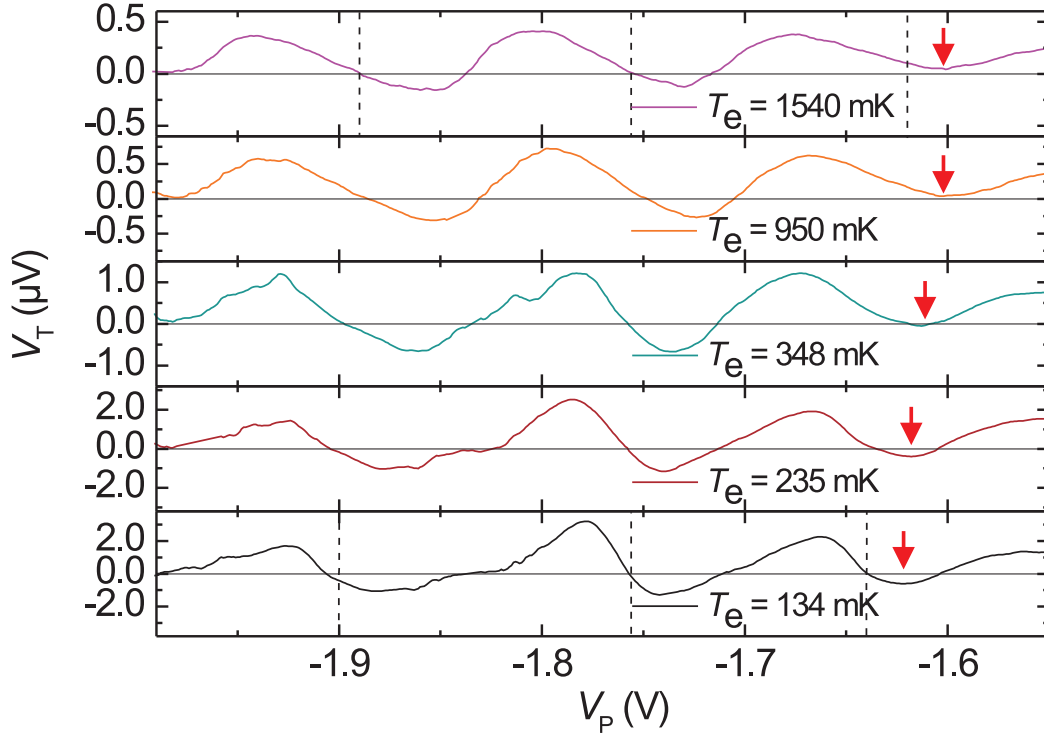
Fig. 5.1: Thermovoltage as function of plunger gate voltage in the strong coupling regime of a QD at six different temperatures. The arrows indicate the crossing from positive to negative oscillation amplitudes as the temperature is lowered. Vertical dashed lines indicate the position of the SET conductance peaks at the highest and lowest temperatures.

Changing the gate bias voltage within one sample alters both the height and the width of the tunneling barriers. A very sophisticated method is needed to keep one of these parameters constant while changing the other without changing the properties of the QD (e.g. the number of electrons). However, effects due to the energy dependence of the tunneling barriers can be distinguished from transport effects of the QD by their weak dependence on the plunger gate voltage in the presented experimental data. The thermoelectric contributions due to the energy dependence of the tunnel barriers are expected to add "homogeneously" to the effects due to the Coulomb-blockade over a wide range of the plunger gate voltage.

Figure 5.1 shows thermovoltage curves as a function of the plunger gate voltage V_P at six different temperatures. The bias voltages of the gates that form the tunneling barriers are kept at a constant value. Thus, the height and the width of the barriers are increased as the plunger gate voltage is tuned to more negative values [see also Chap. 3.1.2].

At the most negative plunger gate voltages ($V_P < -1.85$ V), the thermovoltage oscillations have nearly the same positive and negative signal amplitude in the vicinity of a SET conductance peak for all temperatures. At more positive plunger gate voltages ($V_P > -1.7$ V), a different behavior can be observed. At low temperatures, the extremal

values of the thermovoltage oscillations show enhanced positive thermovoltage amplitudes. As the temperature is increased, the negative oscillation amplitude is further reduced, and the oscillation minimum crosses the zero thermovoltage line at $T_e = 348$ mK. For even higher temperatures, a positive thermovoltage is observable even in the transport regime, where the effective energy gap of the SET QD state is negative, and the thermovoltage oscillation is completely positive [indicated by the red arrow in Fig. 5.1].

In order to explain the observed enhanced positive contribution to the thermovoltage at more positive plunger gate voltages, the coupling strength of the QD states to the leads has to be considered. At strongly negative plunger gate voltages, the tunneling barriers are high compared with $k_B T$, and one can assume energy independent barrier transmission in the energy window where thermoelectric transport takes place ($\sim E_F \pm k_B T$). QD states from above and below the Fermi level contribute with equal statistical weight to the electric and thermoelectric transport. Thus, the line shape is symmetric with respect to the zero voltage line. At more positive plunger gate voltages, the tunneling barriers decrease in height, and cannot be seen as energy independent within the energy window $\sim E_F \pm k_B T$. QD states from above the Fermi level of the leads couple stronger to the leads than QD states from below the Fermi level. The transmission through high energy states is more likely than through low energy states. Because the states above or below the Fermi level are responsible for the positive or negative contributions to the thermovoltage, respectively, positive transport contributions to the thermovoltage (electron-like transport) dominate over negative transport contributions to the thermovoltage (hole-like transport). This effect results in a temperature dependent distortion of the thermovoltage oscillations towards the positive thermovoltage scale. In some cases, the effect may even result in an offset.

With respect to the size of the QD, one would expect that in the many electron (metallic) limit, the line shape of the thermovoltage oscillations experiences a homogeneous offset or distortion, since a continuum of excited states contributes to the thermoelectric transport. In the few electron limit, where only a few QD states contribute to the thermoelectric transport, a more pronounced and a more irregular distortion is expected, since the coupling of single QD states strongly influences the balance between positive and negative thermopower contributions. As it is shown in Fig. 5.1, this tunnel barrier dependent effect becomes especially significant in the regime of strong coupling of the QD to the leads. This regime is discussed in more detail in Chap. 6.

5.2 Unidirectional thermoelectric transport in a SET conductance peak

While in the previous section the influence of the energy dependence of the tunneling barriers on the thermoelectrical signal was discussed, this part focuses on the internal symmetry properties of single QD states and their influence on the single electron tunneling transport. Equation (5.1) shows that the dynamics of various transport phenomena in QD structures crucially depend on the coupling strength of individual QD states to the leads [WHK95]. Even though there might be a spacial overlap of the wave functions of QD and 2DEG electrons, the transport can be fully blocked, if the Clebsch-Gordan coefficient is zero. Vice versa, in the physics of the Kondo effect in QDs, a spin-degenerate QD state with $S \geq 1/2$, which couples strongly to the reservoirs, can even lift the Coulomb blockade [GGSAM+98, COK98, vdWDFF+00, SBR+05].

So far, asymmetries in the coupling of individual QD states to the leads have been studied experimentally by finite-bias electrical transport measurements or by means of finite-bias single charge detection techniques [WHvKP93, SRI+05]. These measurements have shown that the occupation of excited states can suppress the transport occurring via transitions between QD ground states with different numbers of electrons.

Besides the advantage that the QD system is kept in close to equilibrium in a thermopower measurement, additional interest arises due to possible applications of QDs for efficient thermoelectric power generation or cooling [DiS99, GGB+06, KNY+98]. So far, however, detailed studies which clarify the role of asymmetrically coupled QD states in the thermoelectric transport have been missing .

For the analysis of first order thermoelectric transport using asymmetrically coupled QD states, the thermoelectric properties of a few-electron QD are compared with its excitation spectrum which has been obtained independently from nonlinear differential conductance measurements. It is shown that the line shape of the thermoelectric signal reflects the symmetry of the coupling of given QD states to the leads. By using magnetic fields up to $B_{\parallel} = 14$ T parallel to the plane of the 2DEG, a strong rectified (unidirectional) thermoelectrical transport is observed in a SET resonance instead of the commonly expected positive and negative contributions. This behavior is discussed with respect to the consequences for the thermoelectrical and thermal transport.

5.2.1 Experimental observation

Figure 5.2(a) shows a color scale plot of the zero-bias conductance in the regime of two SET conductance peaks at $V_P = -2.17$ V and $V_P = -2.33$ V as a function of plunger gate voltage V_P and magnetic field $B_{\parallel}$ applied parallel to the 2DEG plane. Dark colors correspond to high conductance and bright colors correspond to low conductance. Both SET conductance peaks, $\bar{\mu}_{N+1;N}$ and $\bar{\mu}_{N+2;N+1}$, shift towards more positive gate voltages with increasing magnetic fields. This diamagnetic shift is due to a different magnetic
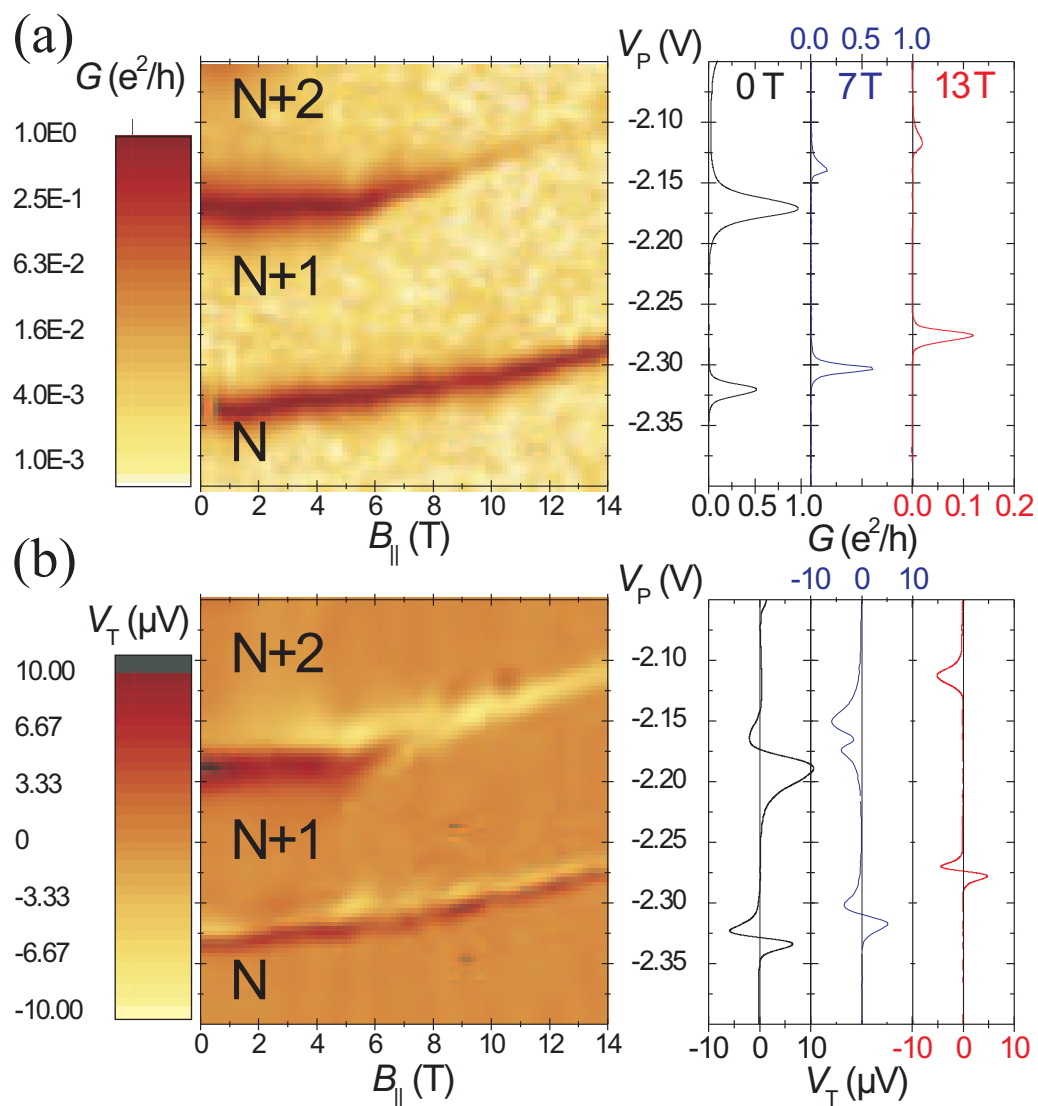
Fig. 5.2: (a) Color scale plot of the conductance G as a function of parallel magnetic field $B_{\parallel}$ and plunger gate voltage V_P. Dark regions represent high conductance on the logarithmic scale. (b) Corresponding color scale plot of the thermovoltage (linear scale).

field dependence of energy states in the QD and in the leads [WHvKP93, WHKP94, DGGW$^+$00, Ste68]. The amplitudes of both SET conductance peaks show qualitatively different behaviors as a function of the magnetic field. The SET peak at $V_\text{P} = -2.33$ V exhibits a moderate decrease of the peak amplitude towards high magnetic fields. The SET conductance peak at $V_\text{P} = -2.17$ V, however, starts decreasing at $B_\parallel = 5$ T and vanishes almost for magnetic fields higher than $B_\parallel = 8$ T. For clarity, single traces of $G(V_\text{P})$ at $B_\parallel = 0$, 7, and 13 T are shown in the right panel of Fig. 5.2(a).

The corresponding thermovoltage is shown in Figure 5.2(b). Dark and bright regions correspond to large positive and negative thermovoltage signals, respectively. The positions of the SET resonances can be identified by the sharp transition from positive to negative thermovoltages with increasing V_P. The line shape of the thermovoltage oscillations is in agreement with the results which have been discussed in Chap. 4. Close to the Coulomb blockade resonance, the transport is mainly due to sequential tunneling and the thermovoltage is proportional to the average energy gap between the QD resonance and the Fermi level in the leads [BS92]. Between two SET conductance peaks, the thermovoltage is approximately zero due to the energy conserving nature of the dominating cotunneling processes [TM02, KK06, SNB$^+$07a]. The observed diamagnetic shift is clearly visible in the thermovoltage measurement. The SET resonance at $V_\text{P} = -2.33$ V shows a uniform behavior for the whole magnetic field range while for the second resonance at $V_\text{P} = -2.17$ V, the thermovoltage exhibits significant changes for $B \geq 5$ T. For $B < 5$ T a regular resonance with a crossing from positive to negative thermovoltages can be observed. At 5 T $\geq B \geq 8$ T, an intermediate region is observable, where the thermovoltage positive to negative transition turns into a double peak structure with negative amplitudes. For $B > 8$ T, only a single negative thermovoltage signal remains. In contrast to the conductance measurements, the amplitude of the negative thermovoltage signal remains approximately unchanged. Traces of the thermovoltage at $B_\parallel = 0$, 7, and 13 T are plotted on the right hand side of Fig. 5.2(b).

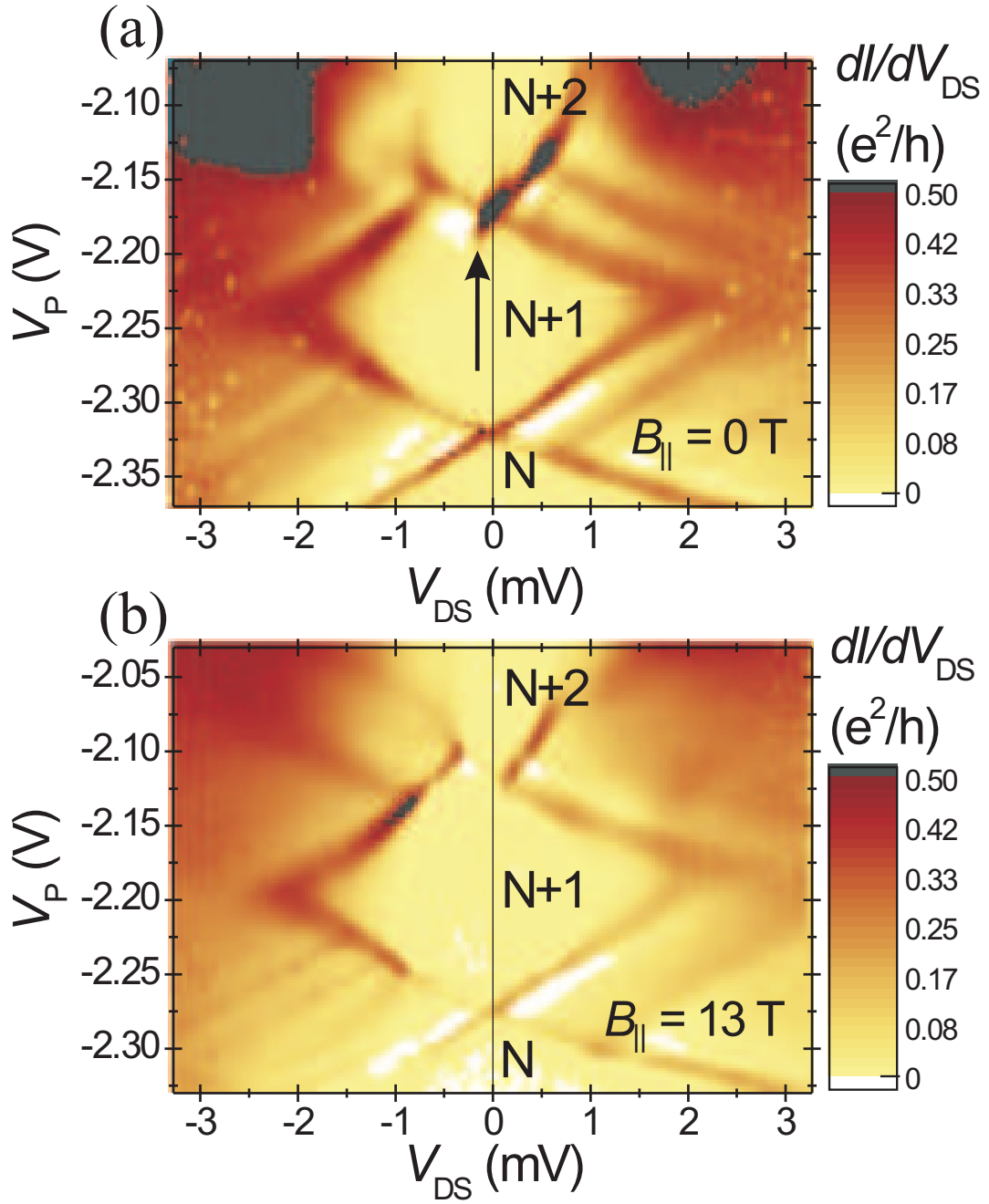**Fig. 5.3:** Color scale plot of the differential conductance as a function of drain-source voltage V_{DS} and plunger gate voltage V_P at (a) $B_\parallel = 0$ T and (b) $B_\parallel = 13$ T. The arrow marks the transition from a suppressed to a high differential conductance. The dashed line indicates the direction of numerical integration for the comparison of differential conductance and thermovoltage (see text).

In order to analyze the behavior of the $\bar{\mu}_{N+2;N+1}$ SET resonance at $V_{\mathrm{P}} = -2.17$ V in detail, the addition spectrum of the QD at $B = 0$ T is compared to the addition spectrum taken at $B = 13$ T. Figure 5.3 displays the nonlinear differential conductance as a function of plunger gate voltage and source drain voltage at $B_{\parallel} = 0$ T [Fig. 5.3(a)] and at $B_{\parallel} = 13$ T [Fig. 5.3(b)]. The familiar diamond shaped regions of zero (differential) conductance develop in the V_{DS}-V_{P} plane corresponding to fixed numbers (..., N-1, N, N+1, ...) of electrons on the QD [KMM$^+$97]. Borders of the Coulomb blockaded regime with negative slope indicate the alignment of ground states resonances with the source contact $\bar{\mu}_{\mathrm{S}} = \bar{\mu}_{n+1,0;n,0}$. Lines with positive slope correspond to the alignment with the drain contact $\bar{\mu}_{\mathrm{D}} = \bar{\mu}_{n+1,0;n,0}$. Lines outside the Coulomb blockade diamonds, originate from transport through excited states $\bar{\mu}_{n+1,i;n,j}$, where $(i,j) \in \mathbb{N}^+$ [FMM$^+$93]. The appearance of areas with negative differential conductance (white areas) are typical signatures for blocking mechanisms of various kinds [WHK95, DMTG02, Tew04]. For example, a first kind of blocking occurs due to interference of two competing transport channels. Once the second channel is energetically available, destructive interference reduces the total transmission probability. A second kind of blocking mechanism considers that due to fast inner dot transitions, the dot can relax into an excited state that is spin blocked for further transport or that takes place on a very much longer time scale.

At $B_{\parallel} = 0$ T, the SET resonance $\mu_{(N+2;N+1)}$ exhibits a negativ differential conductance for $V_{\mathrm{DS}} < -250$ μeV and $V_{\mathrm{P}} < -2.17$ V [onset indicated by an arrow in Fig. 5.3(a)]. The resonance line with a positive slope involving the ground state, $\mu_{N+2,0;N+1,0}$ is absent. The sudden jump in the differential conductance indicates that a QD state, which inhibits the charge transport, becomes energetically accessible for $V_{\mathrm{DS}} < -250$ μeV. From the asymmetric behavior with respect to positive and negative V_{DS}, it can be deduced that this blocking state couples asymmetrically to both contact reservoirs. In the following, the two participating QD resonances is denoted by $\bar{\mu}_{(N+2;N+1)}$ (regular resonance) and $\bar{\mu}^*_{(N+2;N+1)}$ (asymmetrically coupled resonance).

At $B_{\parallel} = 13$ T, the gate voltage range, where the transport for negative V_{DS} is inhibited, extends to more positive plunger gate voltages [cf. Fig. 5.3(b)]. At the zero bias $N+2 \leftrightarrow N+1$ transition, the transport is now dominated by the $\bar{\mu}^*_{(N+2;N+1)}$ resonance, which shows strongly suppressed transmission. The suppression of the differential conductance still occurs mainly for negative V_{DS}. Hence, an asymmetric transport gap opens for the zero bias $N+2 \leftrightarrow N+1$ transition.

5.2.2 Discussion

Obviously, the asymmetric transport gap results from a broken symmetry within the QD-leads system. The symmetry in charge transport between source and drain reservoirs can be broken either by a difference between the properties of source and drain[1] or due to an intrinsic asymmetry within the QD. Since the source and the drain reservoirs are equal in the experimental setup, they are not expected to be the origin of the observed asymmetric behavior. Thus, the source-drain-dependent asymmetric transport can be attributed to an intrinsic property of the QD.

In the following, it is shown that the interplay between two QD states which are energetically close to each other causes the asymmetry in the transport. At $B = 0$ T, the $\bar{\mu}_{(N+2;N+1)}$ resonance shows a high differential conductance for both transport directions (positive and negative V_{DS}). Therefore, the assumption is justified that this first QD state has a symmetric coupling to the source and the drain contact. The second state, couples strongly to the drain, while at the same time it couples very weakly to the source and thus determines the transport via the $\bar{\mu}^{*}_{(N+2;N+1)}$ resonance. At $B_{\parallel} = 0$ T, the symmetrically coupled state lies energetically below the the asymmetrically coupled state and represents the ground state of the QD.

If the state which couples asymmetrically lies energetically lower [cf. Fig. 5.3(b)], electrons from the drain are very likely to enter the dot into this state, but their further transport to the source is blocked. Electrons from the source reservoir are then expected to tunnel mainly into the symmetrically coupled state and leave the dot to the other side. Vice versa, if the state which couples symmetrically to both sides is the ground state, a much smaller difference can be expected between the transport in both directions.

Both the external gate voltage (V_{P}) and the magnetic field ($B_{\parallel}$), shift the energetic position of the QD states with respect to each other. V_{P} changes the strength and the shape of the confinement potential of the QD, which itself determines the level splitting between the QD states. The resulting energetic shift varies for states with different spacial orientations. By applying an in-plane magnetic field, the energies of the QD states shift due to the Zeeman effect according to $\delta E_{Z} = m_{J}g\mu_{B}B$, where m_{J} is the magnetic quantum number of the QD state with total angular momentum J, g is the associated g-factor, and μ_{B} is the Bohr magneton. For a single QD state, the orbital part of the electronic wave function remains almost unchanged when $B_{\parallel}$ is increased. This ensures that the coupling of this single QD state to the leads through the tunnel barriers is mostly independent of the magnetic field. If two states possess different magnetic quantum numbers, $B_{\parallel}$ can be

---

[1]The difference between source and drain can be due to differences in electron densities or magnetization. For example, an asymmetric transport gap can be accomplished in a spin blockade scenario where the addition of one electron to the dot is forbidden, since electrons from the leads can only change the spin state of the QD by $\Delta S = 1/2$, though at the same time the next available ground state transition would require $\Delta S > 1/2$. If, additionally, the electrons in the source were fully spin polarized and those in the drain were not, only a spin degenerate level would accomplish equal or symmetric transport between source and drain.
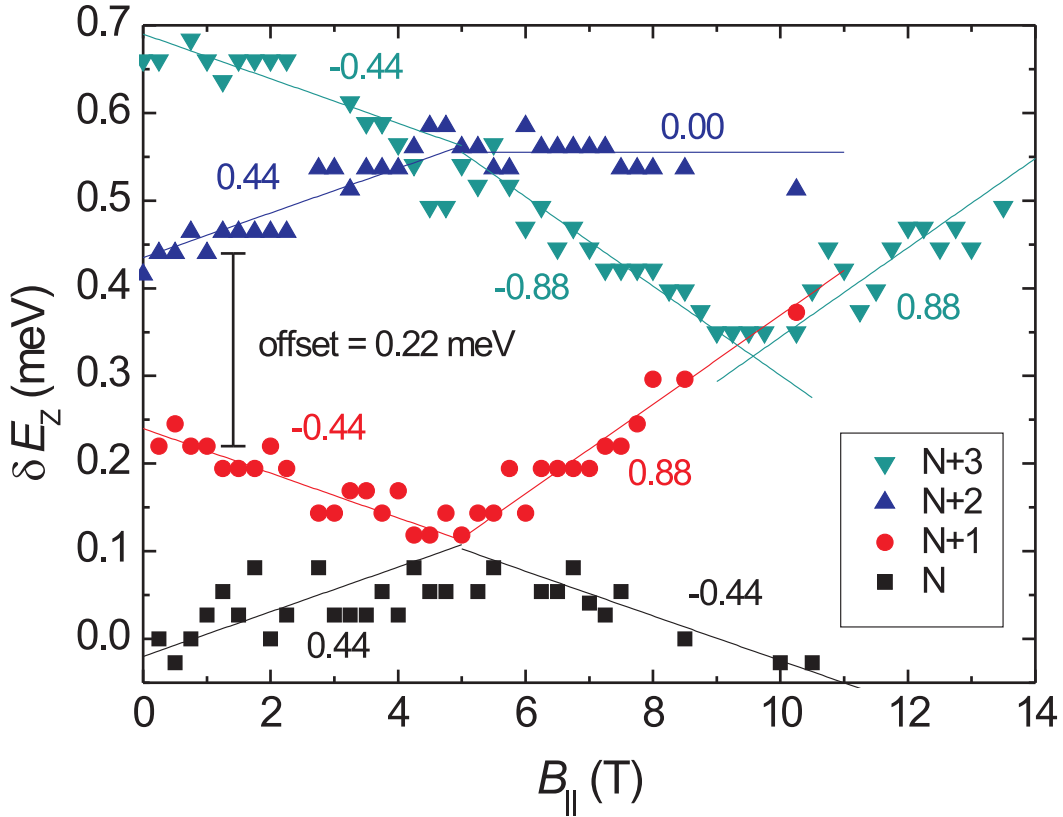
Fig. 5.4: Conductance peak spacings as a function of $B_\parallel$ for constant electron numbers in units of energy. The curves are offset for clarity. The lines are linear fits to the measurement data by using the indicated slopes.

used to tune both states into resonance. For the investigated QD, this means that the resonance point for the two states with different coupling properties can be tuned into the vicinity of the SET conductance peak.

Information about the magnetic quantum numbers and the energetic ordering can be obtained by analyzing the $B_\parallel$-dependent evolution of the SET conductance peak-spacings [DGGW+00, LIH+02, PFM+03]. The spacing between successive SET conductance peaks changes due to shell filling and spin effects [TAH+96]. Figure 5.4 shows the energy dependence of the spacings between neighboring SET conductance peaks δE_Z as a function of $B_\parallel$. For clarity, the electrostatic charging energy has been removed and the curves are vertically offset. The curves are fitted using a linear magnetic field dispersion with a slope in multiples of $g_{GaAs} = -0.44$, which is assumed to be the g-factor of an $S = 1/2$ state in the GaAs QD. The slopes of the fitted lines are added in units of μ_B to the graph. A positive or negative slope of 0.44 μ_B denotes that upon successively adding two electrons to the QD, first the total spin of the QD increases or decreases by 1/2 and then decreases or increases again by 1/2. At a constant number of electrons on the QD, a change of

slope indicates either a rearrangement of the QD orbital configuration or a change of the spin in the ground state. At $B_\parallel = 5$ T, such a rearrangement of the electrons in the QD occurs. For the $N + 1$ electron occupation, the Coulomb blockade resonance peak spacing increases with a slope of 0.88 μ_B. This behavior can not be explained by considering spin states in the QD with $S \leq 1/2$, and thus requires the occupation of orbital wave functions with $L > 0$.

The peculiar magnetic behavior of the blocking state and the asymmetric transport behavior indicate that the charge distribution of this state has a preferred spacial orientation and a high magnetic moment. Hence, the asymmetric transport gap most likely results from a sophisticated spin blockade mechanism due to a QD state with a spacial orientation in the direction of the drain reservoir.

5.2.3 Comparison of thermovoltage and nonlinear differential conductance

In order to verify that the measured asymmetric transport gap at the N+1↔N+2-transition is responsible for the observed asymmetric thermovoltage signal at $B = 13$ T, a resonant tunneling model within the Landauer picture [GBJB95] is used to compute the thermovoltage by numerical integration of the nonlinear differential conductance data. The total generalized current through the QD is given by

$$J_{tot} = \int_{-\infty}^{\infty} dE \left(\frac{\Lambda}{h} \right) [f_L(E,T) - f_R(E,T)] t(E) \tag{5.2}$$

where Λ is either the electron charge $-e$ or the energy $(E - \bar{\mu})$ carried by an electron, f is the Fermi distribution in the leads, L and R denote the left and the right reservoirs, and $t(E)$ the energy dependent transmission function. The transport coefficients L_{ij} connect charge and heat currents (I, Q) to the applied electrochemical potential or temperature differences in the following way:

$$\begin{pmatrix} I \\ Q \end{pmatrix} = \begin{pmatrix} L_{11} & L_{12} \\ L_{21} & L_{22} \end{pmatrix} \begin{pmatrix} \bar{\mu}_L/e - \bar{\mu}_R/e \\ T_L - T_R \end{pmatrix}. \tag{5.3}$$

Within this framework, the linear-response diffusion thermopower is given by

$$S = -\frac{L_{12}}{L_{11}} = -\frac{(-\frac{e}{Th}) \int_{-\infty}^{\infty} dE \ (E - \bar{\mu}) \ t(E) \ (-\frac{df}{dE})}{(\frac{e^2}{h}) \int_{-\infty}^{\infty} dE \ t(E) \ (-\frac{df}{dE})}. \tag{5.4}$$

Here, L_{12} and $L_{11} = G$ denote the thermoelectric and electric transport coefficients which describe the response of the system with respect to an applied temperature difference and bias voltage, respectively. For the calculation, it is assumed that $t(E) = \frac{dG}{dE}$ and additionally one accounts for thermal broadening by a constant factor.[2] For the numerical

---

[2]The constant factor is 1/1.76. It only enters into the amplitude of the calculated coefficients and L_{11} and L_{12}, but cancels out in the calculation of the thermopower.
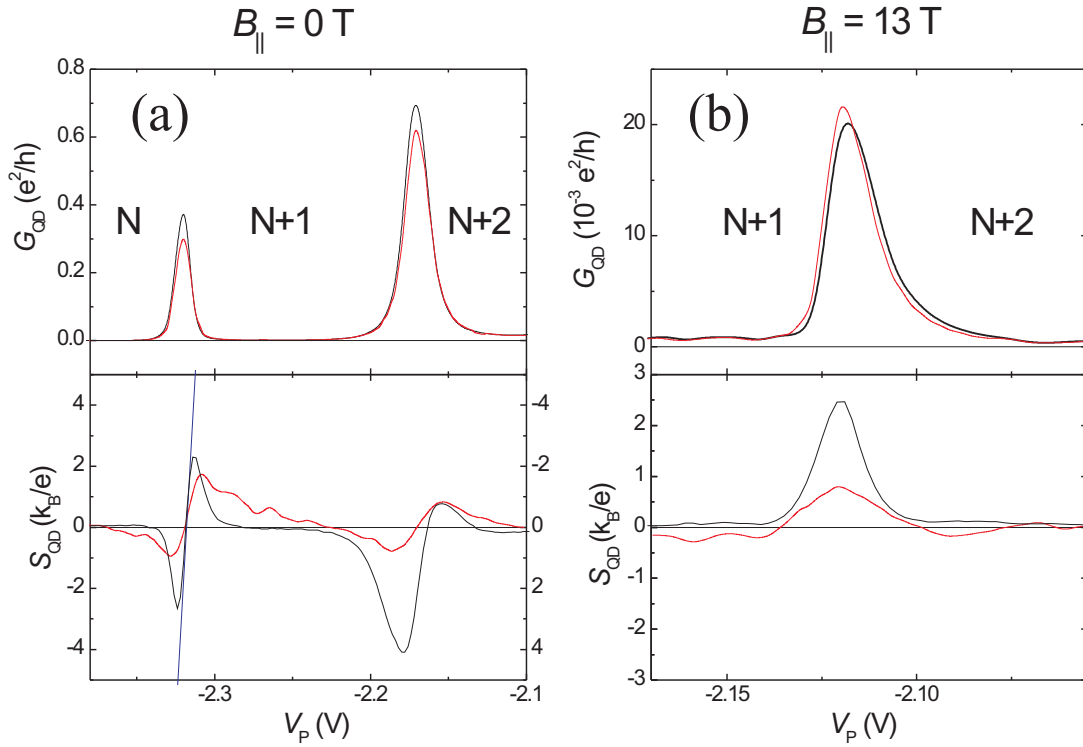
Fig. 5.5: Conductance G (upper panel) and thermopower S (lower panel) at $B_\parallel = 0$ T [(a)] and $B_\parallel = 13$ T [(b)]. Black lines indicate experimental data; the red line shows the results from the numerical integration of the nonlinear differential conductance using Eq. (5.4) for $T = 150$ mK. The blue line indicates the sequential tunneling limit for the thermopower of the left SET resonance for $T = 80$ mK and $E_C = 2.2$ meV.

integration of dG/dE, it has to be considered that the source and the drain contact couple capacitively to the QD and the fact that the drain contact is used as the hot reservoir for the measurement of the thermovoltage. The thermovoltage as a function of plunger gate voltage is obtained by using subsets of measurement data for $t(E)$, which have been extracted from dG/dV_{DS} along parallel lines to the dashed line shown in Fig. 5.3(b).

Figures 5.5(a) and (b) show the results of the numerical integration of dI/dV_{DS} according to Eq. (5.4) for $B_\parallel = 0$ T and $B_\parallel = 13$ T. Here, an increased average temperature of $T = 150$ mK has been used for the numerical calculations, in order to average over a set of data points and avoid numerical artifacts. For direct comparison, the measured zero bias conductance and the corresponding thermopower have been added. For the experimental data, the temperature of the electron gas $T = 80$ mK and the temperature difference $\Delta T = 30$ mK have been obtained independently by analyzing the temperature dependence of magneto-conductance fluctuations in the electron heating channel (cf. Chap. 3.3.2.3). In order to account for the temperature dependence of the thermopower, the theoretical results have been scaled according to the sequential tunneling theory, i.e. $S(T) \times T = -\langle E \rangle / 2e = S_{80 \text{ mK}} \times 80$ mK, which increases the amplitude roughly by a

factor of 2. This procedure is valid at least in the close vicinity of the SET conductance peaks, where sequential tunneling contributions to the thermopower dominate (cf. Chap. 4). Here, $\langle E \rangle$ is the temperature independent effective energy gap between the QD state and the Fermi level.

The curves presented in Figs. 5.5(a) and (b) show good agreement between experimental and numerically deduced data. The line shape and the approximate amplitude agree well with the measurement data. Differences between experimental and calculated thermopower are expected to result from neglecting any interplay between the thermoelectric contributions of sequential tunneling and cotunneling within the theoretical treatment. The agreement between the numerical analysis and the measurement data confirms that the calculations using the resonant tunneling model are applicable to the thermoelectric transport in QDs. Additionally, it confirms that the asymmetric transport gap at the N+1↔N+2-transition is responsible for the observed asymmetric thermovoltage signal at $B_\parallel = 13$ T.

Furthermore, theoretical model calculations show that the observed behavior can be explained by a two state model system. Figure 5.6 presents the results of the numerical calculation of the transport coefficients using Eq. 5.2 and an idealized transmission function

$$t(E) = \lambda(E) \times \sigma(E,T) = A \frac{(h\Gamma/2)^2}{(h\Gamma/2)^2 + (E)^2} \times f(E - \delta E_Z, T). \tag{5.5}$$

Here, $\lambda(E)$ represents a single QD resonance, while $\sigma(E,T)$ accounts for the thermal occupation of a blocking state which depends on the Zeeman energy separation δE_Z between the transmitting and the blocking state. For the calculations the SET conductance peak at $V_P = -2.17$ V, ($B_\parallel = 0$ T) has been fitted; this gives $A = 0.79$ and $h\Gamma = 0.2$ meV. In order to account for co-tunneling contributions via additional excited states, a constant amount of $G_{cot} = 0.001\ e^2/h$ has been added to the conductance. The amplitude of G_{cot} corresponds to the experimentally observed minimum conductance between two SET conductance peaks. Furthermore, the experimentally determined electron temperature $T = 80$ mK and temperature difference $\Delta T = 30$ mK have been used for all calculations.
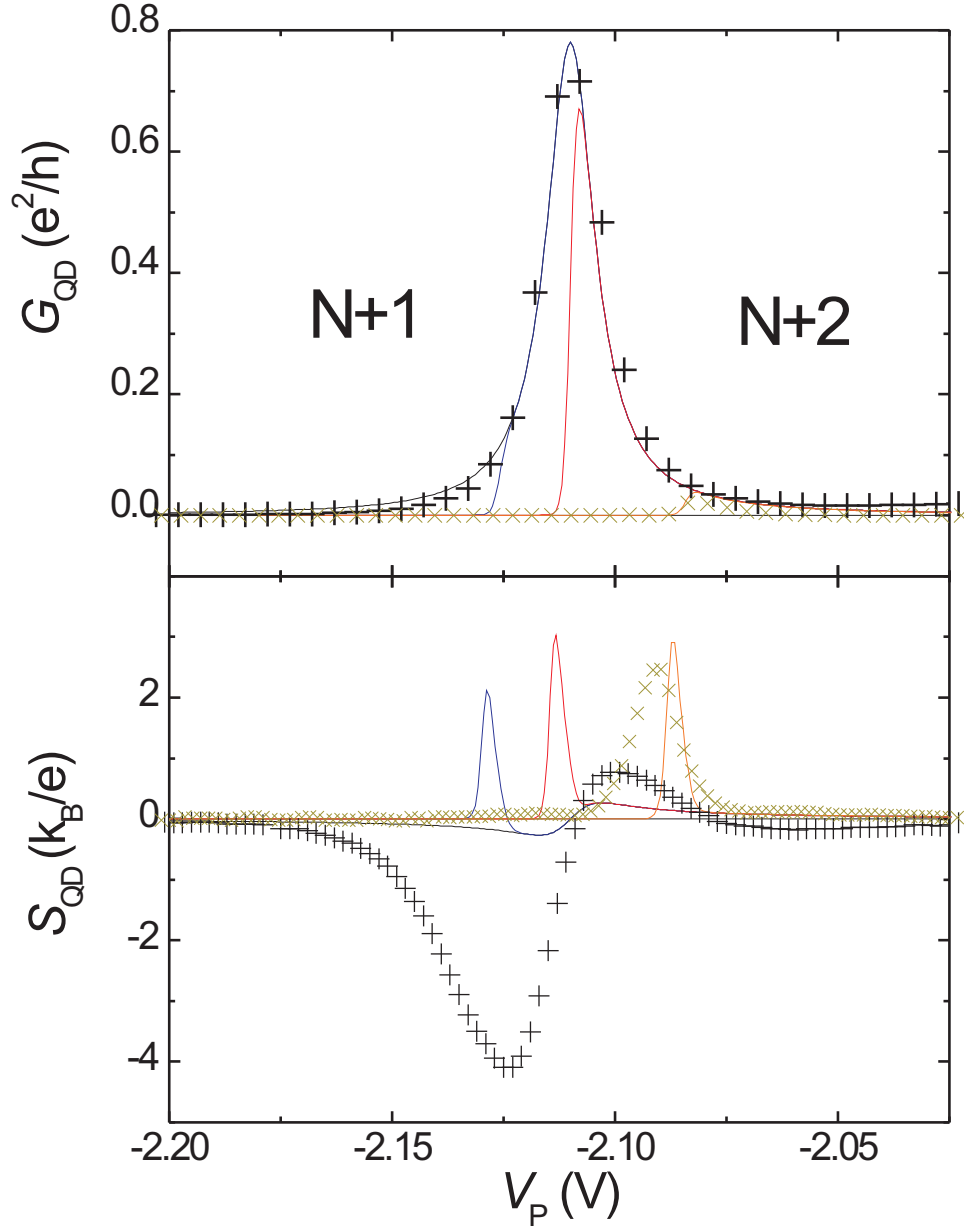
Fig. 5.6: Conductance G (upper panel) and thermopower S (lower panel) obtained from a numerical simulation using Eq. (5.2) and Eq. (5.5) for various Zeeman energies E_Z of the blocking state: without blocking (black), $\delta E_Z = -250$ μeV (blue), 0 μeV (red), 400 μeV (orange). Other parameters used for the calculation: $E_C/eV_P = 0.0154$, $h\Gamma = 200$ μeV, $T = 150$ mK, and $\Delta T = 30$ mK. For comparison, the experimental data points for $B_\parallel = 0$ and 13 T have been added to the graphs as black and dark yellow crosses, respectively. The experimental data have been corrected for shifts in the potential of the QD.

Starting from a situation where the blocking state is energetically above the transmitting state ($\delta E_Z = -250 \, \mu e$V), the upper panel of Fig. 5.6 shows that the SET conductance peak becomes more and more asymmetric with increasing δE_Z. For $\delta E_Z = 0$, the SET conductance peak shows a sharp cutoff edge at its center position. The calculated conductance for $\delta E_Z = 400 \, \mu e$V closely resembles the measured $G(V_P)$ at $B_\parallel = 13$ T. This value corresponds to the situation where the blocking state is energetically below the transmitting state. The corresponding thermopower S changes from a point symmetric shape to a single peak structure as the blocking state is shifted through the resonance. Again, good agreement with the experiment is achieved for all values of $\delta E_Z = 0$. The observed deviations most probably result from neglecting additional excited states which may broaden the overall line shape in the experimental curves.

5.2.4   Thermal rectification

Although electric rectification is a hint for similar thermal effects, it seems noteworthy that within the framework of this model for the transmission function [Eq. (5.5)], the QD acts as a electronic *thermal rectifier*, which is the thermal analogue to the electrical diode [Pey06, COMZ06]. The reversal of the temperature difference across the QD results in a difference in the heat flow through the QD. This is because the line shape of the transmission function depends on the temperature of the reservoir that determines the occupation of the blocking state. The rectifying behavior with respect to the thermal transport is shown in Figs. 5.7(a) and (b), where the parameters of the measurement ($T = 80$ mK, $\delta T = 30$ mK) have been used for the calculation of the experimentally measurable thermal conductance $\kappa = L_{22} - (L_{12}L_{21}/L_{11})$. The efficiency of rectification, ($\Delta \kappa / \kappa$), reaches 10.5 % at the given temperatures. The effect increases with increasing temperature difference. However, it has to be considered that very high temperature differences lead to increased thermally activated transport via other excited states in a real QD structure. These effects modify the transport properties considerably, and are not included in the present model calculations. Nevertheless, the perspective of a more sophisticated device geometry (e.g. in multiple QDs or QD molecules) may lead to an improved performance.

Finally, it should be mentioned that these investigations show that QDs are capable of intrinsically uniting electrical and thermal information processing in one device.

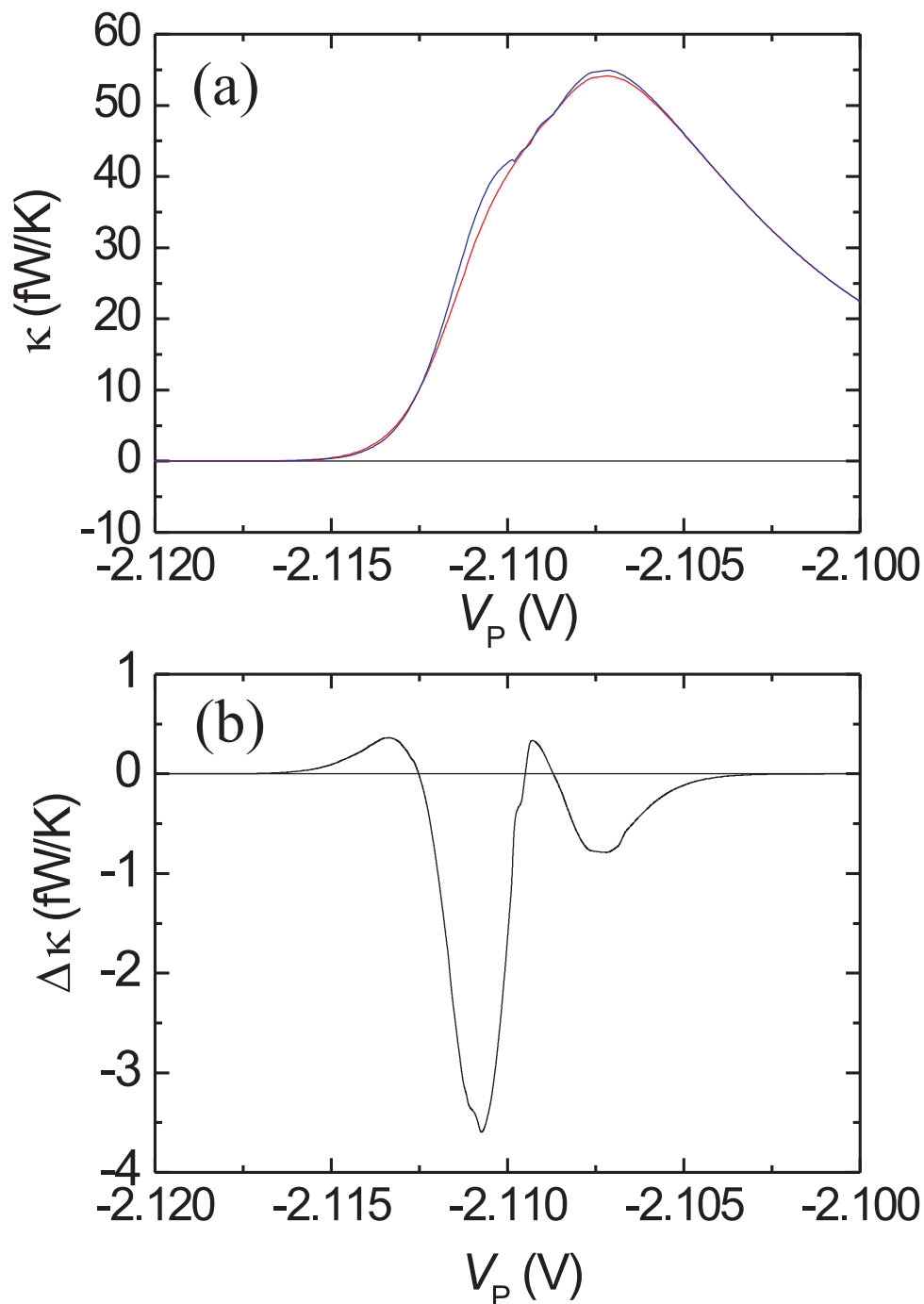**Fig. 5.7:** (a) Thermal conductance $\kappa = L_{22} - (L_{12}L_{21}/L_{11})$ calculated for $T = 80$ mK, $\delta E_Z = 0$, and $\Delta T = 30$ mK. The red line corresponds to the case of a strong coupling of the blocking state to the hot reservoir. The blue line indicates a strong coupling of the blocking state to the cold reservoir. (b) Difference in the heat conductance ΔL_{22} due to the reversed temperature difference.

5.3 Asymmetric thermoelectric transport induced by excited states

In the previous section, the thermoelectric signal in the regime of asymmetric first order transport was discussed. Since the asymmetric coupling of the QD states is not restricted to sequential tunneling via the ground state transition, the thermoelectric signal should also be sensitive to asymmetries in the sequential and co-tunneling transport via the excited states of the QD. In the following, the signatures of the various possible situations and QD configurations will be explained by means of an exemplary measurement.

Figure 5.8 presents a color scale plot of the nonlinear differential conductance against the plunger gate voltage V_P at $T_L = 40$ mK together with the corresponding zero-bias conductance line and traces of the thermovoltage at high and low temperatures. The plot shows three successive Coulomb blockade diamonds, which are labelled by N, $N+1$, and $N+2$ respectively. The QD is the same as the one discussed in Chap. 4, where the change from a sawtooth line shape for high temperatures to a sawtooth shape interposed periodically by a zero thermovoltage for low temperatures in the Coulomb blockade regime [see third and fourth panels of Fig. 5.8]. This behavior has been ascribed to the increasing dominance of the cotunneling transport at very low temperatures.

In the dI/dV_{DS}-measurement, differences between the charge transport from drain to source and the transport from source to drain are observable. This indicates an asymmetric coupling of the QD to the leads [WHvKP93]. The finite-bias differential conductance lines for positive V_{DS} differ in height from the lines observed for negative V_{DS}. Most obviously, this can be seen for the N- and $N + 1$-electron QD. The single-electron-tunneling (SET) from source to drain via the ground state transition ($(n,0) \leftrightarrow (n+1,0)$) is partially suppressed for positive V_{DS}. This is evident in the upper right boundary of the Coulomb blockade diamonds in the first panel of Fig. 5.8. For negative V_{DS}, the corresponding SET transition from drain to source via the same ground states is clearly visible [see the lower right boundary of the Coulomb blockade diamonds].

Furthermore, strong negative differential conductance is observable in the SET regime for excited states of the configuration $\bar{\mu}_{n,i;n+1,0}$ with $i > 0$. Again, this behavior is less pronounced for negative V_{DS}. According to the subsequent filling of the single particle states of the QD with increasing number of electrons N with increasing V_P, these lines of negative differential conductance (excited states) move closer to the ground state SET transition. Corresponding to the discussion in the previous section, the occurrence of regions with strong negative differential conductance in the V_{DS}-V_P plane is the signature of various transport blocking mechanisms [WHK95, Tew04]. In connection with the negative differential conductance, also a suppression of the ground state transitions can be observed again for finite $|V_{DS}| > 0$.

These distinct features in the finite-bias differential conductance can be compared to pronounced features in the fine structure of the thermovoltage line shape, indicated by the dashed vertical lines in Fig. 5.8. For direct comparison, it is necessary to keep in
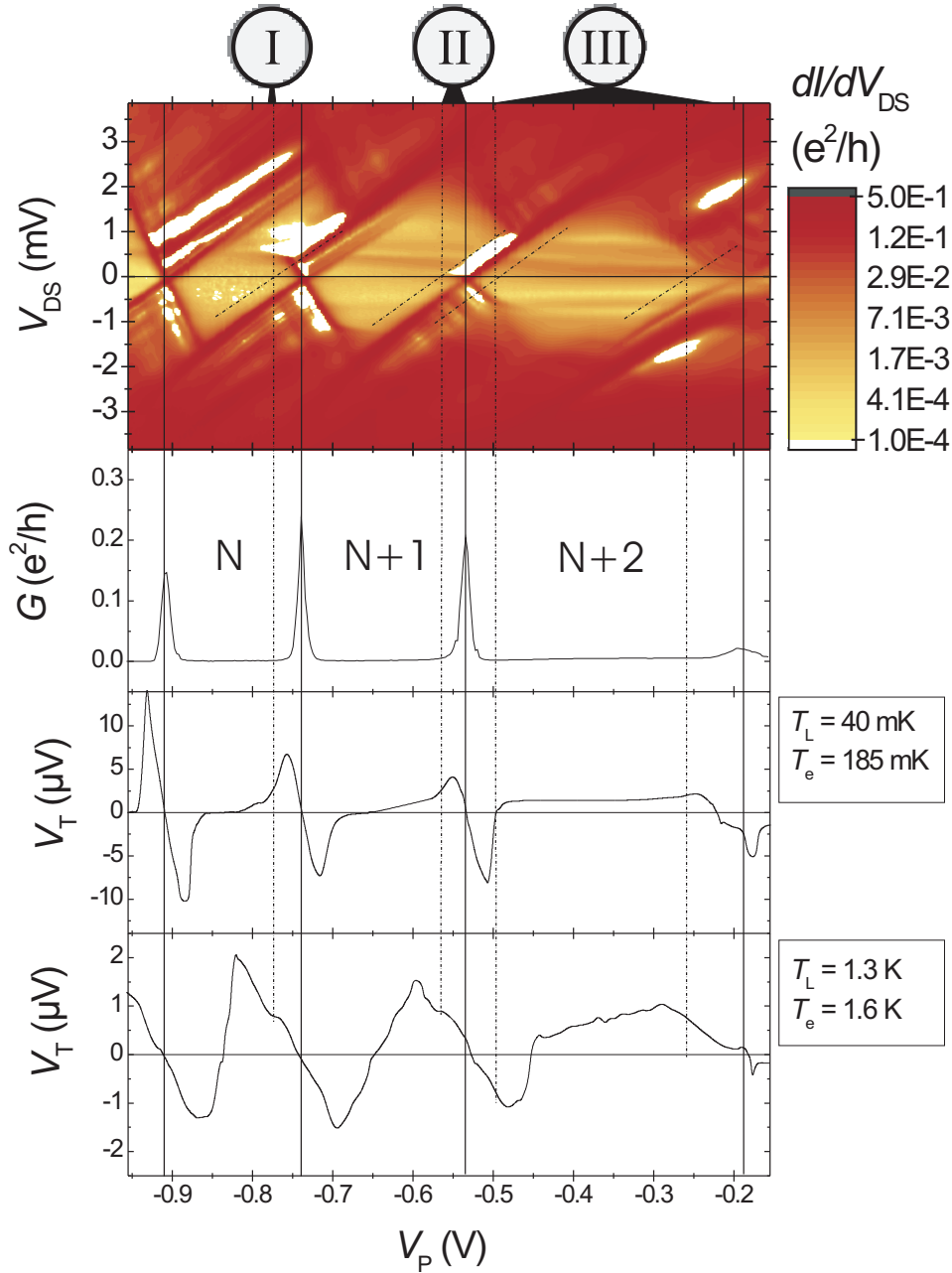
Fig. 5.8: Logarithmic color-scale plot of the nonlinear differential conductance dI/dV_{DS} against plunger gate voltage V_P at $T_L = 40$ mK (first panel) together with corresponding zero bias conductance G (second panel) and corresponding thermovoltage at low (third panel) and high (fourth panel) temperatures. White areas mark regions of a negative differential conductance. Solid vertical lines indicate the gate voltage positions of the zero-bias SET conductance peaks. Vertical dashed lines mark the points of special interest (see Roman numbers from I to III). These are discussed in the text and in Figs. 5.10, 5.9 and 5.11. Diagonal dashed lines indicate the direction in the V_P-V_{DS}-plane which has to be considered for the comparison of the nonlinear differential conductance with the thermovoltage measurement data.

mind that the drain contact of the conductance measurement connects to the cold side in the thermovoltage measurement. Thus, a high differential conductance at positive source-drain voltage translates into a positive energy gap in the thermoelectric transport. Taking into account the capacitive coupling of source and drain contacts to the QD, the thermovoltage has to be compared to the excitation spectrum along the diagonal dashed lines in the first panel of Fig. 5.8.

Note that the $N + 2 \leftrightarrow N + 3$ SET conductance peak is strongly suppressed [see second panel of Fig. 5.8]. Here, the single particle state, which is responsible for the negative differential conductance at more negative plunger gate voltages, is the ground state of the $N + 3$ electron system. A finite V_{DS} is needed to accomplish transport via excited states of the system. The corresponding thermovoltage curve shows a non trivial behavior at low temperatures, which is a mixture of strong cotunneling away from the SET conductance peak, and mainly thermally activated tunneling at the center of the SET conductance peak. The following discussion does not cover this situation in detail, since it is rather similar to the thermoelectric signature of the ground state transition via an asymmetrically coupled blocking state, which has been discussed in the previous section. The main differences to the previous case are the strength of the asymmetric coupling and the ratio of positive and negative thermovoltage contributions via excited states. Here, negative contributions prevail at very low temperatures, while positive contributions outweigh in the temperature range above $T_L = 1$ K.

The following subsections discuss the fine structure in the thermovoltage measurements by analyzing the excited state spectra of the QD. According to the Roman numeral labelling given in Fig. 5.8, first the effects due to an enhanced SET transport via an excited state are discussed (I). Then, the signature of a reduced SET transport due to a blocking excited state is discussed (II). The last subsection focuses on thermoelectric effects due to cotunneling, in the case of an asymmetric coupling of the excited states (gate voltage range III).

5.3.1   Fine structure of first order transport via excited states

Figure 5.9 shows a color-scale plot of dI/dV_{DS} and the corresponding thermovoltage in the vicinity of the $N \leftrightarrow N+1$ SET conductance peak. A diagonal dotted line has been added to the graph in order to extrapolate the energetic position of an excited state to the zero-bias axis. The excited state intersects the Coulomb blockade diamond at $V_{DS} = 0.5$ mV and $V_P = -0.76$ V. The extrapolated line intersects the zero-bias axis at $V_P = -0.78$ V. Here, the potential of the QD is raised to the point, where the Fermi levels of source and drain reservoirs are equal to the electro-chemical potential of the corresponding excited state resonance $\bar{\mu}_{N,2;N+1,0}$.

The thermovoltage line shape taken at $T_L = 1.3$ K shows a small wiggle at the corresponding plunger gate voltage. These kinds of wiggles also show up in the model calculations of the sequential thermopower contributions, which have been presented in
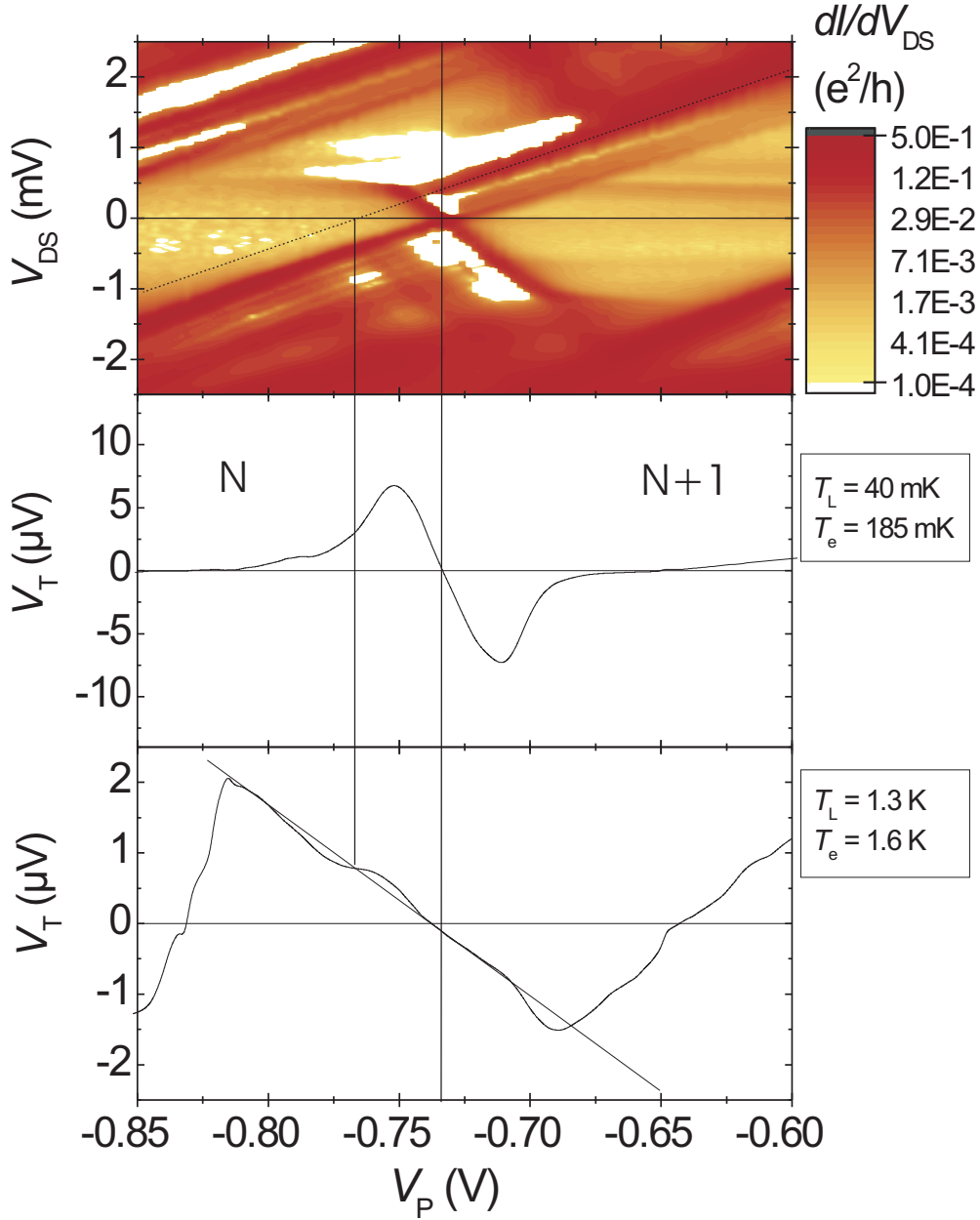
Fig. 5.9: Logarithmic color-scale plot of the nonlinear differential conductance $dI/dV_{DS}(V_P, V_{DS})$ (upper panel) together with corresponding thermovoltage at low (middle panel) and high (lower panel) temperatures. The solid vertical line at $V_P = -0.73$ V indicates the gate voltage position of the zero-bias SET conductance peak. The diagonal dashed line indicates the direction in the V_P-V_{DS}-plane which has to be considered in the comparison of the nonlinear differential conductance with the thermovoltage measurement data, and extrapolates the enhanced tunneling via one excited state to the zero-bias line at $V_P = -0.78$ V.

Chap. 4. This kind of fine structure has been observed in previous experimental studies of the thermopower of QDs [DSB$^+$97]. However, a direct one-to-one comparison of contributions due to single excited states has not been treated. The fine structure is determined by the level spacing, and is only equally spaced if the levels are equally spaced. This is usually not the case in few-electron QDs, and the fine structure on top of the positive part of the thermovoltage sawtooth does not map to that on top of the negative part.

At $T_L = 40$ mK, the thermovoltage is already dominated by cotunneling processes in the corresponding gate voltage range. However, the contribution of the excited state to the thermoelectric transport can still be seen as the beginning of a shoulder toward the more negative V_P.

5.3.2 Thermoelectric signature of blocked excited states

Figure 5.10 shows a color scale plot of $dI/dV_{DS}(V_P, V_{DS})$ in the vicinity of the $N + 1 \leftrightarrow N + 2$ SET conductance peak. For positive V_{DS} and -0.55 V $< V_P < -0.47$ V, strong negative differential conductance is measured. Furthermore, the ground state transition is suppressed for $V_P < -0.55$ V and $V_{DS} > 0$. This behavior indicates that the occupation of an excited state of the $N + 1$ electron system blocks further transport from source to drain for $V_P \lesssim -0.54$ V.

The low temperature ($T_L = 40$ mK) thermoelectric transport shows a significantly reduced positive thermovoltage amplitude compared to the negative thermovoltage amplitude at more positive plunger gate voltages ($V_P \sim -0.51$ V). However, the high temperature ($T_L = 1.3$ K) line shape of the thermovoltage is enhanced for $V_T = 0.34$ μV in the plunger gate voltage range where the electric transport is characterized by a strong negative differential conductance for $V_{DS} > 0$.

The different low and high temperature behaviors of the thermoelectric contribution of the blocking state can be explained by the interplay between sequential and cotunneling transport. In general, it has to be considered that the blocking state itself contributes only weakly to the thermoelectric transport. For the high temperature thermoelectric transport, which is dominated by sequential tunneling, this means that the electrons which cross the QD have to tunnel via excited states at a higher energy. This energy is provided by the high temperature in the leads, and correspondingly the average energy of tunneling charge carriers, which is proportional to the thermovoltage, is increased.

At low temperatures, the thermal energy is not sufficient to overcome the additional energy gap and sequential transport is suppressed. The ratio of thermally activated transport to cotunneling transport is shifted in favor of the cotunneling transport events. Since the average energy of cotunneling charges is only of the order of $k_B T$, a reduced thermovoltage signal amplitude results.

Because the blocking state seems to have less influence on the electron transport from drain to source, the additional energy gap also has little influence on the negative thermovoltage signal amplitude for $V_P > -0.54$ V.

Fig. 5.10: Logarithmic color-scale plot of the nonlinear differential conductance $dI/dV_{\mathrm{DS}}(V_{\mathrm{P}}, V_{\mathrm{DS}})$ (upper panel) together with corresponding thermovoltage at low (middle panel) and high (lower panel) temperatures. The solid vertical line at $V_{\mathrm{P}} = -0.53$ V indicates the gate voltage position of the zero-bias SET conductance peak. The diagonal dashed lines define the area limits in the V_{P}-V_{DS} plane where strong negative differential conductance contributes to the thermoelectric transport.

This example shows that the asymmetric coupling of excited states can have a strong influence on the low temperature thermoelectric transport. In this case, remarkably, the "fine structure correction" due to the effect of one excited state is about 30% of the total signal. This may be taken as an indication of the fact that the low temperature thermoelectric behavior of many material compositions is hardly predictable.

5.3.3   Asymmetric cotunneling

While the examples studied in the previous sections cover the interplay between sequential and cotunneling of asymmetrically coupled states, the thermoelectric transport due to pure cotunneling in the case of asymmetrically coupled states is discussed in this part.

The color scale plot of Figure 5.11 shows the nonlinear differential conductance for the $N + 2$ Coulomb blockade diamond of Fig. 5.8 in detail. In the regime of Coulomb blockade, small peaks of enhanced differential conductance $dI/dV_{\mathrm{DS}}(V_{\mathrm{DS}})|_{V_{\mathrm{P}}=\mathrm{const.}}$ are visible as faint lines parallel to the zero-bias line. These are asymmetrically distributed in positive and negative V_{DS} directions. The lines end at the intersections of the adjacent SET regimes, where the SET differential conductance lines of the excited states intersect the ground state transition. This contribution is visible in all of the Coulomb blockade diamonds shown in Fig. 5.8. Their amplitude, however, decreases with increasing V_{P}, which indicates a dependence on the tunneling barrier height.

The low temperature thermovoltage ($T_{\mathrm{L}} = 40$ mK) shows a plateau-like structure from $V_{\mathrm{P}} = -0.47$ V to $V_{\mathrm{P}} = -0.47$ V instead of the expected zero thermovoltage between two SET conductance peaks. The high temperature thermovoltage ($T_{\mathrm{L}} = 1.3$ K) shows a similar but less pronounced plateau structure in the same plunger gate voltage range.

The finite differential conductance in the Coulomb blockade regime, which sets in at $|V_{\mathrm{DS}}| > 0$, is characteristic for inelastic cotunneling. Two states and electrons participate in this incoherent second order transport process. First, an electron tunnels from one lead to the QD, and in the second step, an electron which occupies a different state tunnels from the QD to the second lead. In order to obey the conservation of energy law, the energy difference between the two participating QD states δE_{in} has to be provided by the energy difference of the electrons in the leads prior to and after the transport event. As discussed in more detail in Chap. 1, this effect depends on the coupling of the QD to the leads and the level spacing. In the Coulomb blockade regime, inelastic cotunneling is independent of the potential of the QD. And due to the discrete level spectrum of the QD, it sets in abruptly at $|eV_{\mathrm{DS}}| = \delta E_{in} \gg k_B T$.
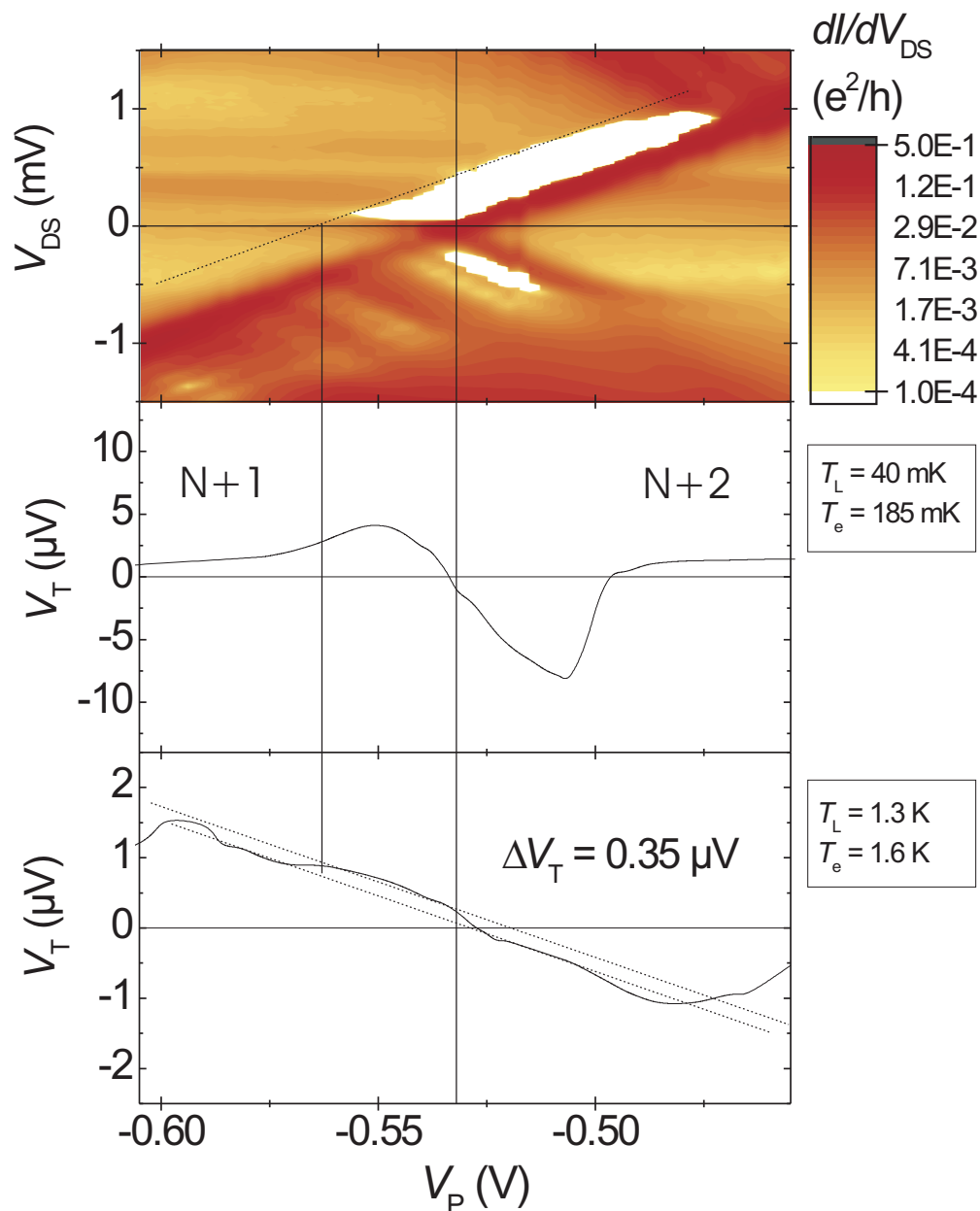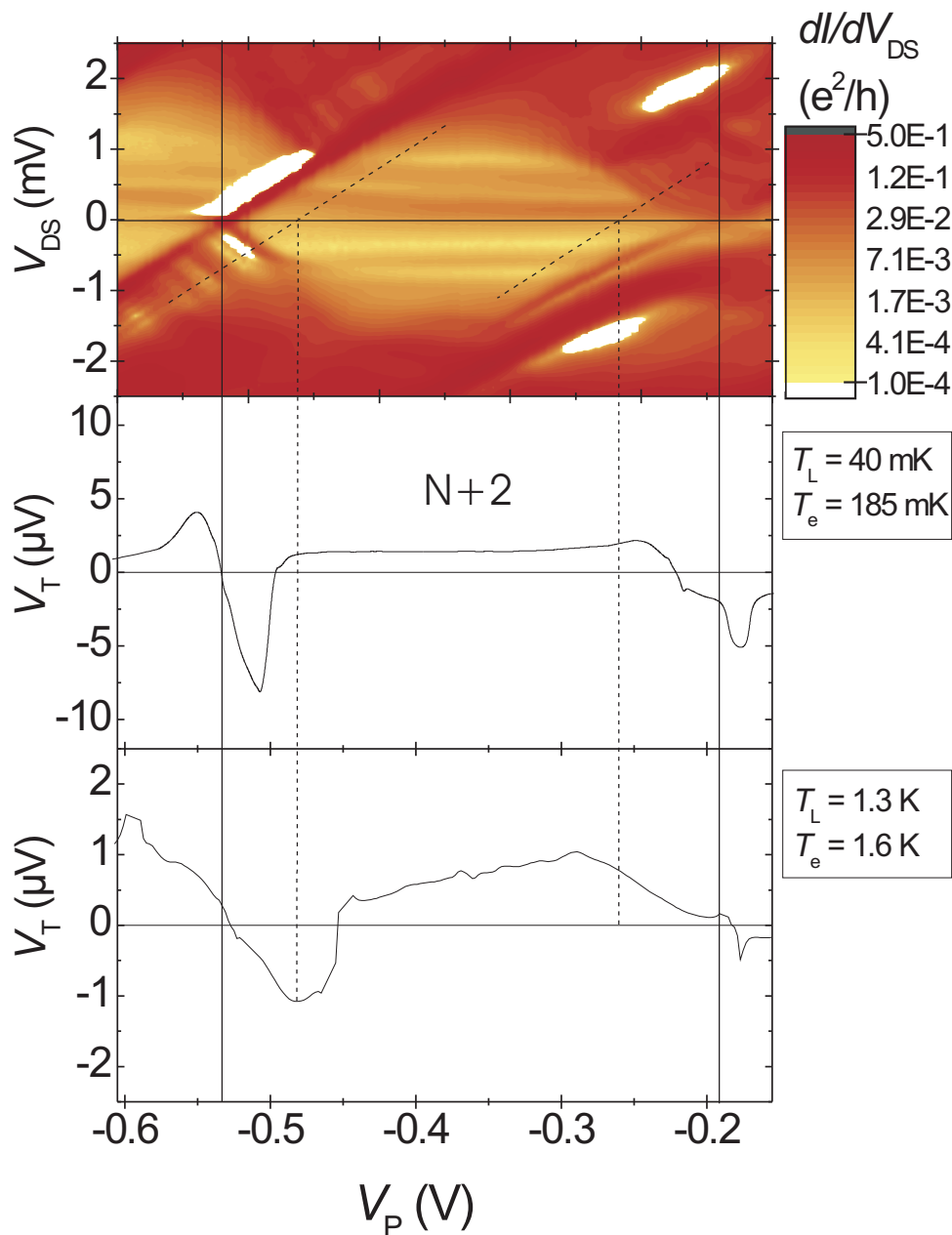
Fig. 5.11: Logarithmic color-scale plot of the nonlinear differential conductance $dI/dV_{DS}(V_P, V_{DS})$ (upper panel) together with corresponding thermovoltage at low (middle panel) and high (lower panel) temperatures. The solid vertical lines at V_P = -0.19 and -0.53 V indicate the gate voltage positions of the zero-bias SET conductance peak. The vertical dashed lines mark the beginning and the end of the low temperature thermovoltage plateau between the SET conductance peaks.

In the same gate voltage range, the sequential tunneling is exponentially suppressed and does not contribute to the charge transport at very low temperatures. The smallest energy gap, which mainly determines the signal amplitude of the low temperature thermovoltage, is determined by the level spacing of the QD.[3] In the case of a direction independent transmission through the QD, positive and negative contributions cancel each other, and a zero thermovoltage results. However, in the present case, the strongly asymmetric transport behavior of the given QD states favor the positive contributions to the thermovoltage. At very low temperatures, the thermovoltage signal is clearly independent of V_P [see lower panel of Fig. 5.11]. This behavior is not preserved for high temperatures, since part of the transport is again thermally activated. The remaining strong cotunneling reduces the back-formation of the full sawtooth line shape.

This measurement shows that cotunneling transport strongly contributes to the thermoelectric transport. The cotunneling contributions to the thermoelectric transport are directly visible by means of a QD state, which shows a strong unidirectional transport behavior. In the QD system under investigation, the asymmetric dynamics lead to thermovoltage signals that are in a certain range independent of the QD potential.

---

[3]At very low temperatures, the thermoelectric contribution due to inelastic cotunneling is determined by the energy difference between the ground state and first excited state.

Chapter 6

Thermoelectric transport in the spin-correlated regime

Since the early 1930s it has been known that the low temperature resistance of certain bulk metals first decreases, then goes through a minimum at a certain temperature, and then increases again for decreasing temperature, if the impurities in the material possess a magnetic moment. This effect has become known as the Kondo-effect, named after the Japanese theoretician Jun Kondo and the temperature of minimum resistance as the Kondo temperature. Jun Kondo developed a theoretical model which describes the observed effect by considering a spin scattering mechanism of the free electrons at the localized magnetic moments of the impurities [Kon64]. The Kondo effect due to magnetic impurity scattering in metals is a well known and a widely studied phenomenon [Hew93]. This effect has received much renewed attention after it was first predicted [NL88, GR88, MWL93, WM94, ISS98] and later on demonstrated [GGSAM+98, COK98, SWEK98] that the Kondo effect can significantly influence transport through semiconductor QDs. The problem of transmission through a QD is similar to that of transitions between channels in a multi-channel scattering problem. Under certain model assumptions, the transition rate is proportional to the total scattering cross section. Therefore, the two problems, namely the calculation of the tunneling conductance G and the evaluation of the impurity contribution to the resistivity of a bulk metal are equivalent [PG01, GR88, NL88]. In a gate defined QD, the electronic states can be controlled externally. This enables experimenters to address many questions concerning Kondo physics that were previously inaccessible [vdWDFF+00]. Still unexplored are the thermoelectric properties of a QD in the presence of Kondo correlations. Such thermoelectric properties can often yield valuable additional information concerning transport phenomena. In a Kondo correlated QD, the interaction between the localized magnetic moment of the dot and the free electrons in the adjacent reservoirs leads to a state which is energetically linked to the Fermi energy. The correlated state is destroyed in non-equilibrium situations, e.g. for large bias voltages between the lead reservoirs. In the previous chapters, it has been shown that the thermopower S is a sensitive tool for measuring the weighted spectral density
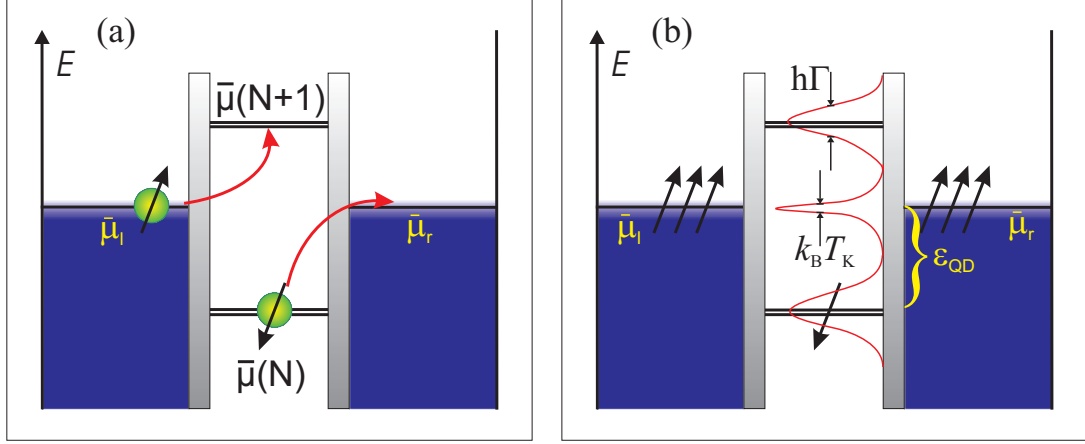
Fig. 6.1: Schematic energy diagram of a QD in the presence of (Kondo) spin-correlations. (a) The electron on the QD occupies a (spin) degenerate energy state. Via an intermediate virtual excited state, the electron from the QD is replaced by the scattered electron from the reservoir, leading to a spin flip on the QD. (b) Density of states in the QD. Due to the spin correlations an additional resonance develops at the position of the Fermi levels of the reservoirs in the Coulomb blockade energy gap.

of states in the close vicinity of the Fermi energy E_F, while leaving the QD at almost zero-bias at the same time. Thus, S is an almost ideal tool for studying the physics of the correlated state.

The next section begins with a brief summary of the Kondo-effect in QDs. Then, the results of thermopower measurements on a lateral QD in a magnetic field perpendicular to the plane of the 2DEG are presented. As a next step, the magnetic field dependent and nonlinear conductance measurements are used to identify the presence of Kondo spin-correlations. The subsequent comparison between the transport regimes of strong and weak coupling of the QD to the leads shows a clear breakdown of symmetry in the electron-hole transport through the QD in the presence of Kondo spin-correlations. This observation is accompanied by qualitative deviations from the semiclassical Mott relation [see Chap. 2.26]. The chapter ends with the discussion of the experimental findings with respect to the kinetic and spin-entropy contribution to the thermoelectric transport.

6.1   Kondo-effect in quantum dots

The Kondo effect in QDs is usually described by using the Anderson impurity model. This model was developed by P.W. Anderson in 1961 [And61]. The model enables the calculation of the transport effects in metals in the presence of magnetic impurities to be done. The schematic energy diagram for the Anderson impurity model is analogous to the schematic energy diagram of a spin degenerate QD in the Coulomb blockade.

Both systems, i.e. the magnetic impurity in metals and the QD, are characterized by the electrostatic Coulomb repulsion energy E_C which is necessary to add an electron to the impurity or to the QD. Further parameters for characterizing the system are the energy level of the spin-degenerate ground state of the impurity or QD, and the constant Γ which describes the tunnel coupling to the reservoirs.

If the coupling of the QD states to the leads is strong enough, higher order tunneling processes via virtual intermediate states have to be incorporated into the transport models, as already discussed. Likewise, elastic and inelastic cotunneling processes in the absence of spin-magnetic moments have already been treated in the previous chapters [Chaps. 4 and 5]. When spin is incorporated, the coupling due to the magnetic exchange interaction modifies the tunneling [cf. Fig. 6.1]. The Kondo effect is a result of this interaction between the localized magnetic moment of the QD and the spin of the electrons in the surrounding electron gas. Successive virtual spin-flip scattering processes effectively screen the local spin of the QD and a quasi bound state is formed by the electrons in the leads interacting with the QD electrons. In the very low temperature limit, the magnetic moment of the QD is completely screened and the spin-correlated state forms a spin-singlet. The stability of this quasi-bound state can be characterized by the energy bandwidth of its spectral density, which is proportional to the Kondo-temperature T_K. According to Ref. [Hal78], the Kondo-temperature T_K for the Anderson-impurity model is given by the analytical expression:

$$k_B T_K = \frac{1}{2}\sqrt{E_C \hbar \Gamma} \exp\left(\frac{\pi \varepsilon_0 (E_C + \varepsilon_0)}{\hbar \Gamma E_C}\right). \tag{6.1}$$

In the measurements of the nonlinear differential conductance of a QD in the CB regime, the Kondo effect expresses itself by a resonance at zero bias between successive SET conductance peaks. In non-equilibrium situations such as in the presence of magnetic fields, which introduce a Zeeman splitting of the spin states in the QD, or in the presence of bias voltages between the leads, the Kondo resonance splits apart and decreases in amplitude [COK98, SWEK98, DFHvdW+02]. This behavior can be explained by the following facts: (a) the spin-correlated state is linked to the electrons close to the Fermi-surface and (b) the virtual spin-flip scattering processes have to be energy conserving.

It should be noted here that other more complex situations can lead to spin- or Kondo-correlated states. These are, among others, the orbital Kondo effect and the Kondo effect at the transition from spin-singlet and spin-triplet states of the QD [JHKvdZ+05, vdWDFE+02]. These will not be discussed here further.

For a more precise and quantitative description of the Kondo effect, reference is made to the large number of literature available on this topic, for example, Ref. [Hew93]. In addition, summaries of the Kondo effect in QDs can be found in Refs. [Pus06, GP03].
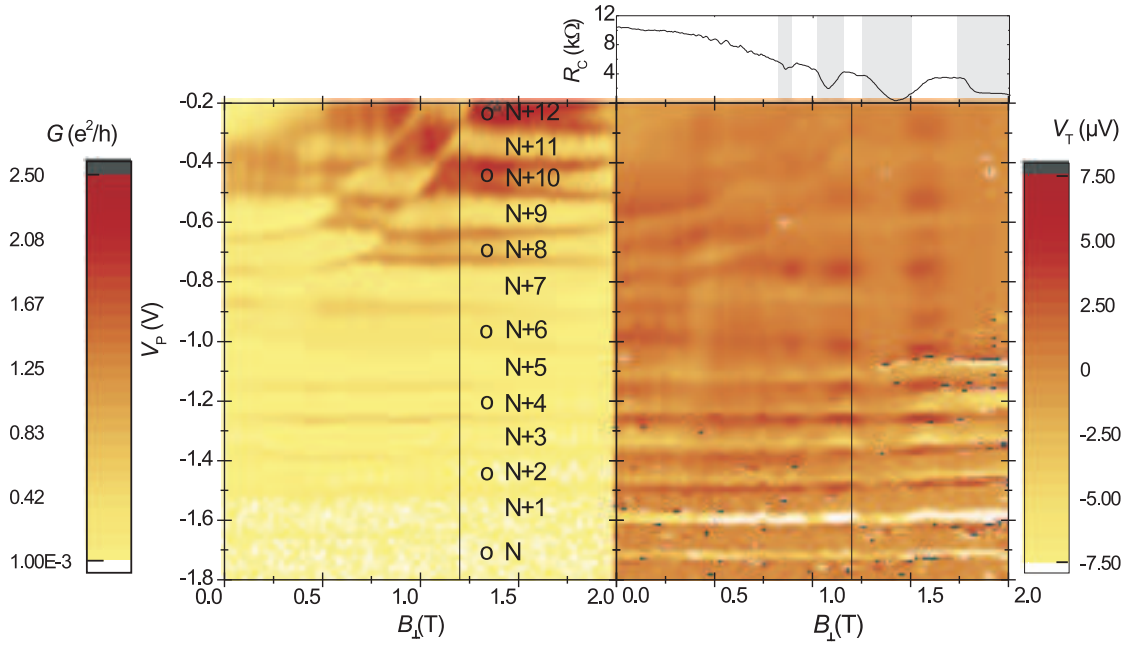
Fig. 6.2: Color-scale plot of the linear conductance G (left panel) and the thermovoltage V_T (right panel) as function of magnetic field $B_\perp$ and plunger gate voltage V_P. Between the SET conductance peaks, small circles mark odd number of electrons on the QD. The longitudinal resistance of the current heating channel R_C as a function of the magnetic field has been added in an additional panel above the thermovoltage color scale plot. Grey shaded regions indicate magnetic field ranges of Shubnikov-de Haas oscillation minima in the panel of the heating channel resistance.

Fig. 6.3: SET conductance peak positions as function of magnetic field. The positions of the SET conductance peaks have been individually offset for clarity. The corresponding voltage shift is given in the legend. The legend denotes the SET conductance peaks according to the transition between n and $n + 1$ electrons on the QD [cf. Fig. 6.2].
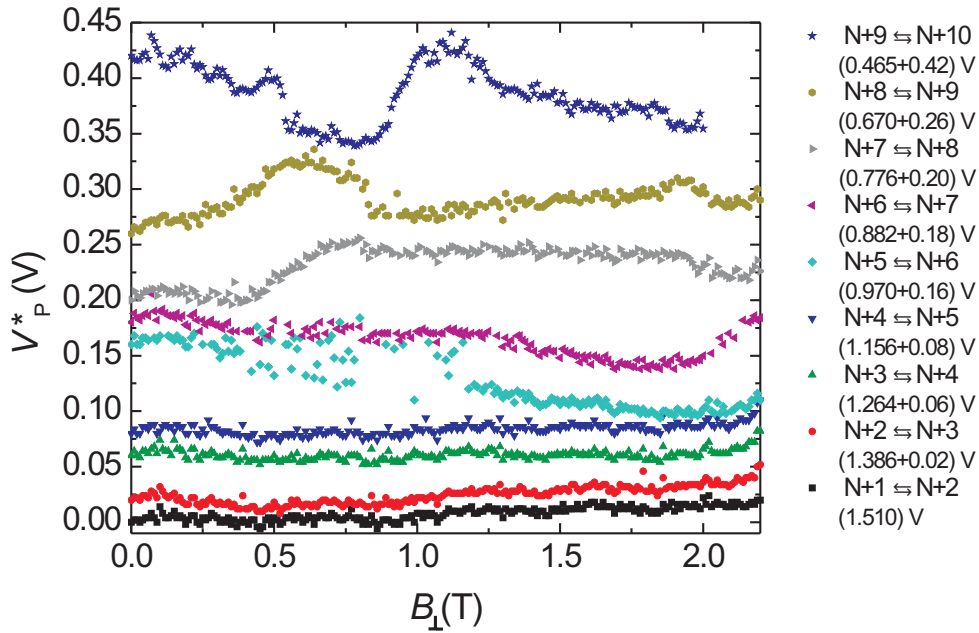
6.2 Magnetically induced chessboard pattern

Figure 6.2 shows a color-scale plot of the conductance (left panel) and the thermovoltage (right panel) of the QD as a function of magnetic field $B_\perp$, applied perpendicular to the plane of the 2DEG, and as a function of plunger gate voltage V_P. Bright and dark colors correspond to low and high conductance and thermovoltage domains, respectively. Two transport regimes can be identified immediately. For $V_P \geq -1.0$ V, the conductance shows pronounced patterns, while the thermovoltage measurement is characterized only by a moderate variation in the signal amplitude. For $V_P \leq -1.0$ V, the situation is reversed. Here, the thermovoltage shows large signal amplitudes, while the conductance shows a less pronounced signature.

For $V_P \leq -1.0$ V, the coupling of the QD to the leads is weak. This results in relatively sharp SET conductance peaks and a low Coulomb blockade valley conductance. Correspondingly, the thermovoltage oscillations show the pattern of an intermittent sawtooth [cf. right panel of Fig. 6.2], as has been described in Chap. 4. In the weak coupling regime, the exact positions of the SET conductance peaks can be identified in the conductance as well as in the thermovoltage diagrams. This can be used to assign each SET conductance peak to its corresponding thermovoltage oscillation.

The sharp SET conductance peaks allow a detailed analysis of the peak positions to be done. Figure 6.3 shows the evolution of the SET conductance peak positions V_P^* as a function of the magnetic field. For clarity, the peak positions have been shifted to zero voltage and additionally offset. The voltage shifts are given in the legend of Fig. 6.3. In the gate voltage range $V_P \leq -1.1$ V [cf. Fig. 6.2], i.e. for electron numbers ranging from $N+1$ to $N+4$ (lowest four curves in Fig. 6.3), the peak positions clearly evolve in pairs (lowest four curves). This can be explained by the fact that when electrons are successively added to the QD, two electrons with spin up and spin down can occupy the same orbital state. If the total spin of the QD alternates between $S = 0$ (all spins are paired) and $S = 1/2$ (one spin remains unpaired), an odd-even behavior is expected. Adding one electron to a QD of the first kind ($S = 0$, all spins are paired) requires an extra amount of energy $\delta E_O(B)$ in addition to the charging energy, since a higher orbital state has to be occupied. This extra charging energy is not needed, if an electron is added to a QD with $S = 1/2$, since the electron can occupy the same orbital state as the unpaired electron, building a spin singlet. The evolution of the orbital states as function of magnetic field, which was first calculated the first time by Fock and Darwin [Foc28, Dar30], differs for different QD states. The pairing behavior allows even and odd numbers of electrons on the QD to be identified. In Figs. 6.2 and 6.4, small circles mark an odd number of electrons on the QD.

For more positive plunger gate voltages ($V_P \geq -1.0$ V), the conductance peak positions show considerable variations in the V_P-direction [see Fig. 6.3]. Here, the coupling of the QD to the reservoirs is increased (as can be seen by the width of the SET conductance peaks), and the conductance reaches considerable high values even in some Coulomb blockade valleys of the (V_P, $B_\perp$)-plane [cf. left panels of Figs. 6.2 and 6.4]. The regions of low and high valley conductance alternate along both the V_P and the B directions. This forms a chessboard like pattern, which is displayed in detail in Fig. 6.4. A similar structure can be observed in the measurement of the thermovoltage in Fig. 6.4 (right panel), though not as pronounced as in the conductance measurement. For direct comparison, the hexagonal pattern obtained from the conductance measurement is sketched on top of the thermovoltage data. A more complex pattern is observed in the V_P-direction for the thermovoltage measurement, since the positions of the conductance resonances are expected only at every second zero-crossing of the thermovoltage signal amplitude. In the $B_\perp$-direction, the correspondence of both chessboard patterns is more obvious, since regions of positive and negative V_T alternate with the same periodicity ($\Delta B_\perp = 0.355$ T) as the regions of zero and high CB valley conductance.

Nonlinear differential conductance measurements clarify the origin of the enhanced conductance in the Coulomb blockade valleys. From the analysis of the Coulomb blockade diamonds [KMM$^+$97], charging energies varying from $E_C = 0.6$ meV to $E_C = 1.5$ meV and corresponding intrinsic level widths of $h\Gamma \sim 0.35$ meV to $h\Gamma \sim 0.15$ meV have been deduced respectively for strong and weak coupling of the dot to the reservoirs. Figure 6.5 shows a color-scale plot of the differential conductance as a function of the QD potential ($\propto V_P$) and V_{DS} at a magnetic field of $B_\perp = 1.2$ T. Here, alternating regimes of low
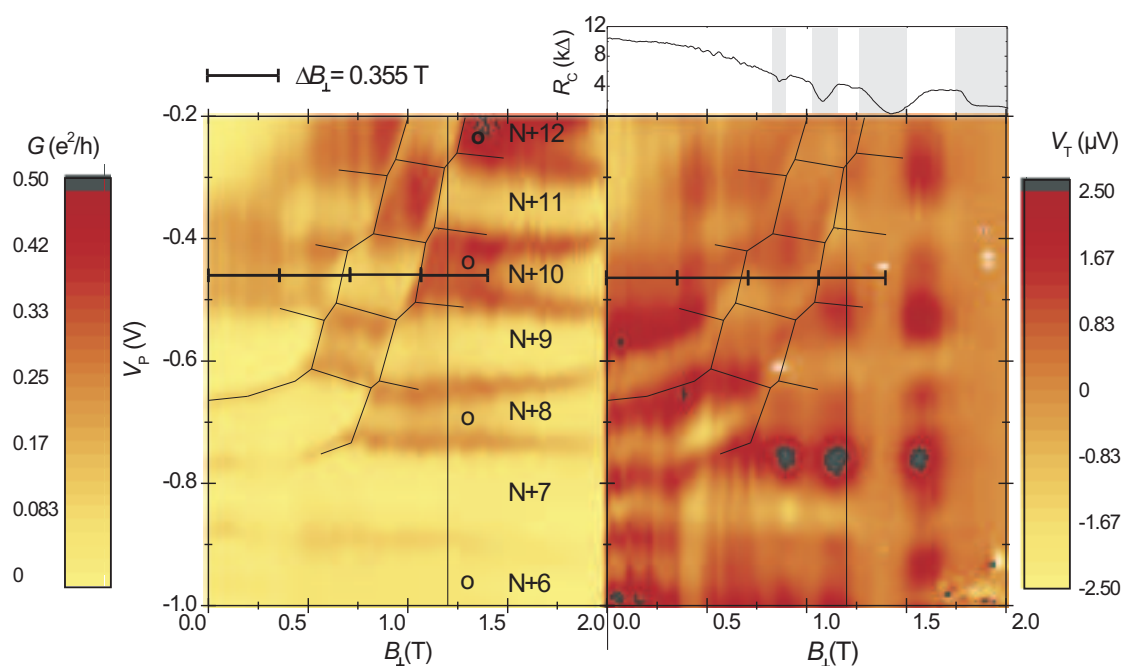
Fig. 6.4: Color-scale plot of the linear conductance G (left panel) and the thermovoltage V_T (right panel) as function of magnetic field $B_\perp$ and plunger gate voltage V_P in the regime of a strong coupling of the QD to the reservoirs (small negative plunger gate voltages). The horizontal bar indicates the periodicity of the chessboard pattern ($\Delta B_\perp = 0.355$ T) in the direction of the magnetic field. A plot of the longitudinal resistance of the current heating channel R_C as a function of the magnetic field has been added as additional panel above the thermovoltage color scale plot. Grey shaded regions indicate magnetic field ranges of Shubnikov-de Haas oscillation minima in the panel of the heating channel resistance.

Fig. 6.5: Color-scale plot of the finite-bias differential conductance as a function of the QD potential ($\propto V_P$) and the externally applied bias voltage acros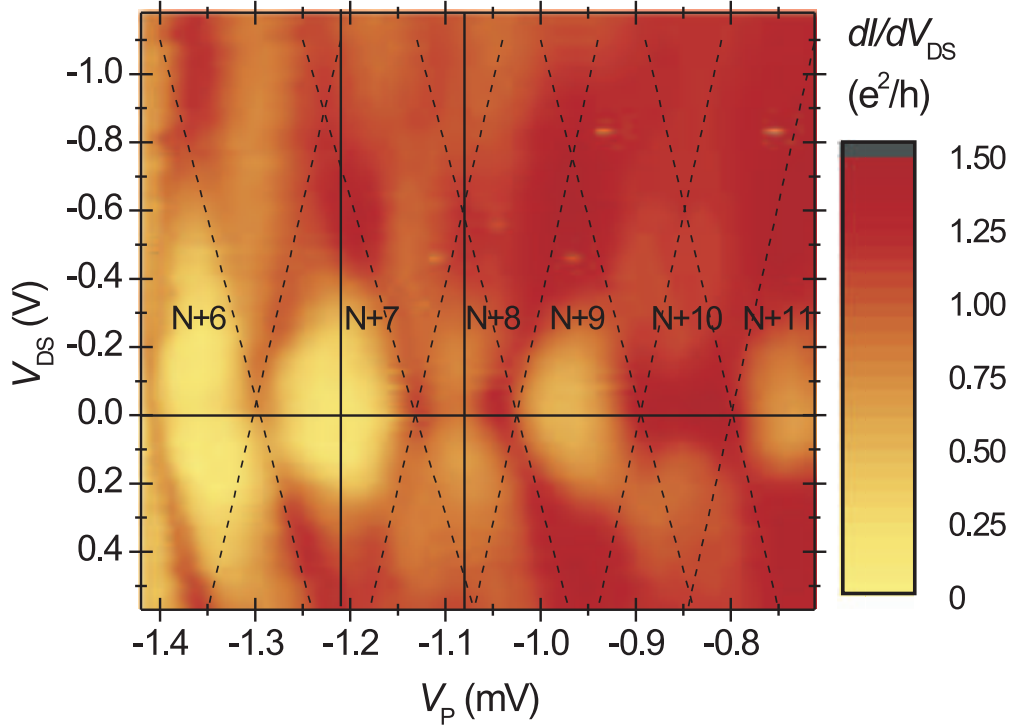s the QD (V_{DS}). Alternating regimes of low and high conductance are observed between successive conductance peaks within the CB diamonds (dashed lines).

and high conductance between two successive conductance peaks can be observed in the gate-voltage range $-0.7 < V_P < -1.2$ V along the zero bias line [$V_{DS} = 0$, horizontal solid line in Fig. 6.5].[1] At $V_P = -1.08$ V (high conductance between two Coulomb blockade peaks) a V_{DS}-dependent trace shows a clear zero bias peak in the differential conductance, in contrast to a V_{DS} trace taken in the adjacent conductance valley at $V_P = -1.21$ V [Fig. 6.6]. For $V_P < -1.2$ V, the coupling between the QD electrons and the surrounding 2DEG decreases and no further zero bias peaks are observable in the V_{DS}-dependent differential conductance. These zero bias resonances are characteristic for Kondo correlated systems [Hew93]. In the following, regions of enhanced conductance in the Coulomb blockade valleys of the chessboard pattern are assigned as magnetic field and voltage ranges where spin correlations modify the transport characteristics.

In the past, several experimental investigations of QDs in magnetic fields perpendicular to the 2DEG plane have shown a similar magnetically induced chessboard pattern in the conductance [SWEvK00, KWS$^+$01, SJH$^+$02, FKH$^+$02, KFB$^+$03]. The occurrence of the hexagonal pattern, which is indicated with red lines in Fig. 6.4, has been explained

---

[1]The QD potential has shifted with respect to those in Figs. 6.2 and 6.4. Due to a power failure of the gate voltage source during the measurement, the QD had to be readjusted.
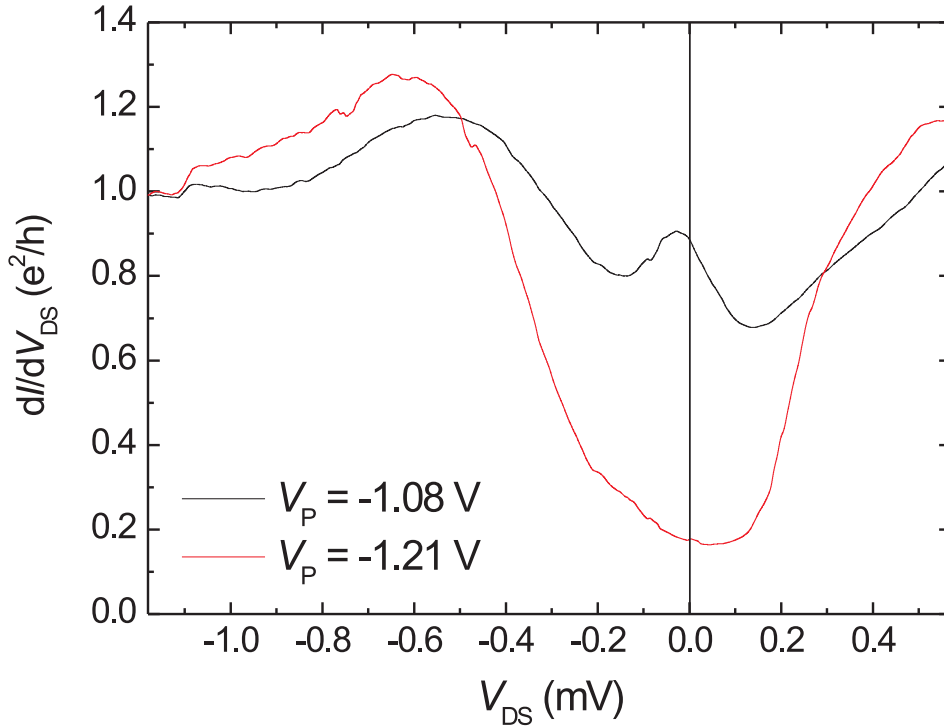
Fig. 6.6: Traces of the differential conductance as a function of the applied drain-source voltage at constant plunger gate voltages $V_P = -1.08$ V (black line) and $V_P = -1.08$ V (red line).

quantitatively in terms of a constant-interaction model of coupled QDs [SvdWDF$^+$03].

In strong perpendicular magnetic fields, compressible and incompressible regions are formed in the QD corresponding to the Landau level quantization in the 2DEG [MFK$^+$92, vKGW05].[2] The electron density distribution of a QD in the quantum Hall regime can be calculated by using a self-consistent iterative solution of the QD Hamiltonian [Eq. (1.1)] in the framework of the Thomas-Fermi approximation. Figures 6.7(a) and (b) depict schematically the situation for a QD when only two Landau levels are filled. Within the constant-interaction model [SvdWDF$^+$03], electrons from different Landau levels (index ν) behave like electrons from separate QDs with capacitances C_ν. These QDs are capacitively coupled to each other $C_{\nu_i,\nu_{ii}}$ and the plunger gate couples capacitively to all Landau levels with different lever arm ($C_{p,\nu}$).

Principally, the magnetic field induces the depopulation of higher Landau levels to lower Landau levels. For low enough magnetic fields, the polarization of the electrons due to the Zeeman splitting can be ignored, and successive depopulation due to an increase of the applied magnetic field results in an alternating total spin ($S = 0 \leftrightarrow S = 1/2$) of

---

[2]Compressible regions exhibit a metallic behavior of the electrons, which screen the confining potential. Incompressible regions are characterized by a constant electron density in the regime of completely filled Landau levels. They show an insulating behavior (energy gap to the next Landau level), and the electrons cannot screen the confining potential completely.
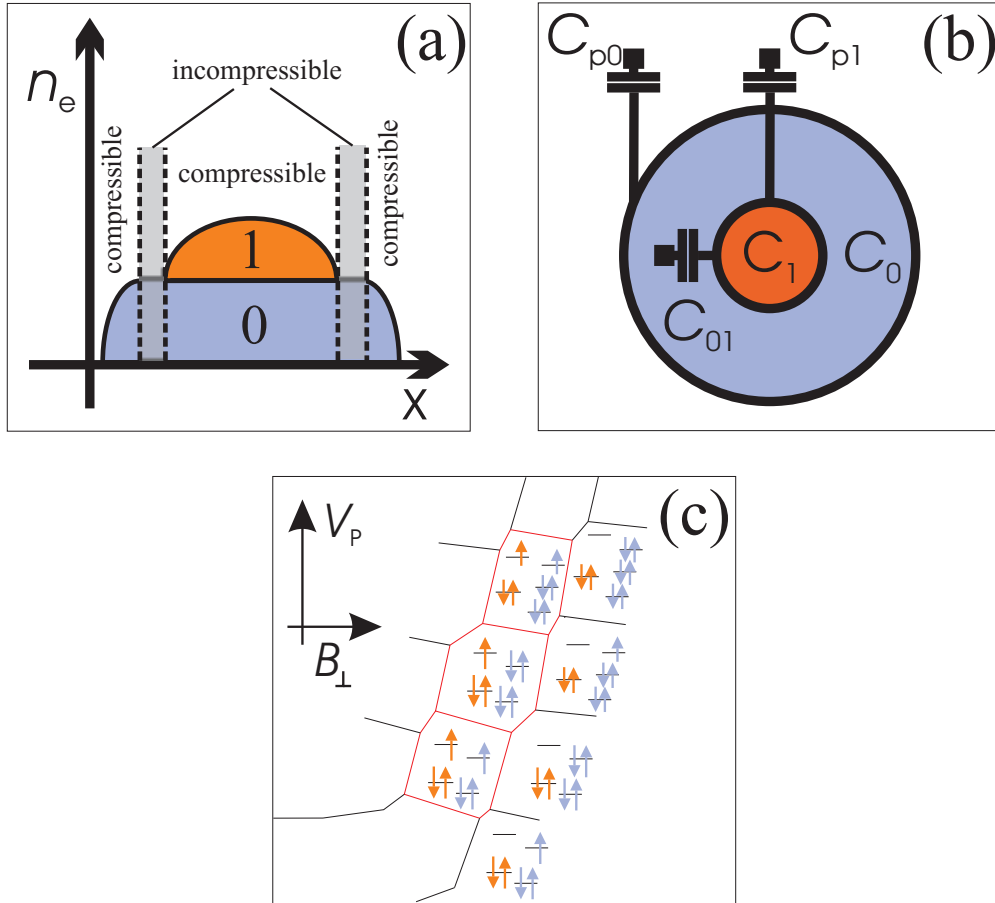
Fig. 6.7: Schematic illustrations of a QD in a high magnetic field, which depict the origin of the chessboard pattern. (a) Electron density profile for a QD in a high magnetic field when only two Landau levels (0 and 1) are occupied. (b) Capacitance model of the corresponding effective double-QD from (a). C_0 and C_1 denote the capacitances of the Landau levels; C_{12}, C_{p0} and C_{p1} denote the capacitive coupling of the Landau levels to the plunger gate. (c) Schematic drawing of the chessboard pattern from Fig. 6.4 including representative spin configurations of inner (orange) and outer (blue) Landau levels.

the lowest Landau level. Since inner (higher) Landau levels couple much weaker to the drain and source contacts than the outer (lower) Landau levels, the spin-correlation of electrons in the leads and the QD is mainly determined by the spin state of the outermost (lowest) Landau level. Due to the possibility of enhanced spin scattering, an enhanced conductance results when the total spin of the lowest Landau level $S = 1/2$ ($S \neq 0$).

The periodicity $\Delta B_\perp$ of the alternating spin configuration in the outermost Landau level is roughly proportional to the addition of one flux quantum $\Phi_0 = h/e$ to the dot [FKH$^+$02]. Thus, the size of the QD can be estimated by using the formula

$$d_{QD} = 2\sqrt{\Phi_0}/(\pi \Delta B_\perp). \tag{6.2}$$

For $\Delta B_\perp = 0.355$ T, the diameter of the QD is approximately 120 nm. This is in good agreement with the lithographically determined diameter of $d = 250$ nm, since the difference between the two values can be explained by the increased depletion of the 2DEG around the biased gates. Assuming an overall electron density of $n_e = 2.3 \cdot 10^{11} \mathrm{cm}^{-2}$, the total number of electrons is about 26 for the QD labeled $N + 10$.

The thermovoltage shows an additional modification of the signal amplitude as a function of the magnetic field. An almost zero signal amplitude coincides with the occurrence of a minimum in the longitudinal resistance of the heating channel R_C [see upper panel of Fig. 6.2]. The minima of the heating channel resistance result from the conductance quantization in the 2DEG in strong magnetic fields, which are the origin of the quantum Hall effect (QHE). In a conductance valley, only completely filled Landau levels contribute to the electron transport. At this point, it seems reasonable to argue that the scattering is considerably reduced in this state and the dissipation of the heat takes place close to the ohmic contacts. At the entrance of the heating channel, the electron gas may not distribute its energy among the electrons and the electron temperature in the heating channel does not increase. The necessary temperature difference for the thermovoltage measurements may not be provided at integer filling factors of the heating channel electron gas, and the signal amplitude vanishes at these magnetic fields. However, in the weak coupling regime of the QD, the thermovoltage oscillations are still visible. Thus a temperature difference still exists. This point is emphasized again in Sec. 6.4.2, where the origin of amplitude modulation is discussed in more detail.

6.3 Contributions of spin-correlations to the thermopower

Due to the strong variation of the thermovoltage signal amplitude as a function of magnetic field, the following discussion focuses on measurements at fixed magnetic fields.

In Fig. 6.8, conductance and thermovoltage measurements are shown as function of V_P at $B_\perp = 0$ T [Fig. 6.8(a)] and $B_\perp = 1.2$ T [Fig. 6.8(b)]. The positions of the conductance resonances (indicated by the two vertical black lines) have been used to compensate for

Fig. 6.8: Conductance (upper panel), thermovoltage (lower panel, black line) and Mott thermopower (lower panel, red line) as function of plunger gate voltage V_P at (a) $B_\perp = 0$ T and (b) $B_\perp = 1.2$ T. Black horizontal lines are added as a guide to the eye, and mark the positions of SET conductance peaks, which have been used to identify the position of the corresponding thermovoltage oscillations.
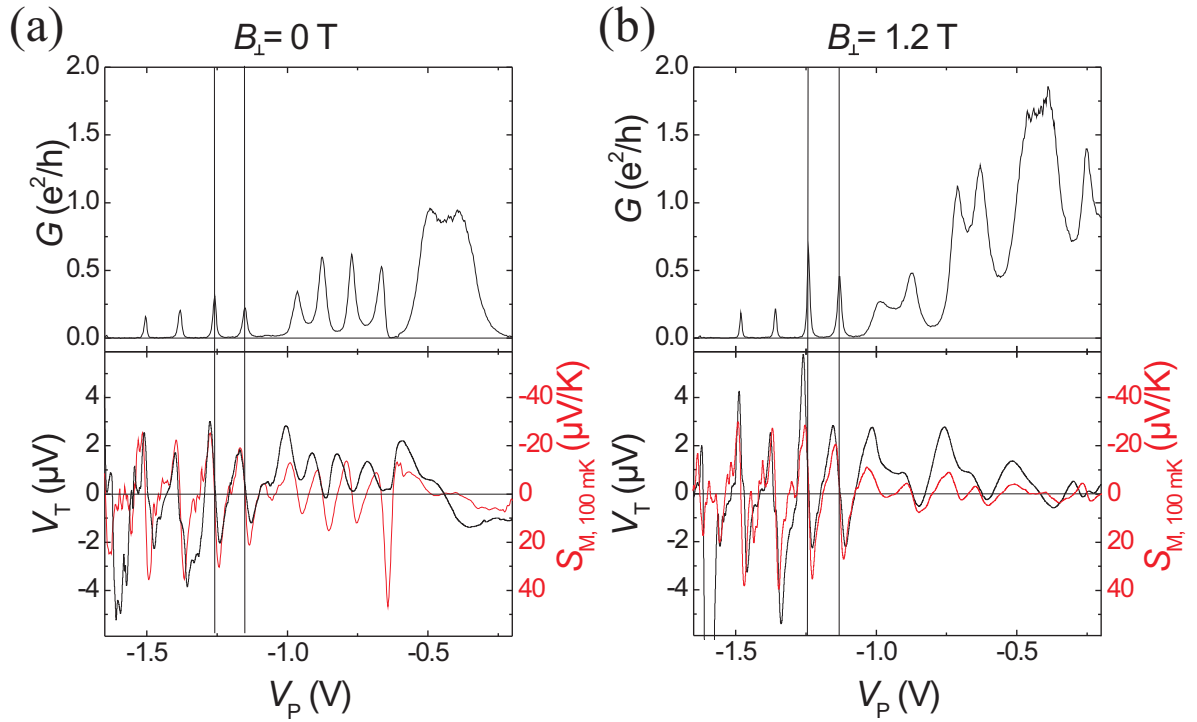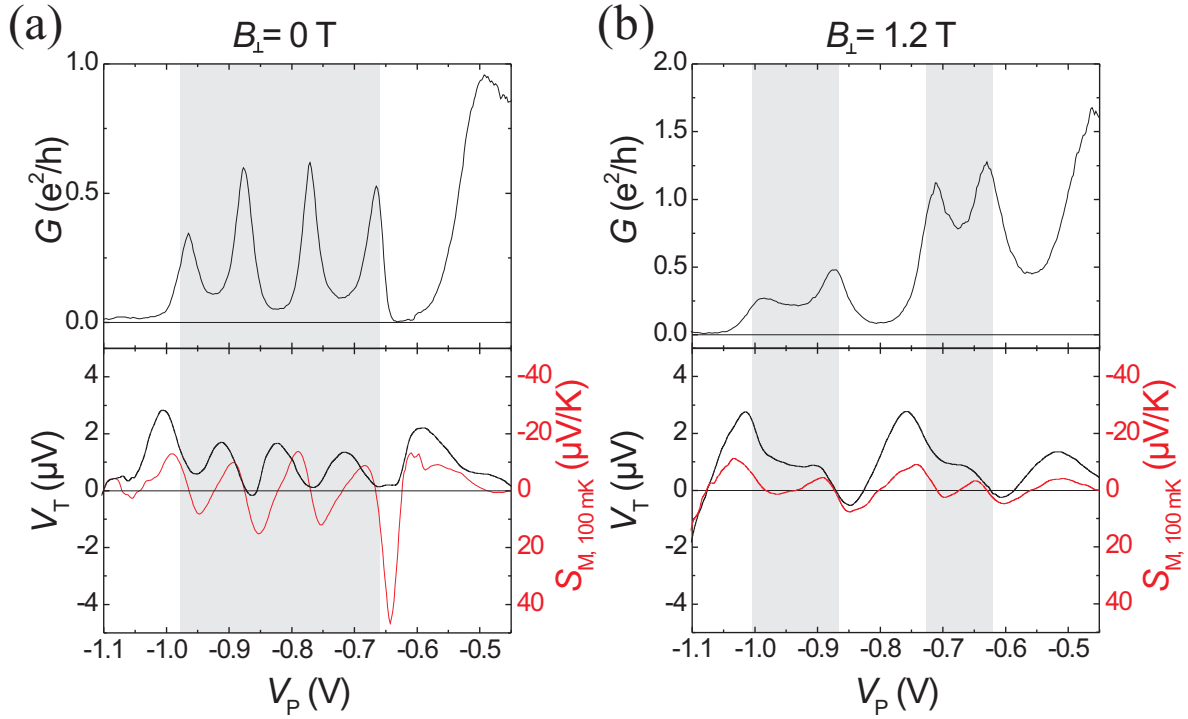
Fig. 6.9: Conductance (upper panel), thermovoltage (lower panel, black line), and Mott thermopower (lower panel, red line) as function of plunger gate voltage V_P at $B_\perp = 0$ T [(a)] and $B_\perp = 1.2$ T. Black horizontal lines are added as a guide to the eye, and mark the positions of Coulomb blockade resonances.

potential shifts in the thermovoltage measurement. As mentioned above, the measurement can be split into two transport regimes. The regime of weak QD-lead coupling ($V_P < -1.1$ V) has already been discussed in Chap. 4. Hence, the discussion here concerns mainly the regime of the strong QD lead coupling ($V_P > -1.1$ V).

Figure 6.9 presents detailed plots of the thermovoltage V_T as a function of plunger gate voltage V_P (lower panel) together with the corresponding conductance curve (upper panel) in the strong coupling regime at $B_\perp = 0$ and 1.2 T. The strong coupling of the QD to the leads results in an enhanced conductance between SET conductance peaks due Kondo correlations in the gate voltage ranges indicated by the grey shaded areas.

At $B_\perp = 0$ T, an overall enhancement of conductance can be observed in the Coulomb blockade valleys between the SET conductance peaks at $V_P = -1.0$ V and $V_P = -0.6$ V. In the same range of the plunger gate voltage, the thermovoltage exhibits an oscillating behavior. In contrast to the weak coupling regime, where positive and negative thermovoltage signal amplitudes are measured in the vicinity of an SET conductance peak, the thermovoltage shows only positive contributions, except for a small plunger gate voltage range around $V_P = -0.85$ V.

The contrast between thermoelectric transport with and without spin-correlations is enhanced at the magnetic field of $B_\perp = 1.2$ T [cf. Fig. 6.8(b)]. In the conductance (upper

panel), the alternating occurrence of spin-correlated and normal transport produces an alternating lifting of the Coulomb blockade between the SET conductance peaks. In the bottom (thermovoltage) panel, a striking difference between the behavior of V_T in the spin correlated regime as compared with the regime without spin correlations is directly conspicuous.

In the transport regime without spin correlations, the thermovoltage exhibits both, negative and positive signal amplitudes in the vicinity of a conductance peak. Corresponding to the discussion in Chap. 4 and Refs. [BS92, TM02], this behavior results from sequential and cotunneling contributions to the thermopower. In this regime, the thermovoltage line shape follows qualitatively the negative parametric derivative of the conductance data, as described by Mott's relation, Eq. (2.26) [Zim63]. The red lines in the bottom panels of Figs. 6.8 and 6.9 show the qualitative behavior of the thermopower as expected from Mott's relation.

For the spin correlated transport regime, the striking experimental result is that in the presence of spin correlations at $V_P = -0.70$ V and -0.93 V, V_T exhibits *only positive* values, while in the absence of these correlations ($V_P = -0.60$ V and -0.85 V), the usual negative V_T shows up between the Coulomb resonances. A comparison to the semiclassically expected S_{Mott} [cf. Eq. 2.26] in Figs. 6.8 and 6.9 shows significant additional contributions at $V_P = -0.70$ V and -0.93 V of approximately 0.5 μV. This cannot originate from single particle effects in the close vicinity of the Fermi energy. Clearly, spin correlations are a prime candidate for explaining the occurrence of these extra contributions.

Further information can be obtained from the dependencies of these effects on the temperature, which are shown in Fig. 6.10.[3] Figure 6.10 (a) shows the temperature dependence of the thermopower anomaly. The additional contributions to the thermopower are suppressed at higher temperatures. As a consequence, the expected valley reappears between the main CB resonances. For comparison, Figs. 6.10 (b) and (c) show the temperature evolution of the zero bias conductance and the bias(V_{DS})-dependent differential conductance of the QD. The zero bias resonance in these curves disappears on a similar temperature scale as the extra features in the thermovoltage, establishing a very strong indication that these features are related to spin correlations.

6.4   Discussion

6.4.1   Kinetic spin-correlation contribution to the thermopower

The anomalous behavior of the thermovoltage in the spin-correlation regime points to an asymmetry in the position of the spin correlation resonance ε_{QD} with respect to the Fermi

---

[3]Note that these experiments were done on the same sample but for a different cooling cycle, where the regime of spin correlations was observed for a different adjustment of the voltages applied to the QD gates.
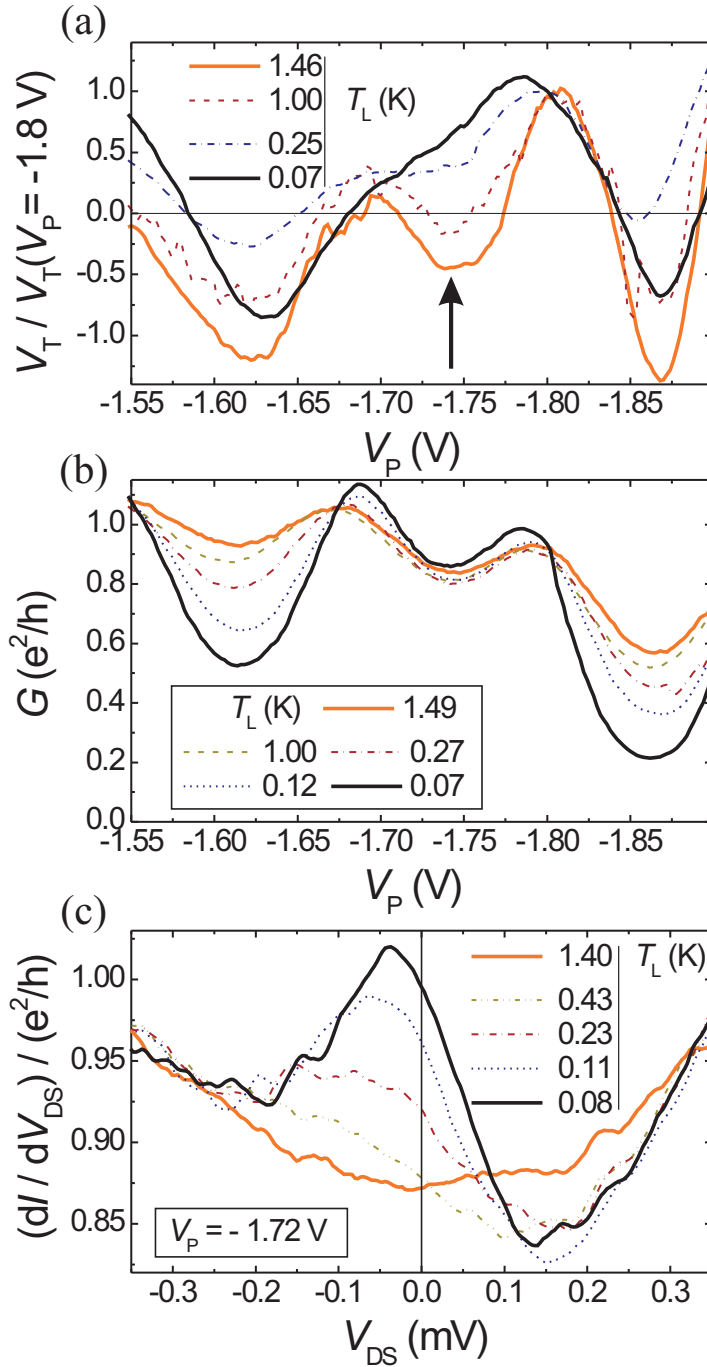
Fig. 6.10: (a) Thermovoltage signal for various lattice temperatures T_L at constant temperature difference ΔT. The curves are normalized to the value at $V_P = -1.8$ V. At high temperatures the spin contribution to the thermopower between two CB peaks decreases and the oscillating CB substructure of the thermopower reappears (indicated by the arrow). (b,c) Temperature dependent (differential) conductance of the zero bias resonance as a function of QD potential V_P and bias voltage V_{DS}.

energy levels E_F of the reservoirs. One can directly deduce the position of ε_{QD} relative to E_F from the sign of the thermovoltage signal. In order to explain the observation of a positive thermovoltage signal, the spectral density of the correlated state on the QD must have its weighted maximum above E_F in the leads. The bias(V_{DS})-dependent differential conductance traces which are shown in Fig. 6.10(c) confirm this assumption. Especially the low temperature data exhibit a maximum of the spin-correlated conductance at $V_{DS} \approx -50$ μV.

From the experimental characterization of the QD, it has been found that $\bar{\mu}_{QD,N}/h\Gamma > -3$ in the gate voltage region where spin correlations are observed [cf. Fig. 6.9 ($V_P > -1.2$ V)]. By describing the spin correlated QD in terms of an asymmetric Anderson model (i.e. $\bar{\mu}_{QD,N} \neq -E_C/2$)[4] [Hew93, CHZ94, BF01, DL02], it implies that one is in the mixed-valence regime. In this limit, the spectral density of the hybridized state has its maximum above E_F [CHZ94, Hew93]. The strong coupling to the reservoirs leads to significant charge valence fluctuations, i.e. a delocalization of the QD charge. Thus, the average electron occupation number deviates from an expected integer number, which results in an overall asymmetry between electron and hole-like transport. According to Ref. [CHZ94], enhanced positive contributions to the thermovoltage are expected in this case. This is in contrast to numerical calculations for an ideal Kondo-QD system, where the QD charge is an integer multiple of the electron charge and one expects both positive and negative contributions to the thermopower, due to the electron-hole symmetry of the problem [DL02].

It should be noted here that many experiments reported on Kondo QDs very often operate in the mixed valence regime [GGSAM+98, COK98]. This notion may have escaped general attention, because of the insensitivity of zero bias conductance measurements with respect to the exact location of the spectral density of the hybridized state. In contrast, the thermopower is very sensitive to this location [BF01], which is why a non-zero contribution to the thermopower is observed.

Further deviations of the experimental results from the single level Anderson model are expected for the following additional reasons. First, the intrinsic level broadening of the QD states, which even leads to an overlap of the states across the CB gap, results in a non-zero conductance in the CB valleys without spin correlations at $V_P > -1.1$V (cf. Fig. 6.9). Thus, the truncation of the spectrum to a single level is not strictly possible. Second, it has to be considered that the QD ground state spin may differ from S= 1/2 at $B_\perp = 0$ T, or that the electrons of the QD occupy various Landau levels for $B_\perp \neq 0$ T, which corresponds to a multiple QD configuration. In these cases, the Anderson impurity model does not describe the transport behavior quantitatively, and a strongly non-monotonic behavior is expected for the transport contributions of the spin correlations as a function of the experimental parameter B, T and V_P [PG01, SWEvK00]. Especially a multi-dot configuration is expected to show a spin-correlation resonance at finite bias [KKM03].

---

[4]Note that, using the notation of the Anderson model as described in Refs. [Hew93, CHZ94], $\bar{\mu}_{QD,N}$ varies between 0 and $-E_C/2$ during the CB oscillations.

6.4.2 Spin-entropy flux

So far, the discussion has focused on the kinetic contribution of the heat flux through the QD and the observed thermoelectric behavior has been strictly attributed to the properties of the QD. This treatment leaves two questions unaddressed regarding the spin-correlated transport regime.

First, the QD cannot be seen as an isolated system in the limit of a strong coupling to the reservoirs. Thus, one can argue that the observed thermoelectric effects have to be attributed to both subsystems, i.e. to the QD *and* the reservoirs. In this regard, the question arises, whether there are any signatures of thermoelectric effects which result from the thermopower of the 2DEG in the reservoirs.

Second, it has been shown by measurements of the finite bias differential conductance that the energy difference between the spin-correlated state and the Fermi-levels of the reservoirs is small. Correspondingly, the kinetic contribution to the heat flux is small and one may ask whether additional kinetic or configurational contributions to the heat flux can account for or contribute to the observed behavior of the thermopower in the spin correlated transport regime, respectively.

In order to address both questions, the magneto-thermopower of the weak coupling regime and the strong coupling regime of the QD has to be analyzed in more detail in the following.

6.4.2.1 Magnetothermopower of the 2DEG

Figure 6.11 presents two traces of the thermovoltage as a function of the QD plunger gate voltage at $B_\perp = 1.2$ T and $B_\perp = 1.4$ T. For $V_P \lesssim -1.0$ V, both traces exhibit regular thermovoltage oscillations of almost the same oscillation amplitude. For $V_P \gtrsim -1.0$ V, the two curves differ significantly from each other. While for $B_\perp = 1.2$ T thermovoltage oscillations are clearly visible, the oscillations vanish and the thermovoltage is almost zero for $B_\perp = 1.4$ T. The modulation of the thermovoltage oscillation amplitude as a function of the magnetic field occurs for magnetic fields above $B_\perp > 0.5$ T as can be seen in Figs. 6.2 and 6.4. The periodicity coincides with the Shubnikov-de Haas oscillations of the longitudinal resistance R_C of the heating channel. A minimum or a maximum in the thermovoltage oscillation amplitude occurs for magnetic fields where also $R_C(B_\perp)$ shows a minimum or a maximum. The vanishing of the thermovoltage signal is obviously independent of the SET conductance peaks, the QD occupation number and the spin state.

Similar vanishing of the thermopower has been observed for the longitudinal thermoelectric power (S_{xx}) of high mobility heterostructures in the integer and fractional quantum Hall regime [OvKP86, FDS$^+$88, ROJ$^+$88, ZMW$^+$93, YBSS94, BGM$^+$95]. According to the theory of the diffusion thermopower in high magnetic fields, S_{xx} is independent of scattering and is given by the entropy per particle divided by the particle charge [GJ82, JG84, Lyo84, Oji84].
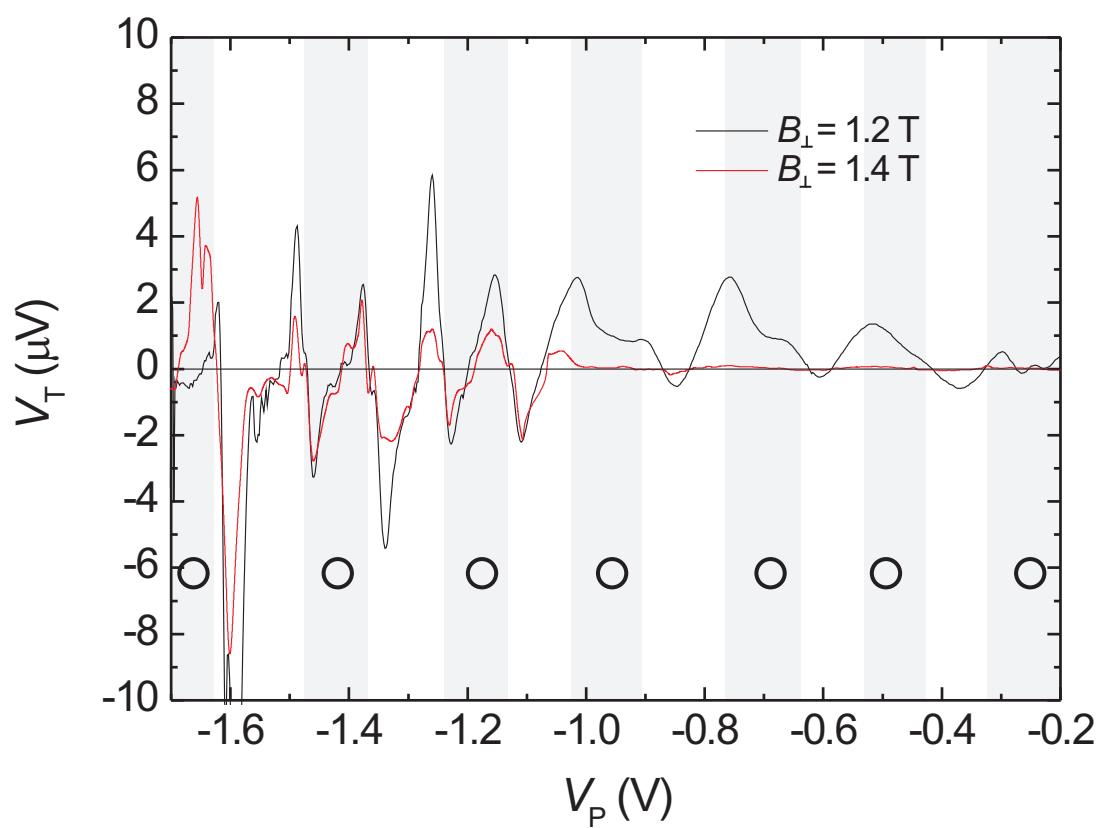
Fig. 6.11: Thermovoltage traces as function of plunger gate voltage V_P at $B_\perp = 1.2$ and 1.4 T. The grey-shaded areas and small circles mark the gate voltage ranges where an odd number of electrons occupy the QD.

In a full Landau level, the charge carriers have zero entropy. Thus, S_{xx} is expected to vanish at integer filling factors ν for $k_B T \ll \hbar\omega_C$ and $h\Gamma_{LL} \ll \hbar\omega_C$, where $h\Gamma_{LL}$ is the Landau level broadening and $\hbar\omega_C$ is the cyclotron energy. For a half-filled Landau level, the entropy per particle is maximum, and S_{xx} reaches the universal value

$$S_{xx} = g\frac{k_B}{q}\frac{\ln 2}{\nu}, \tag{6.3}$$

where the factor g is a function of $k_B T/\Gamma_{LL}$ [ZL84]. The entropy of the charge carriers in the Landau levels can be seen to be analogous to the entropy of the particles in filled or partially filled bands. For a filled band, the entropy (i.e. quantity of heat divided by temperature) vanishes and heat can be carried to the next level only by activation. The entropy becomes maximum (i.e. $\ln 2$ per state) at half-filling of the band and drops as the band is gradually emptied or filled [Lyo84].

The positions of the amplitude variations of the QD thermopower as a function of the magnetic field show qualitative agreement with these considerations. For $V_P \gtrsim -1.0$ V, the QD is strongly coupled to the 2DEG regions in the leads. As a consequence, it seems that the thermopower of the QD-reservoir system is determined by a mixture of the behaviors of both subsystems. These are the QD-state, which determines the wave function overlap of the electronic states in the QD and in the leads, *and* the entropy of the electrons of the 2DEG. For $V_P \lesssim -1.0$ V, the coupling of QD states to the reservoirs is weak and sequential tunneling in the classical transport regime dominates. Classical rate equations [cf. Chap. 4.3 and Ref. [Bee91]] describe the thermoelectric transport. In this case, the QD can be seen as an isolated system and the thermopower is mostly determined by the incoherent transport of electrons through the QD.

The discussion above actually implies that the connecting reservoirs differ from ideal reservoirs with fixed temperature and (electro)chemical potential, which have been assumed so far. More quantitative results would be desirable in order to support the above statements. However, the lack of adequate samples prevented further studies in this transport regime, which leaves the regime of "coherent entropy transport" for future studies.

6.4.2.2 Spin-Entropy of strongly correlated systems

In principle, one expects contributions from both spin and orbital degrees of freedom to the entropy flux. However, in systems with dominating strong electron-electron interaction, the thermopower should be dominated by the spin degrees of freedom. This spin entropy contribution to the thermopower is known from the thermoelectric transport in the correlated hopping regime [CB76], which occurs in impurity conduction or glasses containing transition metal ions [AM98, AM01], and in 1-dimensional organic salts in the narrow band limit [CKE79, Ben74, KBC76]. Recently, the spin entropy contribution to the thermopower has received strong, renewed attention, since it has been proven to be the origin of the giant thermoelectric power in layered cobalt oxide structures [WRCO03].

In these strongly correlated systems, the spin entropy flux accompanying electron transport gives significant contributions to the thermopower [Muk05, KTM00, KM01]. With respect to QD systems, one may anticipate similar large effects since the transport is dominated by strong electron-electron interactions and correlation effects. So far, investigations of the thermopower on single QDs have not shown explicit signs of spin entropy transport, which may be due to the hardly predictable interplay between the various kinetic contributions to the thermopower.

Following the theoretical considerations for the charge transport between localized ion sites in the calculation of the thermopower, a term S_{SE} does arise which is of the form [Hei61, AM98, AM01]

$$S_{\mathrm{SE}} = -\frac{1}{q}\Delta\mathbb{S}. \tag{6.4}$$

Here, $\Delta\mathbb{S}$ is the change in the entropy of a lattice or impurity site due to the *presence* of a charge carrier q. This term takes into account the fact that the charge transport between two heat reservoirs is accompanied by an entropy flow due to the change of the configurational entropy of the unoccupied or occupied lattice sites.

For example, the addition of an electron to an empty, spin degenerate state of an isolated site changes its configurational entropy by $\Delta\mathbb{S} = k_B(\ln g_f - \ln g_i) = k_B(\ln 2 - \ln 1) = k_B \ln 2$, where $g_{i,f}$ denotes the initial and final degree of degeneracy. The temperature driven electron transport along a linear chain, which is made up of such lattice sites, enhances the entropy at the end of the chain where the accumulation of electrons occurs.

At this point, it seems straight forward to directly translate this "*Gedanken experiment*" to the single QD system, although a single site may only under certain circumstances be regarded as a very short version of a one-dimensional chain. Starting from this theoretical concept of spin entropy transport, a simple model for the QD spin correlated transport regime is discussed in the following.

Basically, the number of electrons on the QD has to fluctuate or change during transport in order for a spin entropy contribution to the thermopower of QDs to be observed. This condition is necessary, since the spin entropy term S_{SE} results from the entropy change due to the *presence* of an electron on the lattice or impurity site. Thus, spin entropy contributions to the thermopower of QDs are expected to occur in the vicinity of SET conductance peaks, where the number of electrons on the QD changes.[5] In transport regimes of the full CB or in the completely screened Kondo regime, spin entropy contributions are expected to be small compared to other contributions since the number of electrons on the QD and thus the configuration remains constant. Assuming that the QD is in a twofold spin degenerate state and that the hybridization with the free electrons in the reservoirs results in a spin-correlated transport, the Coulomb blockade oscillations can be divided into four sections as depicted in Fig. 6.12. Panel (I) of Fig. 6.12 sketches the zero-bias conductance of a QD as a function of the number of electrons on the QD. The

---

[5]This might as well be interpreted as a change of the QD valency.

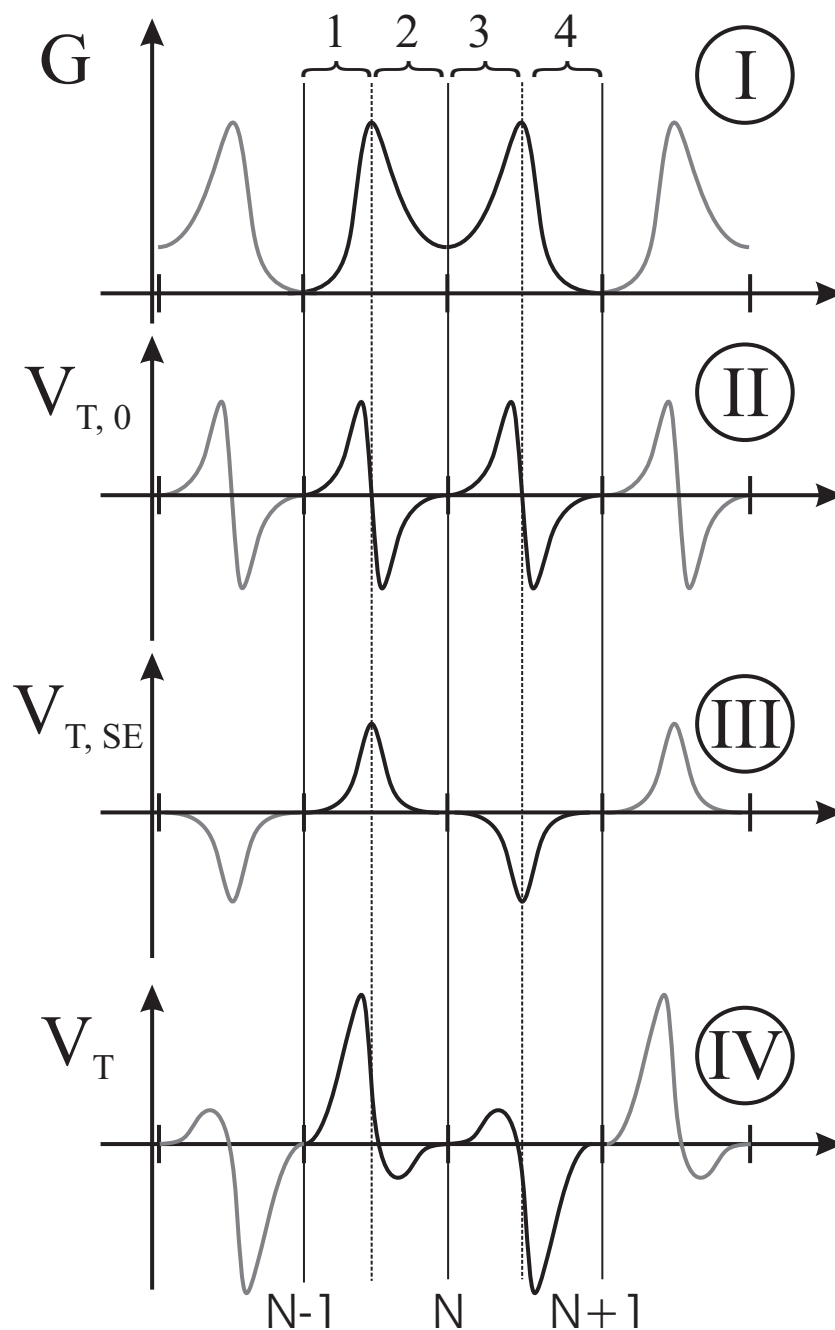**Fig. 6.12:** Conductance and thermovoltage in the spin-correlated transport regime as a function of the number of electrons on the QD. For a spin-degenerate ground state of the N-electron QD, panels I-IV qualitatively show the conductance (I), the thermovoltage without spin correlation effects (II), the spin entropy contribution to the thermovoltage (III), and the expected total thermovoltage (IV).

N-electron QD is assumed to have a spin-degenerate ground state ($g = 2$) and the conductance in the CB valley between the SET conductance peaks is enhanced due to spin- or Kondo- correlated transport. The ground states of the $N \pm 1$ QDs are not degenerate ($g = 1$).

In region 1, the dominating charge transport mechanism is the addition of one electron to the QD from the hot reservoir, which then leaves the QD to the cold reservoir. During transport, the change in entropy of the QD due to the presence of the excess electron is $\Delta\mathbb{S} = \mathbb{S}_f - \mathbb{S}_i = k_B(\ln g_f - \ln g_i) = k_B(\ln 2 - \ln 1) = k_B \ln 2$. Thus, the spin entropy contribution to the thermopower is given by $S_{\text{SE}} = -\frac{k_B}{e}\ln 2$.

In region 2, the leading charge transport mechanism is the hopping of one QD electron to the hot reservoir, which is followed by the addition of one electron from the cold reservoir to the QD. In this case, the change in entropy is $\Delta\mathbb{S} = k_B(\ln 1 - \ln 2) = -k_B \ln 2$ and the spin entropy contribution to the QD thermopower is again $S_{\text{SE}} = -\frac{k_B}{e}\ln 2$, since the reversal of the transport direction introduces an additional change of the sign.

In region 3, the transport is dominated by the same hopping process as it is described for region 1. However, the degeneracies of initial and final state of the QD are interchanged. The entropy change due to the presence of the transported electron is given by $\Delta\mathbb{S} = k_B(\ln 1 - \ln 2) = -k_B \ln 2$, and the SE thermopower is $S_{\text{SE}} = \frac{k_B}{e}\ln 2$.

For region 4, the corresponding analysis yields $\Delta\mathbb{S} = k_B(\ln 2 - \ln 1) = k_B \ln 2$, and $S_{\text{SE}} = \frac{k_B}{e}\ln 2$, where again an additional sign change occurs due to the reversal of the transport direction.

Figure 6.12 summarizes the results of the above discussion. While panel (I) shows the zero-bias conductance and defines the four transport regions (1-4), panels (II-IV) depict the thermoelectric effects. For a better comparison to the experiment, the thermovoltage signal amplitudes ($V_{\text{T}} \propto -S$) are shown in these panels. Panel (II) shows the thermovoltage as it is expected for single electron tunneling including cotunneling effects without spin entropy contributions. Panel (III) gives an estimate of the spin entropy contribution to the thermovoltage signal. The actual contributions may differ from the simplified line shape shown, since the strength of the correlation is not included quantitatively. It is assumed that the correlation effects are strongest in the very close vicinity of the conductance peaks, where the energetic difference between the QD states and the electrons at the Fermi surface is smallest. The combination of panels (II) and (III) is depicted in panel (IV). Note that the superposition of the regular thermovoltage oscillations and the spin entropy contribution results in an amplification of every second maximum and minimum. This is in good agreement with the black curve in Fig. 6.11, where the QD has been adjusted to show an odd-even behavior of alternating spin-degenerate and non-degenerate ground states as a function of the plunger gate voltage. As has been discussed in the previous sections, the measurements of the thermopower of the single QD show that significant additional contributions to the thermopower can be observed in the spin correlated transport regime. These occur predominantly in the vicinity of the positions of the conductance peaks [cf. Fig. 6.11]. Deviations from the theoretically predicted line

shape may result from small asymmetries in the QD-lead system as have been discussed in Chap. 5. The value for the experimentally observed additional thermopower contributions can be estimated to be $|S| \approx 0.5$ mV/10 mK = 50 μV/K, which is close to the theoretical value of $S_{\mathrm{SE}} = 59.7$ μV/K. This leads to the conclusion that the thermoelectric transport in the spin-correlated transport regime in the presence of charge valence fluctuations is mainly spin entropy driven.

Obviously, the above model represents a rather simple qualitative description. For future analysis, a detailed knowledge of the QD ground state configuration is desirable, since theoretical calculations would have to include all the various transport mechanisms. The presented model, however, gives an adequate starting point for the analysis of the thermoelectric transport in the spin-correlated transport regime of QD systems. It has the capability to address questions concerning the entropy transport and entropy production with respect to single bit operations. These questions are of fundamental physical interest due to their close connection to the problem of minimal energy requirements and dissipation in communication, and thus ultimately to the so called "Maxwell's demon" with respect to the second law of thermodynamics. [Ben98, Lan96].

Summary

This thesis presents an experimental study of the thermoelectrical properties of semiconductor quantum dots (QD). The measurements give information about the interplay between first order tunneling and macroscopic quantum tunneling transport effects in the presence of thermal gradients by the direct comparison of the thermoelectric response and the energy spectrum of the QD. The aim of the thesis is to contribute to the understanding of the charge and spin transport in few-electron quantum dots with respect to potential applications in future quantum computing devices. It also gives new insight into the field of low temperature thermoelectricity.

The investigated QDs were defined electrostatically in a two dimensional electron gas (2DEG) formed with a GaAs/(Al,Ga)As heterostructure by means of metallic gate electrodes on top of the heterostructure. Negative voltages with respect to the potential of the 2DEG applied to the gate electrodes were used to deplete the electron gas below them and to form an isolated island of electron gas in the 2DEG which contains a few ten electrons. This QD was electrically connected to the 2DEG via two tunneling barriers. A special electron heating technique was used to create a temperature difference between the two connecting reservoirs across the QD. The resulting thermoelectric voltage was used to study the charge and spin transport processes with respect to the discrete energy spectrum and the magnetic properties of the QD.

Such a two dimensional island usually exhibits a discrete energy spectrum, which is comparable to that of atoms. At temperatures below a few degrees Kelvin, the electrostatic charging energy of the QDs exceeds the thermal activation energy of the electrons in the leads, and the transport of electrons through the QD is dominated by electron-electron interaction effects. The thesis starts by outlining the basic concepts of the electrical and thermoelectrical transport through QD systems as well as the details of the sample design and the experimental techniques.

After the introductory chapters, measurements of the temperature dependent thermopower are presented for the temperature range between 1.5 K and 40 mK. The thermopower of few-electron QDs reveals a transition of the line shape as a function of the QD potential from a full sawtooth to an intermittent sawtooth behavior. Although, the two different line shapes have been observed in previous studies of the thermopower of larger QDs, the results of the present measurements show, for the first time, that both line shapes can occur within the same sample. The comparison of the experimental data

and theoretical model calculations confirms that the transition is directly related to a change in the dominant transport processes. While close to the SET conductance peaks, sequential tunneling processes dominate, the full Coulomb blockaded regime is dominated by elastic and inelastic cotunneling processes. Compared with many-electron or metallic QDs, it turns out that in the present experiments the regime of sequential tunneling is extended over a wider gate voltage range for few-electron QDs. This results in an increasing thermopower peak amplitude with decreasing temperature. Additionally, the analysis reveals that QDs with known energy spectrum can be used as an excellent tool for studying the electron distribution in the 2DEG.

Subsequent to the analysis of the underlying transport behavior, the thesis investigates why the fine structure of low temperature thermopower measurements deviates frequently from the results of idealized model calculations. In this regard, the thermopower as a function of the QD potential has been investigated with respect to certain asymmetries in the QD-lead system. The high sensitivity of the thermopower measurements with respect to the dynamics of the charge transport has revealed that the shape of the tunneling barriers has a significant influence on the thermoelectric transport, especially in the regime of low tunnel barrier heights. In this regime, the transport of electrons from above the Fermi energy of the reservoirs is favored and the thermopower oscillations obtain an offset contribution. It has been found out that this offset is weakly dependent on the potential of the QD and, thus, can be distinguished from other effects.

Furthermore, the effects of an asymmetric coupling of QD states to the contacting reservoirs on the thermoelectric transport have been investigated. High magnetic fields parallel to the plane of the 2DEG have been used to tune the energy states of a QD into a transport regime, where a unidirectional thermoelectric transport in a SET conductance maximum is observable. By using a resonant tunneling model for the charge transport, the nonlinear differential conductance measurements have been directly compared to the thermoelectric signal. The good agreement confirms that the unidirectional thermoelectric transport is a result of an asymmetric transport gap. This gap is induced by the internal symmetry properties of the QD and the spacial configuration of the quantum states. For a corresponding idealized two-level QD system, numerical model calculations show good agreement with these experimental findings. From the observations and the model calculations, it has been inferred that a QD can act as a thermal rectifier. These results imply that in addition to the conventional electronic information processing, information processing based on the rectification of the electronic heat flow is possible in QD systems.

Additionally, these investigations reveal that the asymmetric coupling of QD states to the leads also strongly influences the charge transport via excited states in first and second order tunneling. It is shown that these contributions to the thermoelectric signal can reach up to 30% of the maximum amplitude of the thermopower oscillations. This result explains why a detailed knowledge of the band structure and the impurity levels is necessary in order to understand the complex behavior of the thermopower at very low temperatures.

In order to clarify the role of the magnetic or spin properties of QDs in the thermo-electric transport, the thermopower of a *Kondo* spin-correlated QD has been studied. The spin correlations manifest themselves as a zero-bias resonance in the finite-bias differential conductance measurements. The temperature dependence of the conductance and the magnetic field induced chessboard pattern in the measurement of the Coulomb blockade oscillations have been used to identify the thermoelectric signature of the spin-correlated transport. In this regime, clear deviations from the semiclassical single particle Mott relation between thermopower and conductance have been observed. This is interpreted as a clear sign of the underlying many-particle nature of the correlated transport process. The observed strong thermopower contributions indicate a significant asymmetry in the spectral density of states of the spin-correlated state with respect to the Fermi energies of the reservoirs. The measurements agree well with theoretical considerations, which address the evolution of the thermopower as a function of the QD energy. The results presented here confirm that the spectral density of states for the spin correlations of a QD can be explained in the framework of an Anderson impurity model in the presence of charge valence fluctuations.

Generally speaking, the measurements clarify the overall line shape of thermopower oscillations and the observed fine structure as well as additional spin effects in the ther-moelectrical transport. The observations demonstrate that it is possible to control and optimize the strength and direction of the electronic heat flow on the scale of a single im-purity and create spin-correlated thermoelectric transport in nanostructures, where the experimenter has a close control of the exact transport conditions. The results support the assumption that the performance of thermoelectric devices can be enhanced by the adjustment of the QD energy levels and by exploiting the properties of the spin-correlated charge transport via localized, spin-degenerate impurity states. Within this context, spin entropy has been identified as a driving force for the thermoelectric transport in the spin-correlated transport regime in addition to the kinetic contributions. Fundamental considerations, which are based on simple model assumptions, suggest that spin entropy plays an important role in the presence of charge valence fluctuations in the QD. The presented model gives an adequate starting point for future quantitative analysis of the thermoelectricity in the spin-correlated transport regime. These future studies might cover the physics in the limit of single electron QDs or the physics of more complex struc-tures such as QD molecules as well as QD chains. In particular, it should be noted that the experimental investigations of the thermopower of few-electron QDs address questions concerning the entropy transport and entropy production with respect to single-bit infor-mation processing operations. These questions are of fundamental physical interest due to their close connection to the problem of minimal energy requirements in communication, and thus ultimately to the so called "Maxwell's demon" with respect to the second law of thermodynamics.

Zusammenfassung

Diese Dissertation präsentiert eine experimentelle Studie über die thermoelektrischen Eigenschaften von Halbleiterquantenpunkten. Das thermoelektrische Verhalten der Quantenpunkte wird unter besonderer Berücksichtigung ihrer jeweiligen Energiespektren und magnetischen bzw Spin-Eigenschaften diskutiert. Die durchgeführten Messungen geben Aufschluss über das Zusammenspiel von Einzelelektronentunnelprozessen erster und höherer Ordnung unter dem Einfluss thermischer Gradienten. Somit trägt diese Dissertation zum Verständnis des Ladungs- und Spintransports in potentiellen, zukünftigen Bausteinen für die Quanteninformationsverarbeitung bei und ermöglicht neue Einblicke in das Themengebiet der Thermoelektrizität bei sehr tiefen Temperaturen.

Die untersuchten Quantenpunkte wurden in einem zweidimensionalen Elektronengas (2DEG) mittels nanostrukturierter, metallischer „gates" erzeugt, die auf der Oberfläche einer GaAs/AlGaAs Heterostrukturoberfläche aufgebracht wurden. Durch das Anlegen negativer Spannungen in Bezug auf das Potential des 2DEGs, wurde das Elektronengas unter den gates verdrängt, so dass eine isolierte Insel entstand, die bis zu ca. 30 Elektronen zählte. Zwei Tunnelbarrieren dienten als elektrische Verbindung dieses Quantenpunkts zu den Zuleitungen. Unter Verwendung einer speziellen Stromheizungstechnik wurde eine Temperaturdifferenz zwischen den zwei Zuleitungsreservoirs über dem Quantenpunkt erzeugt. Die Untersuchung von Ladungs- und Spintransportprozessen erfolgte über den direkten Vergleich der resultierenden thermoelektrischen Spannung mit den jeweiligen Energiespektren der Quantenpunkte.

Im Allgemeinen weist eine solche zweidimensionale Insel ein diskretes Energiespektrum auf, das vergleichbar mit dem einzelner Atome ist. Unterhalb einer Temperatur von wenigen Grad Kelvin, ist die elektrostatische Aufladungsenergie des Quantenpunkts größer als die thermische Anregungsenergie der Elektronen in den Zuleitungen. Als Folge bestimmen Elektron-Elektron-Wechselwirkungseffekte den Transport von Elektronen durch den Quantenpunkt. Ein einführender Überblick über diese grundlegenden Konzepte des elektrischen und thermoelektrischen Transports durch Quantenpunktsysteme sowie die experimentellen Techniken wird in den einleitenden Kapiteln geben.

Im Anschluss werden Messungen zur Temperaturabhängigkeit der thermoelektrischen Kraft (Thermokraft) im Temperaturbereich zwischen 1,5 K und 40 mK diskutiert. Die Thermokraft von Quantenpunkten mit nur wenigen Elektronen zeigt in ihrem Verlauf als Funktion des Quantenpunktpotentials einen Übergang von einem sich wiederholenden

Sägezahnprofil bei hohen Temperaturen, in diesem Fall 1,5 K, zu einem periodisch unterbrochenen Sägezahnprofil bei tiefen Temperaturen. Obwohl diese zwei unterschiedlichen Linienformen in vorangegangenen Untersuchungen an größeren Quantenpunkten bereits beobachtet wurden, gaben die durchgeführten Messungen zum ersten Mal zu erkennen, dass beide Linienformen in ein und derselben Probe auftreten können. Zudem wurde nachgewiesen, dass der Übergang eine Konsequenz aus der Änderung der dominierenden Transportprozesse ist. Während in der Nähe der Leitwertsmaxima, welche durch das Einzelelektronentunneln hervorgerufen werden, sequentielles Tunneln vorherrscht, dominieren elastische und inelastische Cotunnelprozesse im Bereich der vollständigen Coulombblockade. Im Gegensatz zu Vielelektronenquantenpunkten, sog. metallischen Quantenpunkten, hat sich in diesen Experimente herausgestellt, dass sich das Regime des sequentiellen Tunnelns bei Quantenpunkten, die nur wenige Elektronen zählen, über einen erweiterten Bereich der Elektrodenspannung erstreckt. Dies führt zu einer ansteigenden Amplitude der Extrema der Thermokraft mit einhergehender Temperaturabnahme. Darüberhinaus folgt aus der Analyse der Messdaten, dass Quantenpunkte, deren Energiespektrum im Detail bekannt ist, ein überaus geeignetes Mittel zur Untersuchung der Elektronenverteilung im 2DEG darstellen.

Ausgehend von dieser Analyse der zugrunde liegenden Transporteigenschaften wird in der Dissertation die Frage erläutert, aus welchem Grund die Feinstruktur der Tieftemperaturmessungen der Thermokraft in einer Vielzahl von Messungen von den Ergebnissen der Modellrechnungen abwich. Zu diesem Zwecke wurde die Thermokraft als Funktion des Quantenpunktpotentials hinsichtlich möglicher Asymmetrien im Quantenpunktsystem untersucht.

Die hohe Empfindlichkeit der Thermokraftmessungen bezüglich der Dynamik des Ladungstransports hat zum Vorschein gebracht, dass im Regime niedriger Tunnelbarrieren die Thermokraftoszillationen einen Untergrundbeitrag enthalten, der schwach vom Potential des Quantenpunkts abhängt. Dieser Beitrag wurde der Form der Tunnelbarrieren zugeschrieben, welche den Transport von Elektronen oberhalb der Fermienergie der Zuleitungen begünstigt.

Darüber hinaus wurden Messungen vorgestellt, die es erlaubten das Zusammenspiel von Quantenpunktzuständen zu untersuchen, welche symmetrisch bzw. asymmetrisch an die Zuleitungen gekoppelt wurden. Hohe Magnetfelder parallel zur Ebene des 2DEGs wurden verwendet um die Quantenpunktzustände in ein Transportregime einzustellen, in dem ein nur in eine Richtung gerichteter thermoelektrischer Transport in einem Leitwertsmaximum des Einzelelektronentunnels beobachtbar war. Basierend auf ein Modell, das einen resonanten Ladungstransport betrachtet, konnte der nicht-lineare differentielle Leitwert direkt mit dem Thermospannungssignal verglichen werden. Die gute Übereinstimmung bestätigte, dass der unidirektionale thermoelektrische Transport die Folge einer asymmetrischen Transportlücke war. Diese Lücke wurde durch die internen Symmetrieeigenschaften des Quantenpunkts und der räumlichen Anordnung seiner quantenmechanischen Zustände bestimmt. Numerische Berechnungen für ein Zwei-Niveau Quantenpunktsystem

zeigten eine sehr gute Übereinstimmung mit diesen experimentellen Ergebnissen. Aus diesen Beobachtungen und den Modellrechnungen folgt, dass ein Quantenpunkt als thermischer Gleichrichter agieren kann. Aus diesen neuen Ergebnissen folgt, dass zusätzlich zur bekannten elektronischen Informationsverarbeitung, eine Informationsverarbeitung beruhend auf dem Prinzip der Gleichrichtung des elektronischen Wärmeflusses möglich ist.

Desweiteren wurde durch diese Untersuchungen deutlich gezeigt, dass das asymmetrische Koppeln von Quantenpunktzuständen zu den Zuleitungen den Ladungstransport über angeregte Zustände bei Tunnelprozessen erster und zweiter Ordnung ebenfalls stark beeinflusst. Es hat sich herausgestellt, dass diese Beiträge zum thermoelektrischen Signal bis zu 30% der maximalen Amplitude der Thermokraftoszillationen erreichen kann. Dieses Ergebnis erklärt, weshalb eine detaillierte Kenntnis der Bandstruktur und der Energiezustände von Verunreinigungen notwendig ist, um das komplexe Verhalten der Thermokraft bei tiefen Temperaturen zu verstehen.

Um die Rolle der magnetischen bzw. Spineigenschaften von Quantenpunkten im thermoelektrischen Transport zu klären, wurde die Thermokraft eines Spin-korrelierten Quantenpunkts untersucht. Die Spinkorrelationen äußern sich in den Messungen des differentiellen Leitwerts als zusätzliche Resonanz, wenn keine Vorspannung am Quantenpunkt anliegt. Die Temperaturabhängigkeit des Leitwerts und das magnetfeldinduziertes Schachbrettmuster in den Coulombblockadeoszillationen wurden verwendet, um das Regime des Spin-korrelierten Transports zu identifizieren. In der Gegenwart von Spinkorrelationen wurde eine offensichtliche Abweichung von der semiklassischen Mott-Beziehung für Ein-Teilchensysteme zwischen dem Leitwert und der Thermokraft beobachtet. Dies wird als klares Zeichen der zugrunde liegenden Viel-Teilchennatur des korrelierten Transportprozesses interpretiert. Die beobachteten, starken Beiträge zur Thermokraft weisen auf eine ausgesprochene Asymmetrie der spektralen Zustandsdichte des Spin-korrelierten Zustands bezüglich der Fermi-Energien der Reservoirs hin. Die Messungen stimmen mit theoretischen Überlegungen überein, die das Verhalten der Thermokraft als Funktion der Quantenpunktenergie behandeln. Dabei bestätigen die gezeigten Ergebnisse, dass die spektrale Zustandsdichte der Spinkorrelationen eines Quantenpunkts im Rahmen eines Anderson-Störstellenmodells bei vorhandenen Fluktuationen der Valenzladungen des Quantenpunkts beschrieben werden kann.

Allgemein betrachtet, erklären die durchgeführten Messungen den Verlauf der Thermokraft als Funktion des Quantenpunktpotentials einschließlich der aufgeprägten Feinstruktur sowie zusätzliche thermoelektrische Effekte, die von den Spin-Eigenschaften des Quantenpunkts hervorgerufen werden. Die Beobachtungen beweisen, dass es möglich ist Stärke und Richtung des elektronischen Wärmeflusses auf der Größenskala einzelner Verunreinigungen zu kontrollieren und gegebenenfalls zu optimieren sowie Spin-korrelierten thermoelektrischen Transport in künstlich hergestellten Nanostrukturen zu verwirklichen, welche eine gezielte Kontrolle der Transportbedingungen erlauben. Die Ergebnisse untermauern die Annahmen einer möglichen Verbesserung der Effizienz thermoelektrisch

aktiver Materialien durch die Anpassung der energetischen Lage entsprechender Quantenpunktzustände und durch die Ausnutzung der thermoelektrischen Effekte im Spin-korrelierten Ladungstransport durch energetisch entartete, lokalisierte Zustände. In diesem Rahmen wurde erläutert, dass Spinentropie neben den kinetischen Beiträgen eine weitere treibende Kraft des thermoelektrischen Transports durch Quantenpunkte darstellt. Grundlegende Überlegungen, die auf einfachen Modellannahmen beruhen, lassen erwarten, dass die Beiträge der Spinentropie zum thermoelektischen Transport bei vorhandenen Fluktuationen der Anzahl der Ladungen auf dem Quantenpunkt eine signifikante Rolle spielen. Das vorgestellte Modell bietet hierzu einen geeigneten Ausgangspunkt für weitere quantitative Analysen der Thermoelektrizität im Spin-korrelierten Transportregime. Diese zukünftigen Untersuchungen sollten sich voraussichtlich mit der Physik von Ein-Elektron-Quantenpunkten oder Strukturen höherer Komplexität, wie z.B. Quantenpunktmolekülen oder Kettenstrukturen, bestehend aus Quantenpunkten, befassen. Insbesondere sei darauf hingewiesen, dass die experimentelle Untersuchung der Thermokraft von Quantenpunktstrukturen, wie sie hier verwendet wurden, den Entropietransport und die Entropieerzeugung in Bezug zu Ein-Bit-Rechenoperationen setzen. Fragestellungen dieser Art sind von fundamentalem physikalischen Interesse aufgrund ihrer engen Verknüpfung mit der Frage nach dem minimalen Energieaufwand, der eine Kommunikation ermöglicht. Dieses Problem wird häufig mittels des so genannten Maxwell'schen Dämon diskutiert und hinterfragt in ihrem Ursprung den zweiten Hauptsatz der Thermodynamik.

Appendix A

Sample information

The table lists the layer sequence of the (Ga,Al)As heterostructure, which was used for the fabrication of samples *Bochum I4A* and *Bochum I13C*. The electron density n_{He} and the mobility μ_{He} are the nominal values given on the data sheet for the 2DEG heterostructure. These values may differ from the values obtained form the actual samples. Especially the mobility turned out to be very sensitive to the cooling procedure from room temperature to below 77 K. Best stability of the QDs was obtained for cooling with an applied gate voltage bias of +0.2 V with respect to the potential of the 2DEG.

Wafer Samples	Bo-11189 : Bochum I4A, Bochum I13C	
Layer	Thickness (nm)	Material
cover layer	5.0	GaAs:Si
donor layer	$26.0 + 4.0 + \text{Si-}\delta$	$\text{Al}_{0.32}\text{Ga}_{0.68}\text{As}$
spacer layer	35	$\text{Al}_{0.32}\text{Ga}_{0.68}\text{As}$
buffer	600	GaAs
	$n_{He} = 1.41 \times 10^{11} \text{ cm}^{-2}$	Si-δ doping
	$\mu_{He} = 2.29 \ 10^{6} \text{ cm}^{2}/\text{Vs}$	

direction of growth

cover layer

donor layer

spacer layer

2DEG

buffer

substrate

Appendix B

Cryogenic filtering

Below temperatures of a few 100 mK, the 2DEG decouples from the lattice due to the strongly reduced electron phonon interaction. Thus, accurate electronic measurements of single electron tunneling devices require an appropriate filtering of the connecting wires into the cryostat in order to reduce thermal noise and noise from other sources in the environment which would heat up the electronic system. Proper shielding and, especially, low temperature filtering is of special importance, since even the black body radiation of 4 K photons is enough to heat up the sample [VOJ+95]. A comparison of various cryogenic filters can be found in Ref. [BGH+03] and Ref. [CBCP95]. Most of these filters act as so called lossy lines which employ the high capacity and resistance of the lines going to the sample as an RC-filter. Here, it should be noted that this filtering technique sets limitations to the measurement of the thermovoltage of quantum dots. The capacity of the wiring and the high impedance of the quantum dot in the Coulomb blockade regime act as a very efficient RC-filter which attenuates the frequency modulated thermovoltage signal as it has been described in Chap. 3.2.3. Depending on which transport regime is investigated, e.g. the regime of strong coupling or the regime of a very weak coupling, respectively, the capacity of the line filters has to be chosen adequately. Thus, in the limit of a very high QD impedance, a trade-off has to be made between the electron temperature and the accuracy of the measurement in the fully Coulomb blockaded transport regime. Figure B.1 shows a 3-D projection of the bottom part of the sample holder which has been built for the 18-Tesla Leiden cryogenics dilution cryostat unit which is a bottom loading system. According to the constraints of the investigated QD system and the geometry of the dilution unit, the capacity of one of the Thermocoax® cables has been chosen to be approximately 200 pF at cryogenic temperatures.
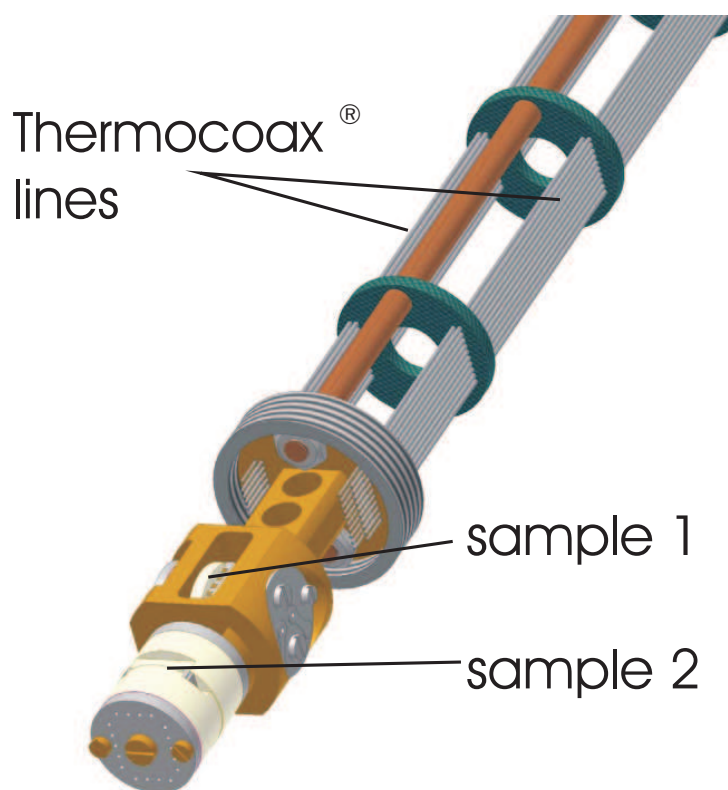
Fig. B.1: Technical sketch of the sample holder for the bottom loading cryostat. Here, the wiring is made of approximately 45 cm of Thermocoax® cables with an outer diameter of 1 mm. This filter stage is located below the cryostat cold plate and is thermally anchored to the mixing chamber. The sample holder allows two samples to be measured at the same time; sample 1 is oriented parallel to the direction of the magnetic field, sample 2 is oriented perpendicular to the magnetic field direction.

Bibliography

[AL91]   D.V. Averin and K.K. Likharev, *Mesoscopic Phenomena in Solids*, Else-vier, Amsterdam, 1991.

[AM98]   I.G. Austin and N.F. Mott, *Polarons in crystalline and non-crystalline materials*, Advances in Physics **18** (1998), no. 71, 41–102.

[AM01]   I.G. Austin and N.F. Mott, *Polarons in crystalline and non-crystalline materials*, Advances in Physics **50** (2001), no. 7, 757–812.

[AN90]   D.V. Averin and Yu.V. Nazarov, *Virtual electron diffusion during quantum tunneling of the electric charge*, Phys. Rev. Lett. **65** (1990), no. 19, 2446–2449.

[And61]   P.W. Anderson, *Localized Magnetic States in Metals*, Phys. Rev. **124** (1961), no. 1, 41–53.

[ANP+00]   N.J. Appleyard, J.T. Nicholls, M. Pepper, W.R. Tribe, M.Y. Simmons, and D.A. Ritchie, *Direction-resolved transport and possible many-body effects in one-dimensional thermopower*, Phys. Rev. B **62** (2000), no. 24, R16275–R16278.

[ANS+98]   N.J. Appleyard, J.T. Nicholls, M.Y. Simmons, W.R. Tribe, and M. Pepper, *Thermometer for the 2D Electron Gas using 1D Thermopower*, Phys. Rev. Lett. **81** (1998), no. 16, 3491–3494.

[Bar72]   R.D. Barnard, *Thermoelectricity in metals and alloys*, Taylor and Francis LTD, London, 1972.

[Bee91]   C.W.J. Beenakker, *Theory of Coulomb-blockade oscillations in the conductance of a quantum dot*, Phys. Rev. B **44** (1991), no. 4, 1646–1656.

[Ben74]   G. Beni, *Thermoelectric power of the narrow-band Hubbard chain at arbitrary electron density: Atomic limit*, Phys. Rev. B **10** (1974), no. 6, 2186–2189.

[Ben98]   C.H. Bennett, *Information physics in cartoons*, Superlattices and Microstructures **23** (1998), no. 3/4, 367–372.

[BF01]   D. Boese and R. Fazio, *Thermoelectric effects in Kondo-correlated quantum dots*, Europhys. Lett. **56** (2001), no. 4, 576–582.

[BGH+03]   K.F Bladh, D. Gunnarsson, E. Hürfeld, S. Devi, C. Kristoffersson, B. Sma-lander, S. Pehrson, T. Claeson, P. Delsing, and M. Taslakov, *Comparison of cryogenic filters for use in single electronics experiments*, Rev. Sci. Instr. **74** (2003), no. 3, 1323–1327.

[BGM+95]   V. Bayot, E. Grivei, H. C. Manoharan, X. Ying, and M. Shayegan, *Thermopower of composite fermions*, Phys. Rev. B **52** (1995), no. 12, R8621–R8624.

[BILP85]   M. Büttiker, Y. Imry, R. Landauer, and S. Pinhas, *Generalized many-channel conductance formula with application to small rings*, Phys. Rev. B **31** (1985), no. 10, 6207–6215.

[BimcVC95]   N. Balkan, H. Çelik, A.J. Vickers, and M. Cankurtaran, *Warm-electron power loss in $GaAs/Ga_{1-x}Al_xAs$ multiple quantum wells: Well-width dependence*, Phys. Rev. B **52** (1995), no. 24, 17210–17222.

[BS92]   C.W.J. Beenakker and A.A.M. Staring, *Theory of the thermopower of a quantum dot*, Phys. Rev. B **46** (1992), no. 15, 9667–9676.

[Büt86]   M. Büttiker, *Four-Terminal Phase-Coherent Conductance*, Phys. Rev. Lett. **57** (1986), no. 14, 1761–1764.

[But90]   P.N. Butcher, *Thermal and electrical transport formalism for electronic microstructures with many terminals*, J. Phys.: Condens. Matter **2** (1990), 4869–4878.

[BvH91]   C.W.J. Beenakker and H. van Houten, *Quantum transport in semiconductor nanostructures*, Solid State Physics **44** (1991), 1.

[CB76]   P.M. Chaikin and G. Beni, *Thermopower in the correlated hopping regime*, Phys. Rev. B **13** (1976), no. 2, 647–651.

[CB86]   D.G. Cantrell and P.N. Butcher, *A calculation of the phonon drag contribution to thermopower in two dimensional systems*, J. Phys. C **19** (1986), no. 20, L429–L432.

[CBCP95]   H. Courtois, O. Buisson, J. Chaussy, and B. Pannetier, *Miniature low-temperature high-frequency filters for single electronics*, Rev. Sci. Instr. **66** (1995), no. 6, 3465–3468.

[CHZ94]   T.A. Costi, A.C. Hewson, and V. Zlatic, *Transport coefficients of the Anderson model via the numerical renormalization group*, Journal of Physics: Condensed Matter **6** (1994), no. 13, 2519–2558.

[CKE79]   P.M. Chaikin, J.F. Kwak, and A.J. Epstein, *Evidence for Strong Coulomb Correlations in an Organic Conductor*, Phys. Rev. Lett. **42** (1979), no. 17, 1178–1182.

[COK98]   S.M. Cronenwett, T.H. Oosterkamp, and L.P. Kouwenhoven, *A Tunable Kondo Effect in Quantum Dots*, Science **281** (1998), no. 5376, 540–544.

[COMZ06]   C.W. Chang, D. Okawa, A. Majumdar, and A. Zettl, *Solid-State Thermal Rectifier*, Science **314** (2006), no. 5802, 1121–1124.

[CSH+00]   M. Ciorga, A.S. Sachrajda, P. Hawrylak, C. Gould, P. Zawadzki, S. Jullian, Y. Feng, and Z. Wasilewski, *Addition spectrum of a lateral dot from Coulomb and spin-blockade spectroscopy*, Phys. Rev. B **61** (2000), no. 24, R16315–R16318.

[Dar30]   C.G. Darwin, *The diamagnetism of the free electron*, Proc. Cambridge Philos. Soc. Math. Phys. Sci. **27** (1930), 86.

[DFHvdW+02]   S. De Franceschi, R. Hanson, W.G. van der Wiel, J.M. Elzerman, J.J. Wijpkema, T. Fujisawa, S. Tarucha, and L.P. Kouwenhoven, *Out-of-Equilibrium Kondo Effect in a Mesoscopic Device*, Phys. Rev. Lett. **89** (2002), no. 15, 156801–156804.

[DFSE+01]   S. De Franceschi, S. Sasaki, J.M. Elzerman, W.G. van der Wiel, S. Tarucha, and L.P. Kouwenhoven, *Electron Cotunneling in a Semiconductor Quantum Dot*, Phys. Rev. Lett. **86** (2001), no. 5, 878–881.

[dG63]   S.R. de Groot, *Thermodynamics of irreversible processes*, North-Holland Publ., Amsterdam, 1963.

[DGGW+00]   D.S. Duncan, D. Goldhaber-Gordon, R.M. Westervelt, K.D. Maranowski, and A.C. Gossard, *Coulomb-blockade spectroscopy on a small quantum dot in a parallel magnetic field*, Applied Physics Letters **77** (2000), no. 14, 2183–2185.

[DiS99]   F.J. DiSalvo, *Thermoelectric Cooling and Power Generation*, Science **285** (1999), 703–706.

[DL02]   B. Dong and X.L. Lei, *Effect of the Kondo correlation on the thermopower in a quantum dot*, Journal of Physics: Condensed Matter **14** (2002), no. 45, 11747–11756.

[DLS95]   J.H. Davies, I.A. Larkin, and E.V. Sukhorukov, *Modeling the patterned two-dimensional electron gas: Electrostatics*, J. Appl. Phys. **77** (1995), no. 9, 4504–4512.

[DMTG02]   C.F. Destefani, G.E. Marques, and C. Trallero-Giner, *Transport properties in spherical quantum dots: Orbital-blockade and spin-blockade effects*, Phys. Rev. B **65** (2002), no. 23, 235314–235324.

[DSB+97]   A.S. Dzurak, C.G. Smith, C.H.W. Barnes, M. Pepper, L. Martín-Moreno, C.T. Liang, D.A. Ritchie, and G.A.C. Jones, *Thermoelectric signature of the excitation spectrum of a quantum dot*, Phys. Rev. B **55** (1997), no. 16, R10197–R10200.

[DSB+98]   A.S. Dzurak, C.G. Smith, C.H.W. Barnes, M. Pepper, L. Mart'in-Moreno,
              C.T. Liang, D.A. Ritchie, and G.A.C. Jones, *Thermopower measurements
              of semiconductor quantum dots*, Physica B: Condensed Matter **249–251**
              (1998), 281–285.

[EHG+03]   J.M. Elzerman, R. Hanson, J.S. Greidanus, L.H. Willems van Beveren,
              S. De Franceschi, L.M.K. Vandersypen, S. Tarucha, and L.P. Kouwen-
              hoven, *Few-electron quantum dot circuit with integrated charge read out*,
              Phys. Rev. B **67** (2003), no. 16, 161308–161312.

[EHWvB+04]   J.M. Elzerman, R. Hanson, L.H. Willems van Beveren, B. Witkamp,
              L.M.K. Vandersypen, and L.P. Kouwenhoven, *Single-shot read-out of an
              individual electron spin in a quantum dot*, Nature **430** (2004), no. 6998,
              431–435.

[FDS+88]   R. Fletcher, M. D'Iorio, A.S. Sachrajda, R. Stoner, C.T. Foxon, and
              J.J. Harris, *Evidence of phonon drag in the thermopower of a GaAs-
              $Ga_{0.68}Al_{0.32}As$ heterojunction*, Phys. Rev. B **37** (1988), no. 6, 3137–3140.

[FKH+02]   C. Fühner, U.F. Keyser, R.J. Haug, D. Reuter, and A. D. Wieck, *Flux-
              quantum-modulated Kondo conductance in a multielectron quantum dot*,
              Phys. Rev. B **66** (2002), no. 16, 161305–161309.

[FMM+93]   E.B. Foxman, P.L. McEuen, U. Meirav, N.S. Wingreen, Y. Meir, P.A.
              Belk, N.R. Belk, M.A. Kastner, and S.J. Wind, *Effects of quantum levels
              on transport through a Coulomb island*, Phys. Rev. B **47** (1993), no. 15,
              10020–10023.

[Foc28]   V. Fock, *Bemerkung zur Quantelung des harmonischen Oszillators im
              Magnetfeld*, Zeitschrift für Physik A **47** (1928), no. 5–6, 446–448.

[GAM90]   L.J. Geerligs, D.V. Averin, and J.E. Mooij, *Observation of macroscopic
              quantum tunneling through the Coulomb energy barrier*, Phys. Rev. Lett.
              65 (1990), no. 24, 3037–3040.

[GBJB95]   G.D. Guttman, E. Ben-Jacob, and D.J. Bergman, *Thermopower of meso-
              scopic and disordered systems*, Phys. Rev. B **51** (1995), no. 24, 17758–
              17766.

[GGB+06]   F. Giazotto, T. Galloway, P. Beton, J.P. Oxley, S.P. Beaumont, S. Thoms,
              and C.D.W. Wilkinson, *Opportunities for Mesoscopics in Thermometry
              and Refrigeration: Physics and Applications*, Rev. Mod. Phys. **78** (2006),
              217–275.

[GGSAM+98]   D. Goldhaber-Gordon, H. Shtrikman, D. Abusch-Magder, U. Meirav, and
              M.A. Kastner, *Kondo effect in a single-electron transistor*, Nature **391**
              (1998), 156–159.

[GHL$^+$90]   B.L. Gallagher, T.T. Heikkilä, A. Luukanen, A.M. Savin, and J.P. Pekola, *Observation of universal thermopower fluctuations*, Phys. Rv. Lett. **64** (1990), no. 17, 2058–2061.

[GJ82]   S.M. Girvin and M. Jonson, *Inversion layer thermopower in high magnetic field*, J. Phys. C: Solid State Phys. **15** (1982), no. 32, L1147–L1151.

[GMB$^+$99]   S.F. Godijn, S. Möller, H. Buhmann, L.W. Molenkamp, and S.A. van Langen, *Thermopower of a chaotic quantum dot*, Phys. Rev. Lett. **82** (1999), no. 14, 2927.

[Gor51]   C.J. Gorter, *A possible explanation of the increase of the electrical resistance of thin metal films at low temperatures and small field strengths*, Physica **17** (1951), 777–780.

[GP03]   L.I. Glazman and M. Pustilnik, *New directions in mesoscopic physics: Coulomb blockade and Kondo effect in quantum dots*, Kluwer, Dordrecht, 2003.

[GQ82]   G.F. Giuliani and J.J. Quinn, *Lifetime of a quasiparticle in a two-dimensional electron gas*, Phys. Rev. B **26** (1982), no. 8, 4421–4428.

[GR88]   L.I. Glazman and M.É. Raikh, *Resonant kondo transparency of a barrier with quasilocal impurity states*, JETP **47** (1988), no. 8, 452–455.

[Hal78]   F.D.M. Haldane, *Scaling Theory of the Asymmetric Anderson Model*, Phys. Rev. Lett. **40** (1978), no. 6, 416–419.

[Hei61]   R.R. Heikes, *Thermoelectricity*, New York, Interscience, 1961.

[Hew93]   A.C. Hewson, *The Kondo Problem to Heavy Fermions*, Cambridge University Press, Cambridge, England, 1993.

[HTT92]   A.E. Hanna, M.T. Tuominen, and M. Tinkham, *Observation of elastic macroscopic quantum tunneling of the charge variable*, Phys. Rev. Lett. **68** (1992), no. 21, 3228–3231.

[HWM96]   L.D. Hallam, J. Weis, and P.A. Maksym, *Screening of the electron-electron interaction by gate electrodes in semiconductor quantum dots*, Phys. Rev. B **53** (1996), no. 3, 1452–1462.

[ISS98]   W. Izumida, O. Sakai, and Y. Shimizu, *Kondo effect in single quantum dot systems*, J. Phys. Soc. Jpn. **67** (1998), no. 7, 2444–2454.

[JG84]   M. Jonson and S. M. Girvin, *Thermoelectric effect in a weakly disordered inversion layer subject to a quantizing magnetic field*, Phys. Rev. B **29** (1984), no. 4, 1939–1946.

[JHKvdZ+05] P. Jarillo-Herrero, J. Kong, H.S.J. van der Zant, C. Dekker, L.P. Kouwen-hoven, and S. De Franceschi, *Orbital Kondo effect in carbon nanotubes*, Nature **434** (2005), no. 7032, 484–488.

[KBC76] J.F. Kwak, G. Beni, and P.M. Chaikin, *Thermoelectric power in Hubbard-model systems with different densities: N-methylphenazinium-tetracyanoquinodimethane (NMP-TCNQ), and quinolinium ditetra-cyanoquinodimethane*, Phys. Rev. B **13** (1976), no. 2, 641–646.

[KBM00] J.J. Koonen, H. Buhmann, and L.W. Molenkamp, *Probing the Potential Landscape Inside a Two-Dimensional Electron Gas*, Phys. Rev. Lett. **84** (2000), no. 11, 2473–2476.

[KBT+06] F.H.L. Koppens, C. Buizert, K.J. Tielrooij, I.T. Vink, K.C. Nowack, T. Meunier, L.P. Kouwenhoven, and L.M.K. Vandersypen, *Driven co-herent oscillations of a single electron spin in a quantum dot*, Nature **442** (2006), no. 7104, 766–771.

[KDP80] K. v. Klitzing, G. Dorda, and M. Pepper, *New Method for High-Accuracy Determination of the Fine-Structure Constant Based on Quantized Hall Resistance*, Phys. Rev. Lett. **45** (1980), no. 6, 494–497.

[Kel01] M. Keller, *Der Kondo-Effekt in Quantumdots bei hohen Magnetfeldern*, Ph.D. thesis, Max-Planck-Institut für Festkörperforschung, Stuttgart, 2001.

[KFB+03] U.F. Keyser, C. Fühner, S. Borck, R.J. Haug, M. Bichler, G. Abstreiter, and W. Wegscheider, *Kondo Effect in a Few-Electron Quantum Ring*, Phys. Rev. Lett. **90** (2003), no. 19, 196601–196604.

[KK06] B. Kubala and J. König, *Quantum-fluctuation effects on the thermopower of a single-electron transistor*, Phys. Rev. B **73** (2006), 195316–195325.

[KKM03] M.N. Kiselev, K. Kikoin, and L.W. Molenkamp, *Resonance Kondo tunnel-ing through a double quantum dot at finite bias*, Phys. Rev. B **68** (2003), no. 15, 155323–155331.

[KM01] W. Koshibae and S. Maekawa, *Effects of Spin and Orbital Degeneracy on the Thermopower of Strongly Correlated Systems*, Phys. Rev. Lett. **87** (2001), no. 23, 236603–236606.

[KMM+97] L.P. Kouwenhoven, C.M. Marcus, P.L. McEuen, S. Tarucha, R.M. West-ervelt, and N.S. Wingreen, *Mesoscopic electron transport*, vol. 345, Kluwer Academic, Dordrecht, 1997.

[KNY+98] T.A. Knuuttila, K.K. Nummila, W. Yao, J.P. Kauppinen, and J.P. Pekola, *Direct measurement of electron thermalization in Coulomb blockade nan-othermometres at millikelvin temperatures*, Physica E **3** (1998), no. 4, 224–228.

[Kon64]   J. Kondo, *Resistance minimum in dilute magnetic alloys*, Progress of Theoretical Physics **32** (1964), no. 1, 37–49.

[KS75]   I.O. Kulik and R.I. Shekhter, *Kinetic phenomena and charge discreteness effects in granulated media*, Soviet Physics JETP **41** (1975), 308.

[KTM00]   W. Koshibae, K. Tsutsui, and S. Maekawa, *Thermopower in cobalt oxides*, Phys. Rev. B **62** (2000), no. 11, 6869–6872.

[KWS$^+$01]   M. Keller, U. Wilhelm, J. Schmid, J. Weis, K. v. Klitzing, and K. Eberl, *Quantum dot in high magnetic fields: Correlated tunneling of electrons probes the spin configuration at the edge of the dot*, Phys. Rev. B **64** (2001), no. 3, 033302–033305.

[Lan57]   R. Landauer, *Spatial variation of currents and fields due to localized scatterers in metallic conduction*, IBM J. Res. Dev. **1** (1957), 223.

[Lan70]   R. Landauer, *Electrical resistance of disordered one-dimensional lattices*, Philos. Mag. **21** (1970), no. 172, 863–867.

[Lan96]   R. Landauer , *Minimal Energy Requirements in Communication*, Science **272** (1996), no. 5270, 1914–1918.

[LD98]   D. Loss and D.P. DiVincenzo, *Quantum computation with quantum dots*, Phys. Rev. A **57** (1998), no. 1, 120–126.

[LF05]   A.M. Lunde and K. Flensberg, *On the Mott fromula for the thermopower of non-interacting electrons in quantum point contacts*, J. Phy.: Condens. Matter **17** (2005), 3879–3884.

[LIH$^+$02]   S. Lindemann, T. Ihn, T. Heinzel, W. Zwerger, K. Ensslin, K. Maranowski, and A. C. Gossard, *Stability of spin states in quantum dots*, Phys. Rev. B **66** (2002), no. 19, 195314–195324.

[LNHF89]   D.R. Leadley, R.J. Nicholas, J.J. Harris, and C.T. Foxon, *Cyclotron phonon emission and electron energy loss rates in GaAs-GaAlAs heterojunctions*, Semicond. Sci. Technol. **4** (1989), no. 10, 879–884.

[LS94]   I.A. Larkin and E.V. Sukhorukov, *Method to investigate the random potential in a quantum point contact*, Phys. Rev. B **49** (1994), no. 8, 5498–5507.

[Lyo84]   S.K. Lyo, *High-magnetic-field thermopower in a layered superlattice*, Phys. Rev. B **30** (1984), no. 6, 3257–3260.

[MAE$^+$87]   S.J. Manion, M. Artaki, M.A. Emanuel, J.J. Coleman, and K. Hess, *Electron-energy-loss rates in $Al_xGa_{1-x}As/GaAs$ heterostructures at low temperatures*, Phys. Rev. B **35** (1987), no. 17, 9203–9208.

[Mah81]   G.D. Mahan, *Many particle physics*, Plenum Press, New York, 1981.

[MBGM98] S. Möller, H. Buhmann, S.F. Godijn, and L.W. Molenkamp, *Charging energy of o chaotic quantum dot*, Phys. Rev. Lett. **81** (1998), no. 23, 5197–5200.

[MFK+92] P.L. McEuen, E.B. Foxman, J. Kinaret, U. Meirav, M.A. Kastner, N.S. Wingreen, and S.J. Wind, *Self-consistent addition spectrum of a Coulomb island in the quantum Hall regime*, Phys. Rev. B **45** (1992), no. 19, 11419–11422.

[MFM+91] P.L. McEuen, E.B. Foxman, U. Meirav, M.A. Kastner, Y. Meir, N.S. Wingreen, and S.J. Wind, *Transport spectroscopy of a Coulomb island in the quantum Hall regime*, Phys. Rev. Lett. **66** (1991), no. 14, 1926–1929.

[MFZ+91] Y. Ma, R. Fletcher, E. Zaremba, M. D'Iorio, C.T. Foxon, and J.J. Harris, *Energy-loss rates of two-dimensional electrons at a $GaAs/Al_x Ga_1 - xAs$ interface*, Phys. Rev. B **43** (1991), no. 11, 9033–9044.

[MGvH+92] L.W. Molenkamp, T. Gravier, H. van Houten, O.J.A. Buijk, M.A.A. Mabesoone, and C.T. Foxon, *Peltier coefficient and thermal conductance of a quantum point contact*, Phys. Rev. Lett. **68** (1992), no. 25, 3765–3768.

[MSKH94] D.J. McKitterick, A. Shik, A.J. Kent, and M. Henini, *Edge phonoconductivity in a magnetically quantized two-dimensional electron gas*, Phys. Rev. B **49** (1994), no. 4, 2585–2594.

[Muk05] S. Mukerjee, *Thermopower of the Hubbard model: Effects of multiple orbitals and magnetic fields in the atomic limit*, Phys. Rev. B **72** (2005), no. 19, 195109.

[MvHB+90] L.W. Molenkamp, H. van Houten, C.W.J. Beenakker, R. Eppenga, and C.T. Foxon, *Quantum oscillations in the transverse voltage of a channel in the nonlinear transport regime*, Phys. Rev. Lett. **65** (1990), no. 8, 1052.

[MWK+96] A. Mittal, R.G. Wheeler, M.W. Keller, D.E. Prober, and R.N. Snacks, *Electron-Phonon scattering rates in GaAs/AlGaAs 2DEG samples below 0.5 K*, Surface Science **361/362** (1996), 537–541.

[MWL93] Y. Meir, N.S. Wingreen, and P.A. Lee, *Low-temperature transport through a quantum dot: The Anderson model out of equilibrium*, Phys. Rev. Lett. **70** (1993), no. 17, 2601–2604.

[NK06] T. Nakanishi and T. Kato, *Thermopower of a quantum dot in a coherent region*, arXiv:cond-mat/0611538 (2006).

[NL88] T.K. Ng and P.A. Lee, *On-site Coulomb repulsion and resonant tunneling*, Phys. Rev. Lett. **61** (1988), no. 15, 1768–1771.

[Oji84] H. Oji, *Thermopower and thermal conductivity in two-dimensional systems in a quantizing magnetic field*, Phys. Rev. B **29** (1984), no. 6, 3148–3152.

[OLZH05]   M.F. O'Dwyer, R.A. Lewis, C. Zhang, and T.E. Humphrey, *Electronic Efficiency in Nanostructured Thermionic and Thermoelectric Devices*, Phys. Rev. B **72** (2005), no. 23, 205330–205339.

[Ons31a]   L. Onsager, *Reciprocal Relations in Irreversible Processes. I.*, Physical Review **37** (1931), no. 4, 405–426.

[Ons31b]   L. Onsager, *Reciprocal Relations in Irreversible Processes. II.*, Physical Review **38** (1931), no. 12, 2265–2279.

[OvKP86]   H. Obloh, K. von Klitzing, and K. Ploog, *Thermomagnetic Behaviour of the Two-Dimensional Electron Gas in GaAs-$Al_xGa_{1-x}As$ Heterostructures*, Surface Science **170** (1986), 292–297.

[Pey06]   M. Peyrard, *The design of a thermal rectifier*, Europhys. Lett. e-First **5** (2006), 10223–10225.

[PFM+03]   R.M. Potok, J.A. Folk, C.M. Marcus, V. Umansky, M. Hanson, and A.C. Gossard, *Spin and Polarized Current from Coulomb Blockaded Quantum Dots*, Phys. Rev. Lett. **91** (2003), no. 1, 016802–016805.

[PG01]   M. Pustilnik and L.I. Glazman, *Kondo Effect in Real Quantum Dots*, Phys. Rev. Lett. **87** (2001), no. 21, 216601–216604.

[PLDL+05]   M. Pioro-Ladriere, J.H. Davies, A.R. Long, A.S. Sachrajda, L. Gaudreau, P. Zawadzki, J. Lapointe, J. Gupta, Z. Wasilewski, and S. Studenikin, *Origin of switching noise in GaAs/Al[sub x]Ga[sub 1 - x]As lateral gated devices*, Phys. Rev. B **72** (2005), no. 11, 115331–115338.

[Pus06]   M. Pustilnik, *Kondo effect in nanostructures*, Physica Status Solidi (a) **203** (2006), no. 6, 1137–1147.

[RDC98]   S. Roshko, W. Dietsche, and L.J. Challis, *Spectroscopy of Phonon Emission in the Quantum Hall Effect Regime*, Phys. Rev. Lett. **80** (1998), no. 17, 3835–3838.

[RJSM07]   P. Reddy, S.-Y. Jang, R.A. Segalman, and A. Majumdar, *Thermoelectricity in molecular junctions*, Science **315** (2007), 1568–1571.

[ROJ+88]   C. Ruf, H. Obloh, B. Junge, E. Gmelin, K. Ploog, and G. Weimann, *Phonon-drag effect in GaAs-$Al_xGa_{1-x}As$ heterostructures at very low temperatures*, Phys. Rev. B **37** (1988), no. 11, 6377–6380.

[Sak94]   J.J. Sakurai, *Modern Quantum Mechanics, Rev. ed.*, Addison Wesley, 1994.

[SBR+05]   R. Scheibner, H. Buhmann, D. Reuter, M.N. Kiselev, and L.W. Molenkamp, *Thermopower of a Kondo Spin-Correlated Quantum Dot*, Phys. Rev. Lett. **95** (2005), no. 17, 176602.

[Sch06]   W. Schirmacher, *Gekoppelte quantenpunkte*, Master's thesis, Physikalisches Institut (EP3), Universität Würzburg, 2006.

[She73]   R.I. Shekhter, *Zero anomalies of the resistance of tunnel junctions containing metallic inclusions in the oxide layer*, Sovjet Physics JETP **36** (1973), 747.

[SI86]   U. Sivian and Y. Imry, *Multichannel Landauer formula for thermoelectric tarnsport with application to thermopower near the mobility edge*, Phys. Rev. B **33** (1986), no. 1, 551–558.

[SIR$^+$05]   R. Schleser, T. Ihn, E. Ruh, K. Ensslin, M. Tews, D. Pfannekuche, D.C. Driscoll, and A.C. Gossard, *Co-tunneling mediated transport through excited states in the Coulomb-blockade regime*, Phys. Rev. Lett. **94** (2005), 206805–206808.

[SJH$^+$02]   D. Sprinzak, Y. Ji, M. Heiblum, D. Mahalu, and H. Shtrikman, *Charge distribution in a Kondo-correlated quantum dot*, Phys. Rev. Lett. **88** (2002), no. 17, 176805–176808.

[SMA$^+$93]   A.A.M. Staring, L.W. Molenkamp, B.W. Alphenaar, H. van Houten, M.A.A. Buyk, O.J.A. Mabesoone, C.W.J. Beenakker, and C.T. Foxon, *Coulom-blockade oscillations in the thermopower of a quantum dot*, Europhys. Lett. **22** (1993), no. 1, 57–62.

[SNB$^+$07a]   R. Scheibner, E.G. Novik, T. Borzenko, M. König, D. Reuter, A.D. Wieck, H. Buhmann, and L.W. Molenkamp, *Sequential and cotunneling behavior in the temperature-dependent thermopower of few-electron quantum dots*, Phys. Rev. B **75** (2007), no. 4, 041301–041304.

[SNB07b]   J. Sommerlatte, K. Nielsch, and H. Böttner, *Thermoelektrische Multitalente*, Physik Journal **5** (2007), 35–41.

[SRI$^+$05]   R. Schleser, E. Ruh, T. Ihn, K. Ensslin, D.C. Driscoll, and A.C. Gossard, *Finite-bias charge detection in a quantum dot*, Phys. Rev. B **72** (2005), no. 3, 035312.

[Ste68]   F. Stern, *Transverse Hall Effect in the Electric Quantum Limit*, Phys. Rev. Lett. **21** (1968), no. 25, 1687–1690.

[Str89]   P. Streda, *Quantized thermopower of a channel in the ballistic regime*, J. Phys. Condens. Matter **1** (1989), no. 5, 1025–1027.

[SvdWDF$^+$03] M. Stopa, W.G. van der Wiel, S. De Franceschi, S. Tarucha, and L.P. Kouwenhoven, *Magnetically induced Chessboard Pattern in the Conductance of a Kondo Quantum Dot*, Phys. Rev. Lett. **91** (2003), no. 4, 046601–046604.

[SWEK98]   J. Schmid, J. Weis, K. Eberl, and K. v. Klitzing, *A quantum dot in the limit of strong coupling to reservoirs*, Physica B: Condensed Matter **256–258** (1998), 182–185.

[SWEvK00]   J. Schmid, J. Weis, K. Eberl, and K. v. Klitzing, *Absence of Odd-Even Parity Behavior for Kondo Resonances in Quantum Dots*, Phys. Rev. Lett. **84** (2000), no. 25, 5824–5827.

[TAH⁺96]   S. Tarucha, D.G. Austing, T. Honda, R.J. van der Hage, and L.P. Kouwenhoven, *Shell Filling and Spin Effects in a Few Electron Quantum Dot*, Phys. Rev. Lett. **77** (1996), no. 17, 3613–3616.

[Tew04]   M. Tews, *Electronic structure and transport properties of quantum dots*, Annalen der Physik **13** (2004), no. 5, 249–304.

[TM02]   M. Turek and K.A. Matveev, *Cotunneling thermopower of single electron transistors*, Phys. Rev. B **65** (2002), no. 11, 115332–115340.

[TM06]   R. Tomaz and Y. Meir, *Magnetic impurity formation in quantum point contacts*, Nature **442** (206), no. 7105, 900–903.

[TPA⁺86]   T.J. Thornton, M. Pepper, H. Ahmed, D. Andrews, and G.J. Davies, *One-Dimensional Conduction in the 2D Electron Gas of a GaAs-AlGaAs Heterojunction*, Phys. Rev. Lett. **56** (1986), no. 11, 1198–1201.

[TPC02]   M. Terraneo, M. Peyrard, and G. Casati, *Controlling the Energy Flow in Nonlinear Lattices: A Model for a Thermal Rectifier*, Phys. Rev. Lett. **88** (2002), no. 9, 094302–094305.

[vdWDFE⁺02] W.G. van der Wiel, S. De Franceschi, J.M. Elzerman, S. Tarucha, L.P. Kouwenhoven, J. Motohisa, F. Nakajima, and T. Fukui, *Two-Stage Kondo Effect in a Quantum Dot at a High Magnetic Field*, Phys. Rev. Lett. **88** (2002), no. 12, 126803–126806.

[vdWDFF⁺00] W.G. van der Wiel, S. De Franceschi, T. Fujisawa, J.M. Elzerman, S. Tarucha, and L.P. Kouwenhoven, *The Kondo Effect in the Unitary Limit*, Science **289** (2000), 2105–2108.

[vHMBF92]   H. van Houten, L.W. Molenkamp, C.W.J. Beenakker, and C.T. Foxon, *Thermo-electric properties of quantum point contacts*, Semicond. Sci. Technol. **7** (1992), no. 3B, B215–B221.

[vKGW05]   K. v. Klitzing, R. Gerhardts, and J. Weis, *25 Jahre Quanten-Hall-Effekt*, Physik Journal **6** (2005), 37–44.

[VOJ⁺95]   D. Vion, P.F. Orfila, P. Joyez, D. Esteve, and M. H. Devoret, *Miniature electrical filters for single electron devices*, Journal of Applied Physics **77** (1995), no. 6, 2519–2524.

[Vor04]   S. Vorojtsov, *Coulomb-blockade oscillations of conductance at finite energy level spacing in a quantum dot*, Int. J. of Mod. Phys. B **18** (2004), no. 30, 3915–3940.

[vWvHB⁺88]   B.C. van Wees, H. van Houten, C.W.J. Beenakker, J.G. Williamson, L.P. Kouwenhoven, D. van der Marel, and C.T. Foxon, *Quantized conductance of point contacts in a two-dimensional electron gas*, Phys. Rev. Lett. **60** (1988), no. 9, 848–850.

[WHK95]   D. Weinmann, W. Häusler, and B. Kramer, *Spin Blockades in Linear and Nonlinear Transport through Quantum Dots*, Phys. Rev. Lett. **74** (1995), no. 6, 984–987.

[WHKP94]   J. Weis, R.J. Haug, K. v. Klitzing, and K. Ploog, *Lateral transport through a single quantum dot with a magnetic field parallel to the current*, Surface Science **305** (1994), no. 1–3, 664–668.

[WHvKP93]   J. Weis, R.J. Haug, K. v. Klitzing, and K. Ploog, *Competing channels in single-electron tunneling through a quantum dot*, Phys. Rev. Lett. **71** (1993), no. 24, 4019–4022.

[WM94]   N.S. Wingreen and Y. Meir, *Anderson model out of equilibrium: Noncrossing-approximation approach to transport through a quantum dot*, Phys. Rev. B **49** (1994), no. 16, 11040–11052.

[WRCO03]   Y. Wang, N.S. Rogado, R.J. Cava, and N.P. Ong, *Spin entropy as the likely source of enhanced thermopower in NaxCo2O4*, Nature **423** (2003), no. 6938, 425–428.

[WvHB⁺88]   B.C. van Wees, H. van Houten, C.W.J. Beenakker, J.G. Williamson, L.P. Kouwenhoven, D. van der Marel, and C.T. Foxon, *One-dimensional transport and the quantisation of the ballistic resistance*, J. Phys. C: Solid State Phys. **21** (1988), no. 9, L209–L214.

[WYGB86]   A.K.M Wennberg, S.N. Ytterboe, C.M. Gould, and H.M. Bolzer, *Electron heating in a multiple-quantum-well structure below 1 K*, Phys. Rev. B **34** (1986), no. 6, 4409–4411.

[XX99]   S.-J. Xiong and Y. Xiong, *Resonant Transmission through a Quantum Dot in the Coulomb Blockade Regime*, Phys. Rev. Lett. **83** (1999), no. 7, 1407–1410.

[XY02]   S.-J. Xiong and Y. Yin, *Asymmetric line shape and Fano interference in the transport of electrons through a multilevel quantum dot in the Coulomb blockade regime*, Phys. Rev. B **66** (2002), no. 15, 153315–153318.

[YBSS94]   X. Ying, V. Bayot, M.B. Santos, and M. Shayegan, *Observation of composite-fermion thermopower at half-filled Landau levels*, Phys. Rev. B **50** (1994), no. 7, 4969–4972.

[Zim63]   J.M. Ziman, *Electrons and phonons: The Theory of Transport Phenomena in Solids*, Clarendon Press, Oxford, 1963.

[ZL84]   W. Zawadzki and R. Lassnigc, *Magnetization, specific heat, magneto-thermal effect and thermoelectric power of two-dimensional electron gas in a quantizing magnetic field*, Surf. Sci. **142** (1984), no. 1–3, 225–235.

[ZMFB05]   V. Zlatic, R. Monnier, J. Freericks, and K.W. Becker, *Relationship between the thermopower and entropy of strongly correlated electron systems*, arXiv:cond-mat/0512288v2 (2005).

[ZMW$^+$93] U. Zeitler, J.C. Maan, P. Wyder, R. Fletcher, C.T. Foxon, and J.J. Harris, *Investigation of the electron-phonon interaction in the fractional quantum Hall regime using the thermoelectric effect*, Phys. Rev. B **47** (1993), no. 23, 16008–16011.

Danksagung

Mein Dank gilt all jenen, die es mir durch ihre Unterstützung und Mithilfe ermöglicht haben, diese Arbeit anzufertigen:

- Herrn Prof. Dr. Laurens W. Molenkamp für die Aufnahme am Lehrstuhl für Experimentelle Physik III, die Bereitstellung moderner Apparate für die experimentellen Untersuchungen und die Ermutigung zur Arbeit an thermoelektrischen Transportphänomenen.

- Herrn Prof. Dr. Hartmut Buhmann, Leiter der Quantentransportgruppe, für die Betreuung dieser Arbeit, die hilfreichen Diskussionen und die durchhaltende Bereitschaft bei der Korrektur der Veröffentlichungen sowie für wertvolle Vorschläge beim Zusammenschreiben. Hervorzuheben ist auch die Möglichkeit zur freien Bearbeitung des Forschungsthemas.

- Herrn Dr. Michael Gbordzoe, einem der wenigen Mitstreiter auf dem Gebiet der Thermokraft, der stets bereit war und ist darüber zu diskutieren und außerordentlich sorgfältig diese Arbeit korrigiert hat.

- Den aktuellen und ehemaligen Mitgliedern der Quantentransportgruppe für die Mitarbeit, Unterstützung und Diskussion über physikalische Themen, insbesondere Markus König für die Probenherstellung, Matthias Schäfer für den Ansporn immer möglichst exakt zu arbeiten, und Alena Astakova für ihre Beiträge und Unterstützung bei den Berechnungen.

- Ralf Hälterlein, Michael Scheibner, Elke Jaklin, Johannes Jaklin und Ignacio Gallegos, die das originale Manuskript durchgelesen haben.

- Meiner Frau Doris für die Geduld, das Verständnis und die Unterstützung, die sie für mich in den ganzen Jahren aufbrachte.

- Unserem Sohn Leon, der mir Tag für Tag zeigt was neben der Physik noch wichtig ist im Leben und der mich trainiert, die Dinge auf eine einfache Weise zu betrachten.

- Meinen Eltern, deren Unterstützung mich auf diesem langen Weg immer begleitet hat.

- Meinem Bruder Michael für die Weitergabe seiner Erfahrungen und meiner Schwester Tatjana für das kulturelle Ausgestalten meiner nicht vorhandenen Freizeit.

- Meiner Familie, deren belebtes und belebendes Umfeld mich immer wieder in den außerphysikalischen Alltag zurückbringt.

- Kia Tavakoli und Wilhelm Schirmacher für ihre Kollegialität.

- Katrin Pappert, die immer für eine angenehme Atmosphäre während all der Jahre im Büro C113 sorgte.

Curriculum Vitae

Ralf Scheibner, geboren am 04.03.1976 in Ebern

1982 – 1986	Grundschule Rentweinsdorf
1986 – 1995	Friedrich-Rückert-Gymnasium Ebern
Juli 1995	Abitur
Sept. 1995 – Okt. 1996	Wehrersatzdienst im Pflegedienst des Kreiskrankenhauses Ebern
Nov. 1996	Beginn des Studiums der Physik an der Julius-Maximilians-Universität Würzburg
Aug. 1998	Vordiplom
Aug. 1999 – Aug. 2000	Studium der Physik an der University of New Mexico, Albuquerque, NM (USA)
Aug. 2000	Master Of Science-Abschluß
Sept. 2000 – Jul. 2002	Fortführung des Physikstudiums und Diplomarbeit am Lehrstuhl Experimentelle Physik III der Universität Würzburg bei PD Dr. H. Buhmann. Thema: *'Transportuntersuchungen an mesoskopischen Halbleterheterostrukturen'*
Jul. 2002	Diplom in Physik
Okt. 2002 – Jan. 2007	Wissenschaftlicher Mitarbeiter am Lehrstuhl Experimentelle Physik III der Universität Würzburg bei Prof. Dr. L.W. Molenkamp
seit Feb. 2007	Entwicklungsingenieur bei der AIM Infrarot-Module GmbH in Heilbronn

Lauffen am Neckar, den 30.08.2007

Ralf Scheibner

Ehrenwörtliche Erklärung

gemäß §5 Abs. 1 und 2
der Promotionsordnung der
Fakultät für Physik und Astronomie
der Universität Würzburg
vom 22. September 2003
in der aktualisierten Fassung
vom 22. November 2005

Hiermit erkläre ich ehrenwörtlich, dass ich die Dissertation selbständig und ohne Hilfe eines Promotionsberaters angefertigt und keine weiteren als die angegebenen Quellen und Hilfsmittel benutzt habe.

Die Dissertation wurde bisher weder vollständig noch teilweise einer anderen Hochschule mit dem Ziel, einen akademischen Grad zu erwerben, vorgelegt.

Am 15. Mai 2000 wurde mir von der University of New Mexico at Albuquerque, NM (USA) der akademische Grad 'Master Of Science' verleihen. Am 27. Juli 2002 wurde mir von der Universität Würzburg der akademische Grad 'Diplom-Physiker (Univ.)' verliehen. Weitere akademische Grade habe ich weder erworben noch versucht zu erwerben.

Lauffen am Neckar, den 30.08.2007

Ralf Scheibner